



Florian Schober, BSc

**Design, realisation and control  
of electrical circuits for laboratory purposes**

**MASTER'S THESIS**

to achieve the university degree of

Diplom-Ingenieur

Master's degree programme: Information and Computer Engineering

submitted to

**Graz University of Technology**

Supervisor

Assoc.Prof. Dipl.-Ing. Dr.techn. Markus Reichhartinger

Institute of Automation and Control

## **AFFIDAVIT**

I declare that I have authored this thesis independently, that I have not used other than the declared sources/resources, and that I have explicitly indicated all material which has been quoted either literally or by content from the sources used. The text document uploaded to TUGRAZonline is identical to the present master's thesis.

---

Date

---

Signature

---

## **Abstract**

The aim of this thesis is the design, realisation and control of electrical circuits for laboratory purposes at the Institute of Automation and Control at Graz University of Technology.

The work presents a hardware section and a software section. The hardware part is about designing and implementing the electrical test circuits with the corresponding measurement set-up and the actuation electronics. By keeping the design modular, the laboratory set-up can be easily extended by implementing new test circuits. The software part integrates the test circuits in MATLAB Simulink. By abstracting the real-world systems in Simulink blocks that take input signals and output the measured system states, the blocks can be handled in the simulation similarly to state-space blocks.

Finally, several standard control and observer concepts are applied to the test circuits. They are evaluated in different experiments using the developed MATLAB Simulink interface.

# Contents

<b>Contents</b>	<b>iv</b>
<b>List of Figures</b>	<b>ix</b>
<b>List of Tables</b>	<b>xiii</b>
<b>1 Introduction</b>	<b>1</b>
1.1 Introduction and Motivation . . . . .	1
1.2 Requirements . . . . .	2
<b>2 Hardware Design and Realisation</b>	<b>3</b>
2.1 General Design . . . . .	3
2.2 Evaluation Board . . . . .	4
2.2.1 MATLAB Simulink Compatibility . . . . .	5
2.3 Connector Board . . . . .	6
2.3.1 Power Supply . . . . .	6
2.3.2 Signal Driver . . . . .	8
2.3.2.1 Low-Pass Filter Design for Digital-Analogue Conversion . . . . .	8
2.3.2.2 Amplifier Design . . . . .	11



---

2.3.2.3	Final Design and Test Measurements . . . . .	12
2.3.3	Measuring Amplifier . . . . .	14
2.3.3.1	Amplifier parameters and Test Measurements . . . . .	18
2.3.4	Plugging Interface . . . . .	19
2.4	Test Circuits . . . . .	22
2.4.1	Series Resonance Circuit . . . . .	22
2.4.1.1	State-Space Modelling . . . . .	23
2.4.1.2	Component Dimensioning . . . . .	24
2.4.1.3	Shunt Voltage Amplification . . . . .	28
2.4.1.4	Simulink Integration and Signal Flow . . . . .	31
2.4.1.5	Final Series Resonance Circuit and Model Verification	34
2.4.2	Integrator . . . . .	37
2.4.2.1	State-Space Modelling . . . . .	37
2.4.2.2	Component Dimensioning . . . . .	39
2.4.2.3	Simulink Integration . . . . .	40
2.4.2.4	Simulation and Final Integrator Circuit . . . . .	42
<b>3</b>	<b>Controller and Observer Designs</b>	<b>45</b>
3.1	Controller Designs . . . . .	45
3.1.1	Controllability . . . . .	46
3.1.2	PID Controller . . . . .	46
3.1.2.1	Ziegler-Nichols Ultimate Gain Method . . . . .	49
3.1.3	Loop-Shaping Design . . . . .	50
3.1.3.1	Design considerations . . . . .	51

---

3.1.3.2	Design Approach and Compensators . . . . .	53
3.1.4	State Feedback . . . . .	54
3.1.4.1	Eigenvalue Assignment . . . . .	55
3.1.4.2	LQR . . . . .	58
3.1.5	PI-State Controller . . . . .	59
3.1.6	1-Sliding Controller . . . . .	61
3.1.7	Super-Twisting Controller . . . . .	62
3.1.8	Feedforward control . . . . .	62
3.1.8.1	Trajectory planning . . . . .	64
3.2	Observer Designs . . . . .	65
3.2.1	Observability . . . . .	65
3.2.2	Luenberger Observer . . . . .	66
3.2.3	Reduced Observer . . . . .	67
3.2.4	Super-Twisting Observer . . . . .	68
3.3	Observer-Based control . . . . .	70
3.3.1	Separation Theorem . . . . .	70
3.3.2	Observer-Based Disturbance Attenuating Controller . . . . .	71
<b>4</b>	<b>Controller and Observer Designs for the test circuits</b>	<b>76</b>
4.1	Series Resonance Test Circuit . . . . .	76
4.1.1	Controller Designs . . . . .	77
4.1.1.1	PID Controller . . . . .	77
4.1.1.2	LS Controller . . . . .	78
4.1.1.3	State Controller . . . . .	85

---

Eigenvalue Assignment . . . . .	85
LQR . . . . .	86
4.1.1.4 PI-State Controller . . . . .	87
4.1.1.5 1-Sliding Controller . . . . .	88
4.1.1.6 Super-Twisting Controller . . . . .	89
4.1.1.7 Feedforward Control . . . . .	90
4.1.2 Controller Designs for Current Controlled Circuit . . . . .	91
4.1.2.1 State Controller . . . . .	91
4.1.2.2 Super-Twisting Controller . . . . .	92
4.1.3 Observer Designs . . . . .	93
4.1.3.1 Luenberger Observer . . . . .	93
4.1.3.2 Reduced Observer . . . . .	94
4.1.3.3 Super-Twisting Observer . . . . .	94
4.2 Integrator Test Circuit . . . . .	96
4.2.1 State Controller . . . . .	96
4.2.2 1-sliding Controller . . . . .	97
4.2.3 Super-Twisting Controller . . . . .	98
4.2.4 OBDA Controller . . . . .	99
<b>5 Experimental Results</b>	<b>102</b>
5.1 Series Resonance Circuit . . . . .	102
5.1.1 Experiment 1 . . . . .	103
5.1.2 Experiment 2 . . . . .	106
5.1.3 Experiment 3 . . . . .	107

---

5.1.4	Experiment 4 . . . . .	108
5.1.5	Experiment 5 . . . . .	110
5.2	Integrator . . . . .	111
5.2.1	Experiment 6 . . . . .	112
5.2.2	Experiment 7 . . . . .	113
	. . . . .	114
5.2.3	Experiment 8 . . . . .	115
<b>6</b>	<b>Conclusion and Further Work</b>	<b>117</b>
	<b>Bibliography</b>	<b>119</b>
<b>A</b>	<b>Appendix</b>	<b>121</b>
A.1	Notes on MATLAB Simulink . . . . .	121
A.1.1	Installations for Hardware Support . . . . .	121
A.1.2	Setting up and Running a Simulation . . . . .	122
A.1.3	Data Export . . . . .	122
A.2	Pinout Evaluation Board . . . . .	122
A.3	Connector Board . . . . .	124
A.4	Series Resonance Test Circuit . . . . .	125
A.4.1	Circuit Diagram . . . . .	125
A.4.2	Adjustment Instruction . . . . .	125
A.5	Integrator Test Circuit . . . . .	127
A.5.1	Circuit Diagram . . . . .	127
A.5.2	Adjustment Instruction . . . . .	127

# List of Figures

2.1	Texas Instruments LAUNCHXL-F28069M. . . . .	4
2.2	MATLAB Simulink External Mode . . . . .	5
2.3	Connector Board . . . . .	7
2.4	Power supply circuit diagram . . . . .	8
2.5	Second-order LPF circuit diagram . . . . .	9
2.6	Signal driver LC-LPF magnitude plot . . . . .	9
2.7	Signal driver LPF circuit diagram . . . . .	10
2.8	Signal driver LPF magnitude . . . . .	10
2.9	Signal driver LPF simulation . . . . .	11
2.10	Non-inverting amplifier . . . . .	12
2.11	Signal driver circuit diagram . . . . .	13
2.12	Signal driver test measurements . . . . .	14
2.13	Differential amplifier circuit diagram . . . . .	15
2.14	Measuring amplifier test measurements . . . . .	19
2.15	Plugging Interface . . . . .	20
2.16	Connected laboratory set-up . . . . .	22
2.17	Series resonance circuit . . . . .	23

---

2.18	Series resonance circuit with switchable capacitors . . . . .	27
2.19	Simscape simulation set-up series resonance circuit . . . . .	28
2.20	Series resonance circuit shunt voltage simulation . . . . .	29
2.21	Shunt voltage amplifier . . . . .	29
2.22	Serial resonance circuit Simulink block . . . . .	31
2.23	Serial resonance circuit Simulink integration . . . . .	33
2.24	Soldered series resonance circuit . . . . .	35
2.25	Serial resonance circuit model verification . . . . .	36
2.26	Serial resonance circuit detailed model verification . . . . .	36
2.27	Simplified integrator circuit diagram . . . . .	37
2.28	Integrator magnitude plot . . . . .	40
2.29	Integrator circuit Simulink block . . . . .	41
2.30	Integrator circuit Simulink integration . . . . .	42
2.31	Soldered integrator circuit . . . . .	43
2.32	Simulated integrator circuit. . . . .	44
2.33	Integrator model verification . . . . .	44
3.1	PID closed-loop block diagram . . . . .	47
3.2	Effect of single PID actions. . . . .	48
3.3	Proportional controlled closed-loop block diagram . . . . .	49
3.4	Block diagram control system with noise . . . . .	50
3.5	Bode plot frequency sections . . . . .	51
3.6	Block diagram state controlled system . . . . .	55
3.7	PI state controlled closed-loop block diagram . . . . .	59

---

3.8	Closed-loop block diagram including feedforward control . . . . .	63
3.9	Flatness based two degrees of freedom control . . . . .	64
3.10	Closed-loop block diagram with estimated state feedback . . . . .	71
3.11	Closed-loop block diagram with estimated state feedback and distur- bance attenuation . . . . .	73
3.12	Closed-loop block diagram with estimated state feedback and distur- bance attenuation . . . . .	75
4.1	PID closed-loop experiment . . . . .	78
4.2	Series resonance circuit margins . . . . .	79
4.3	Bode plot loop-shaping 1 . . . . .	80
4.4	Bode plot loop-shaping 2 . . . . .	82
4.5	Bode plot lag compensator . . . . .	83
4.6	Bode plot loop-shaping 3 . . . . .	83
4.7	Step responses LS controllers . . . . .	84
4.8	Simulation of the planned trajectory . . . . .	91
4.9	Output impact of the disturbance with and without attenuation . . .	101
5.1	Results experiment 1a, $y$ . . . . .	103
5.2	Results experiment 1a, $u$ . . . . .	104
5.3	Results experiment 1b, $y$ . . . . .	105
5.4	Results experiment 2, $\hat{x}$ . . . . .	106
5.5	Results experiment 2, $\hat{x}$ detail . . . . .	107
5.6	Results experiment 3, $y$ . . . . .	108
5.7	Results experiment 4, $y$ . . . . .	109
5.8	Results experiment 4, $u$ . . . . .	109

5.9	Results experiment 5, $y$ . . . . .	110
5.10	Results experiment 5, $u$ . . . . .	111
5.11	Results experiment 6, $y$ . . . . .	112
5.12	Results experiment 6, $u$ and $\Delta$ . . . . .	113
5.13	Results experiment 7a, $y$ . . . . .	114
5.14	Results experiment 7a, $u$ and $\Delta$ . . . . .	114
5.15	Results experiment 7b, $y$ . . . . .	115
5.16	Results experiment 8, $y$ . . . . .	116
5.17	Results experiment 8, $u$ and $\Delta$ . . . . .	116
A.1	Pinout evaluation board . . . . .	123
A.2	Circuit diagram connector board . . . . .	124
A.3	Circuit diagram series resonance test circuit . . . . .	126
A.4	Serial resonance circuit Simulink integration . . . . .	126
A.5	Circuit diagram integrator test circuit . . . . .	127
A.6	Integrator circuit Simulink integration . . . . .	128



# List of Tables

2.1	Measured output resistance of the two signal driver channels. . . . .	13
2.2	Differential amplifier component values . . . . .	18
2.3	Measurement amplifier parameter . . . . .	18
2.4	Plugging interface pinout . . . . .	21
2.5	Series resonance circuit component values . . . . .	26
2.6	Shunt voltage amplifier parts . . . . .	31
3.1	Increased PID gains effect. . . . .	49
3.2	Ziegler-Nichols gain setting . . . . .	50
3.3	Trajectory planning coefficients . . . . .	65
4.1	PID gains . . . . .	78
5.1	Altered controller parameters experiment 1b and 3 . . . . .	105
5.2	Altered controller parameters experiment 8 . . . . .	111
A.1	Component values connector board . . . . .	125
A.2	Component values series resonance test circuit . . . . .	125
A.3	Component values integrator test circuit . . . . .	127

# 1 Introduction

## 1.1 Introduction and Motivation

The main aim of this work is to provide a laboratory set-up where selected control and observer algorithms are designed, realised and tested on a real electronic system. The set-up should then be used at the Institute of Automation and Control at Graz University of Technology.

Within theory classes proposed methods are commonly demonstrated in simulation only. However, in real-world systems additional problems and restrictions occur. Such problems are

- model uncertainty respectively parameter uncertainty,
- measurement noise,
- input disturbances or perturbations and
- actuator restrictions limiting the control signal.

In laboratory classes, the knowledge from the theory is applied and tested on real systems in order to demonstrate the behaviour of the designed feedback loops. Nevertheless, these systems, although visualising the control task, are often bulky and hence not easy to transport. Therefore, the idea is to implement a small laboratory set-up that can easily be transported. Hence, being able to showcase discussed methods on real systems and demonstrating the impact due to problems that appear in real systems also in theory classes.

However, the laboratory set-up is also aimed to serve as a basis for future laboratory classes. Thus, it is favourable to replicate different control and observer tasks within the set-up to be able to apply a large variety of different control and observer algorithms. Furthermore, the set-up should be easy to operate.

The final goal of this work is to design, realise and apply different controller and observer methods on the designed hardware.

This thesis is structured as follows: Based on the defined requirements in the next section, Chapter 2 elaborates the design and implementation of the hardware part. Then a general overview and theoretical background of the implemented controller and observer concepts is given in Chapter 3. Subsequently Chapter 4 presents the actual design steps and calculations of these methods when applied to the realised test circuits. The results of the experiments that were carried out are discussed in Chapter 5. Finally, Chapter 6 gives concluding remarks and outlines possibilities for further work.

## 1.2 Requirements

From the previous section several requirements are deduced for the hardware part of the laboratory set-up. For a better overview these requirements are listed first and then explained in more detail. The hardware requirements for the laboratory set-up are:

- interfacing with MATLAB Simulink,
- different control tasks / systems,
- electrical systems only,
- an expandable structure,
- measurement of four different state variables and
- two actuator signals.

Starting with the MATLAB Simulink interfacing, this is specified as it is a common environment for control engineering and often used in classes. By aiming a wide spectrum of controller and observer algorithms it is necessary to provide different control tasks to compare the algorithms. Furthermore, specially designed systems also allow to test and highlight certain features like disturbance attenuation or uncertainty estimation.

Implementing the test systems as solely electrical circuits allows to obtain a small design but at the expense of losing the real-world visualization of the control task e.g. balancing a rod with a cart. However, requiring an expandable structure allows to link the laboratory set-up to other hardware where mechanical action may happen.

By requiring four measurement channels, systems up to fourth order can be monitored and with the two actuator channels it is possible to handle systems with two inputs.

# 2 Hardware Design and Realisation

## 2.1 General Design

Based on the requirements given in the previous chapter, the hardware of the laboratory set-up was divided into three sections

- a *sensor and actuator board*,
- a *connector board* for signal amplification and transformation and
- the *test circuits*.

The main task of the *sensor and actuator board* is to provide measured data from the experimental hardware set-up to MATLAB Simulink. Furthermore, the board sets the actuator signals and applies changes made in MATLAB Simulink to the test circuit. Hence, the sensor and actuator board requires a measurement module with Analogue-to-Digital Converter (ADC), a Digital-to-Analogue Converter (DAC) or Pulse-Width-Modulation (PWM) for actuation and some form of communication module to interface with MATLAB Simulink on the computer.

The *connector board* takes the differentially measured state variables from the test circuit, amplifies them and outputs the signals ground referenced to the sensor and actuator board. Moreover, the connector board provides the supply voltage for the test circuits and decouples the actuator signals from the sensor and actuator board via an impedance transformer and forwards them to the test circuits. By using defined plugging interfaces test circuits can be exchanged easily.

Last part of the hardware set-up are the *test circuits*. The test circuits represent the actual plant. For this thesis two simple circuits with different characteristics are designed.

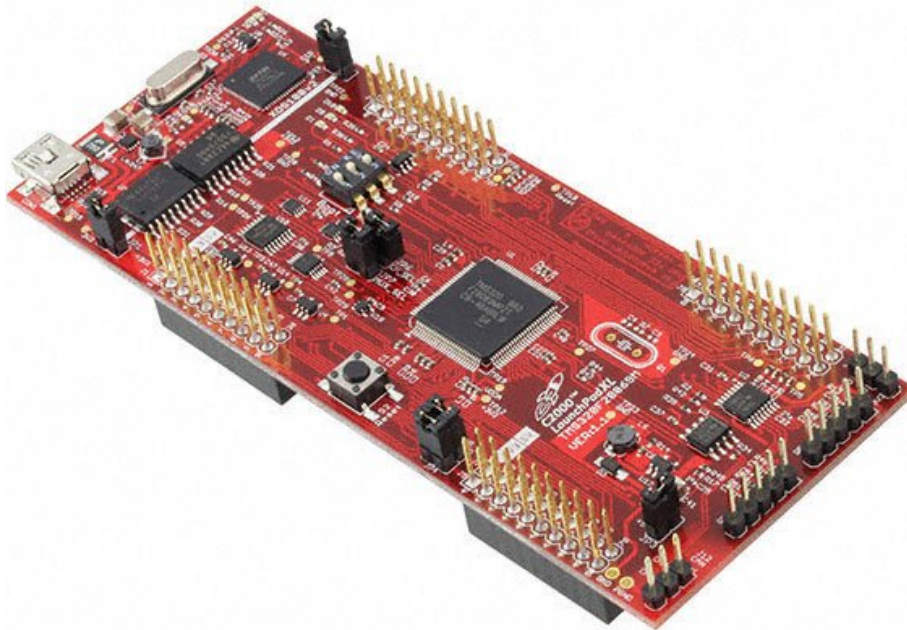


Figure 2.1: Texas Instruments LAUNCHXL-F28069M.

## 2.2 Evaluation Board

Most modern microcontrollers are equipped with ADC, DAC and PWM modules. There is also hardware support through MATLAB Simulink for various different microcontrollers<sup>1</sup>. Therefore, the decision was made to use a microcontroller ( $\mu\text{C}$ ) as sensor and actuator board. More precisely an evaluation board which features a  $\mu\text{C}$ . The choice to use an evaluation board is due to usability reasons since the evaluation board already supplies the  $\mu\text{C}$  as well as making access to the pins of the  $\mu\text{C}$  much more convenient.

For the laboratory set-up the *Texas Instruments LAUNCHXL-F28069M*<sup>2</sup> (Figure 2.1) evaluation board is used. The evaluation board features a *Texas Instruments TMS320F28069M* microcontroller<sup>3</sup> from the C2000 piccolo product family. Some key features of the TMS320F28069M are

- 90 MHz clock frequency,
- 32-bit architecture,
- native float operations,
- 16 ADC channels (12-bit),

<sup>1</sup><https://www.mathworks.com/hardware-support/home.html>

<sup>2</sup><http://www.ti.com/tool/LAUNCHXL-F28069M>

<sup>3</sup><http://www.ti.com/product/tms320f28069m>

- 16 PWM channels (up to 2MHz) and an
- Universal Asynchronous Receiver-Transmitter (UART) module.

In the laboratory set-up, the evaluation board is connected via USB to the host computer that runs MATLAB Simulink. The board is supplied through the USB interface. Also the communication between the host computer and target  $\mu\text{C}$  is handled using the built in USB to UART adapter of the evaluation board.

### 2.2.1 MATLAB Simulink Compatibility

The  $\mu\text{C}$  can be used with MATLAB Simulink by installing the *TI C2000 Piccolo Support from Embedded Coder* hardware support package<sup>4</sup>, requiring MATLAB Coder, Simulink Coder and Embedded Coder toolboxes for code generation.

The hardware support package offers pre-defined hardware configurations for the Simulink models and a toolchain to build and deploy the generated code on the  $\mu\text{C}$ . The different functionalities and modules of the  $\mu\text{C}$  can be accessed via Simulink-blocks, e.g. ADC-block, PWM-block or GPIO-block.

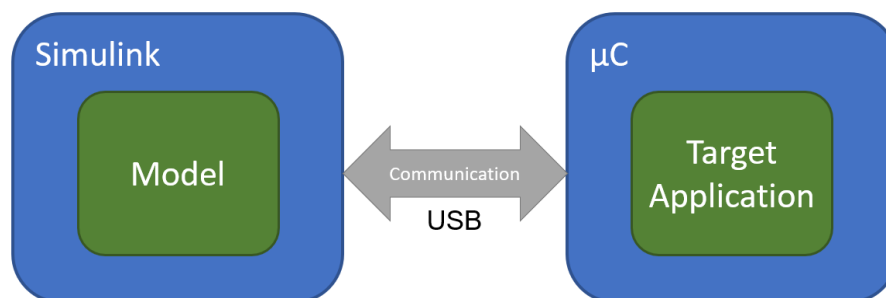


Figure 2.2: Schematic overview of the MATLAB Simulink simulation in External Mode with host and target  $\mu\text{C}$ .

Figure 2.2 illustrates the set-up when the MATLAB Simulink model is executed in *External Mode*. Firstly, an executable is generated and deployed on the TMS320F28069M target  $\mu\text{C}$ . While running, the target application on the  $\mu\text{C}$  communicates with the model on the Simulink host allowing to update parameter changes from the model to the target in real-time. Vice versa, signal data from the target application can be retrieved and monitored in the model. However, limitations arise in terms of data exchange between computer and  $\mu\text{C}$ , where the  $\mu\text{C}$  is fully capable of performing the given task but the actions are too fast to monitor on the computer. This was unfortunately not noticed until the first hardware implementation was fully tested and then tried together with the evaluation board. The upper limit obtained to get correct data are sample rates of about  $1\text{kHz} - 2\text{kHz}$ . Furthermore, the data

<sup>4</sup><https://www.mathworks.com/hardware-support/ti-c2000-piccolo.html>

export from MATLAB Simulink is tedious with the currently used method, however, possible improvements are shown in the appendix.

## 2.3 Connector Board

The connector board is the linking part between the evaluation board and the test circuit. Figure 2.3 shows the board, splitting and highlighting its functionality in three parts

- a power supply (red),
- a signal driver (green) and
- a measuring amplifier (blue).

The extra power supply provides power to the connector board and test circuits independently from the evaluation board and reduces the load for the latter. Incoming actuator signals from the evaluation board are amplified, decoupled and forwarded by the signal driver. The measuring amplifier takes the differentially measured signals from the test circuits and scales them for the evaluation board.

The next sections will explain the three different modules in more detail.

### 2.3.1 Power Supply

As mentioned in Section 2.2, the evaluation board supplies the  $\mu\text{C}$ . Furthermore, the board also offers a  $5\text{V}$  supply with a maximum current of  $0.5\text{A}$ . These ratings are sufficient for the purposes of this laboratory set-up, however, supply via the evaluation board was discarded to keep the load for the board minimal. Thus, a simple power supply is integrated on the connector board.

Figure 2.4 shows the circuit diagram of the designed power supply. To get a constant output voltage  $V_+ = 5\text{V}$ , a positive voltage regulator IC  $L7805\text{CV}^5$  from STMicroelectronics is used. The circuit design is taken from the application information in the datasheet. The input voltage  $V_{in}$  is provided through a  $12\text{V}$ ,  $1.5\text{A}$  power adapter.

Having a constant voltage of  $5\text{V}$  not only allows to supply the operational amplifiers (OPAMPs) on the connector board and test circuits, but also use this voltage as a reference voltage e.g. used in the measuring amplifier section.

---

<sup>5</sup><https://www.st.com/resource/en/datasheet/178.pdf>

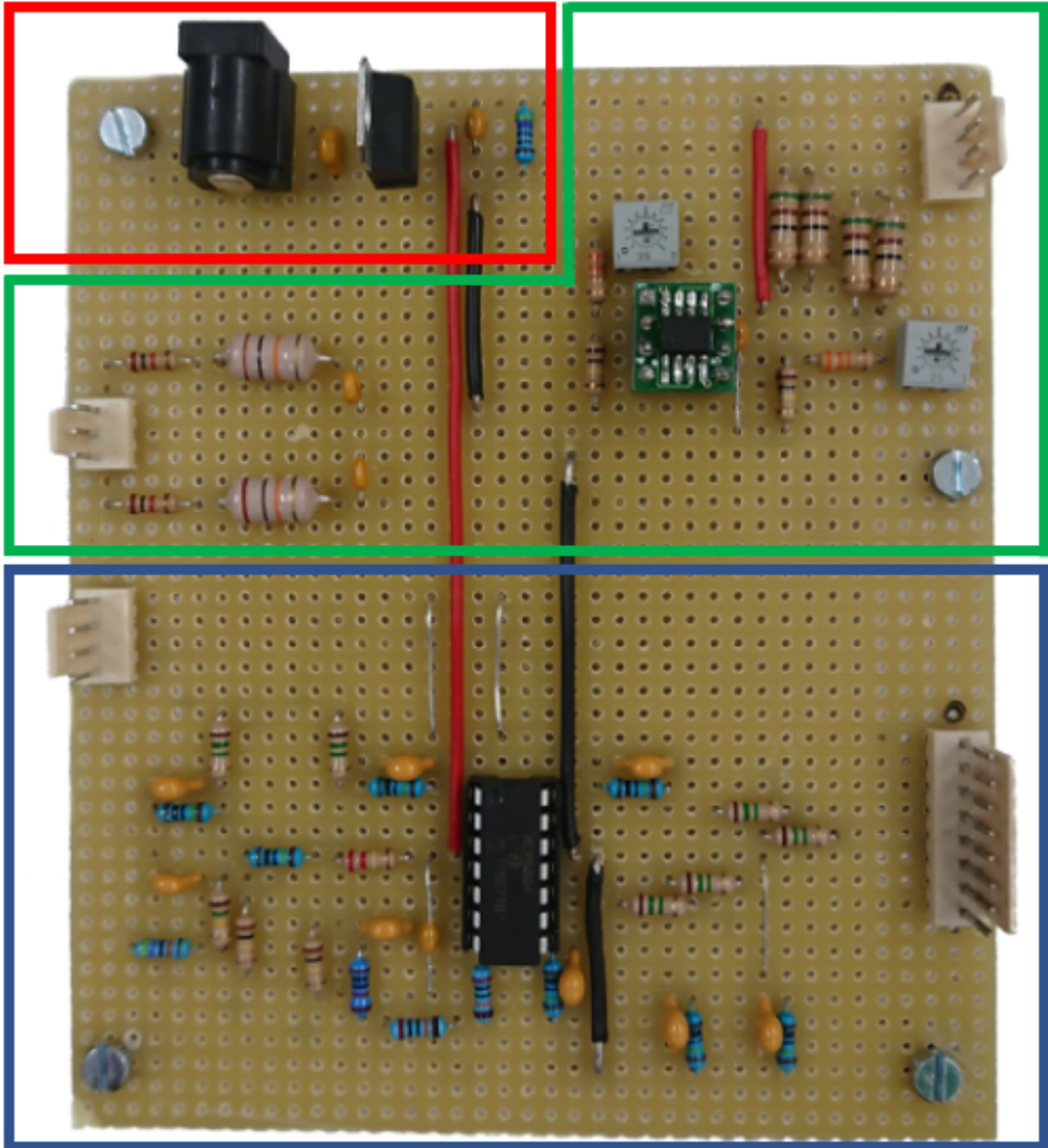


Figure 2.3: The connector board with its three different modules: power supply (red), signal driver (green) and measuring amplifier (blue). The left side is connected to the evaluation board, the right side to the test circuits. The black dots on the right side indicate where the black wire must be located.



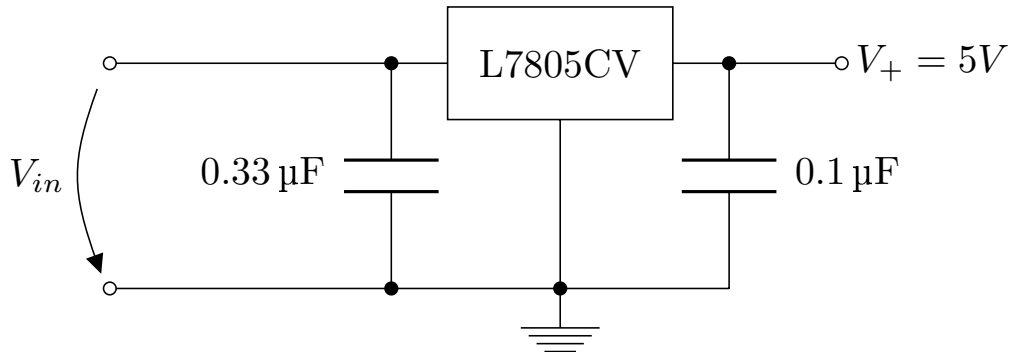


Figure 2.4: Circuit diagram of the power supply.

To have a common ground between the boards, the ground levels of the evaluation board, connector board and test circuits are connected.

### 2.3.2 Signal Driver

The task of the signal driver is to take the actuator signals from the evaluation board and forward them to the test circuits. The first stage of the design was to define the actuator signals, which will be applied to the "plant" electronics. As "fast switching" sliding-mode controllers are designed and tested in the laboratory set-up, DAC-signals from the LAUNCHXL-F28069M evaluation board are discarded and the much faster PWM-signals are used. However, using PWM-signals requires an additional low-pass filter (LPF) on the connector board.

#### 2.3.2.1 Low-Pass Filter Design for Digital-Analogue Conversion

The PWM-signal of the LAUNCHXL-F28069M can be operated with up to  $2\text{MHz}$ . Nevertheless, accuracy decreases with very high frequencies. Thus, the PWM at the evaluation board is operated between  $100\text{kHz}$  and  $500\text{kHz}$ . The cutoff frequency of the LPF is designed to be at  $8\text{kHz}$  -  $10\text{kHz}$ , to have enough bandwidth for discontinuous control signals up to  $1\text{kHz}$ , but still suppressing the PWM frequencies.

To minimize errors from the digital-analogue conversion of the PWM-signal, a second-order LPF as shown in Figure 2.5 is designed. The input-output relation of the second-order LPF reads as

$$\frac{V_{LPF}}{V_{PWM}} = G_{LPF}(s) = \frac{1}{s^2LC + 1}.$$

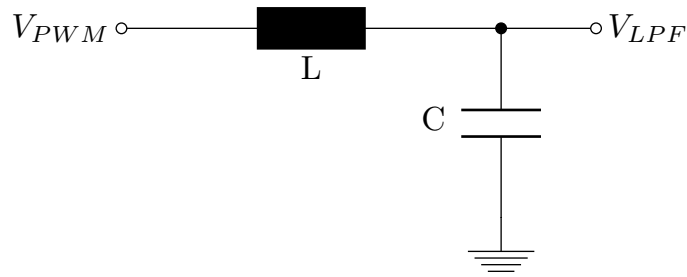


Figure 2.5: Circuit diagram of a simple second-order LC low-pass filter.

The cutoff frequency

$$f_c = \frac{1}{2\pi\sqrt{LC}},$$

further leads to the time constant  $\tau = LC$ ,

$$\tau = LC = \frac{1}{(2\pi f_c)^2},$$

$$\tau = LC = \frac{1}{(2\pi \cdot 9000Hz)^2},$$

$$\tau = LC = 31.3ns.$$

Thus, the component values are selected as  $C = 33nF$  and  $L = 10mH$ , which results in a cutoff frequency of  $8761Hz$ .

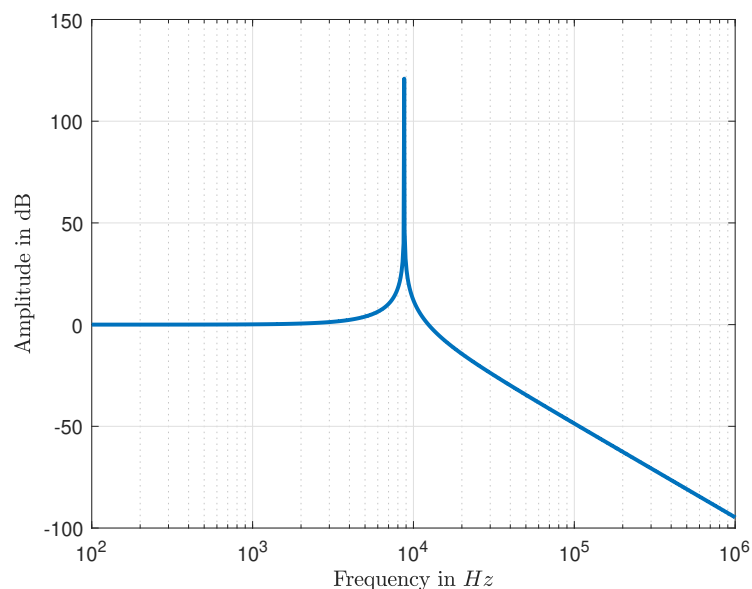


Figure 2.6: Magnitude plot of the second-order LC-LPF.

However, as Figure 2.6 shows, the circuit has a very high amplification at the resonance frequency which is not desired. Thus, a resistor of  $1k\Omega$  is added to the LPF

circuit. The resistor reduces the current through the LPF and ensures a minimum resistance especially at the cutoff frequency, therefore, suppressing the previously given amplification. Figure 2.7 shows the final circuit diagram of the designed second-order LPF.

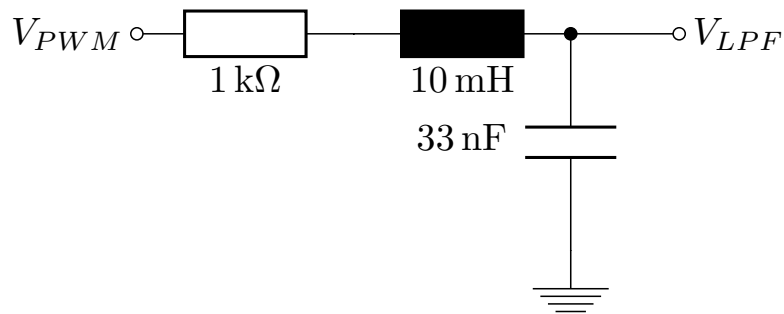


Figure 2.7: Circuit diagram of the second-order RLC low-pass filter used for digital-analogue conversion of the PWM-signal from the evaluation board.

The magnitude plot of the designed second-order LPF is shown in Figure 2.8. As can be seen, frequencies up to the cutoff frequency ( $8761Hz$ ) pass the LPF without any damping. Signals with a frequency above the cutoff frequency are suppressed by an attenuation of  $-40dB$  per decade.

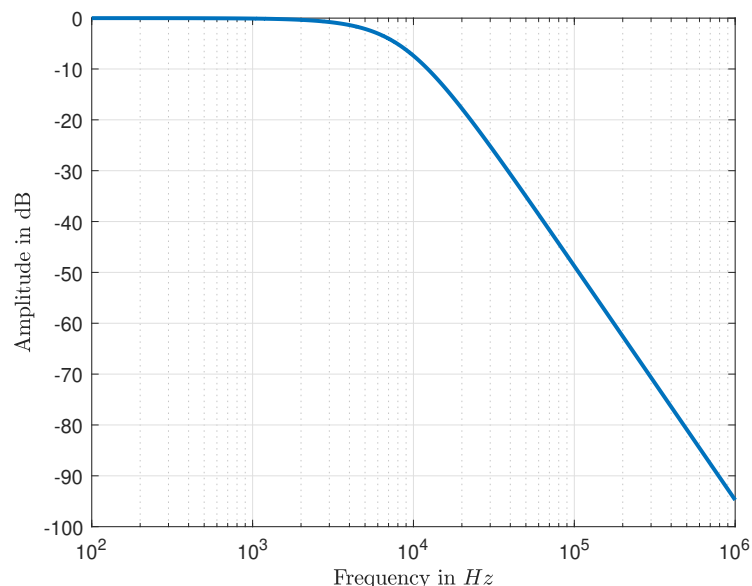


Figure 2.8: Magnitude plot of the designed second-order RLC low-pass filter for the signal driver.

A second-order LPF is used, since the PWM-signal with its steps contains high frequencies that should not appear in the filtered output signal and the requirement of at least  $8kHz$  cutoff frequency. Figure 2.9 highlights the need of a second-order LPF, since a first-order LPF with similar cutoff frequency does not suppress the

higher frequencies of the PWM-signal strong enough.

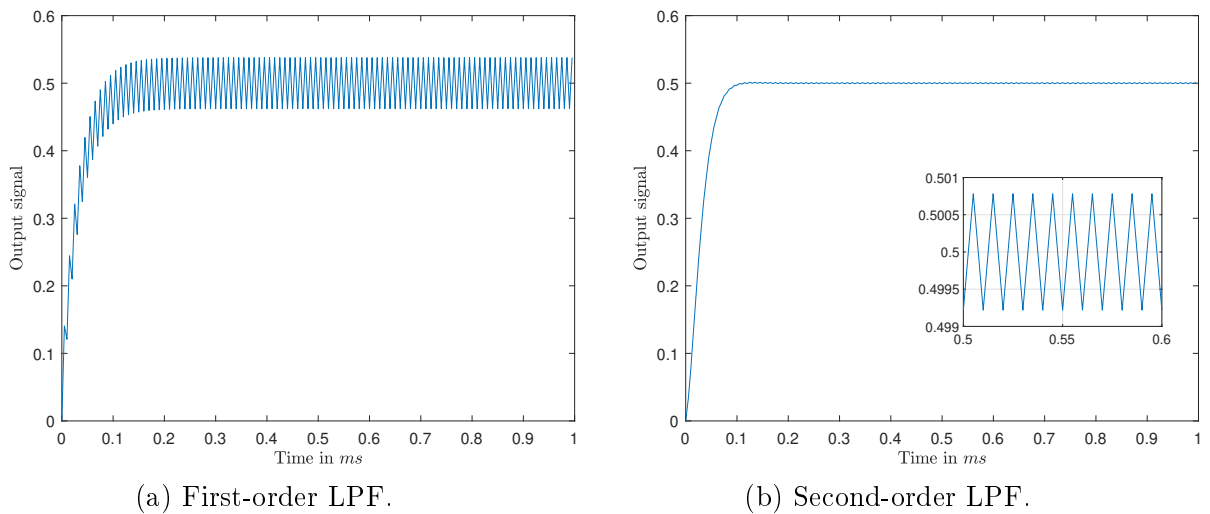


Figure 2.9: Simulation of the digital-analogue conversion using first- and second-order LPF with a PWM input signal. PWM: 50% duty cycle, amplitude 1 and  $200kHz$  frequency.

### 2.3.2.2 Amplifier Design

The low-pass filtered PWM-signal is then amplified using a non-inverting amplifier as shown in Figure 2.10. The amplifier guarantees that there is no load on the second-order LPF, ensuring correct functionality of the LPF. Additionally, the operational amplifier has a low output resistance. By using extra resistors at the output, a defined low output resistance is archived. In case of the connector board a  $25\Omega$  resistor is used.

The amplifier also should be able to provide enough current even if there is a short circuit in the "plant" electronics. With a given maximum output voltage of  $5V$  and an output resistance of  $25\Omega$ , neglecting the output resistance of the operational amplifier, the maximum current of the operational amplifier can be calculated as

$$I_{max} = \frac{U_{max}}{R_{out}} = \frac{5V}{25\Omega} = 200mA.$$

Thus, the Analog Devices AD8532<sup>6</sup> operational amplifier is used, with the amplifier having a maximum output current of  $250mA$ .

<sup>6</sup>[https://www.analog.com/media/en/technical-documentation/data-sheets/AD8531\\_8532\\_8534.pdf](https://www.analog.com/media/en/technical-documentation/data-sheets/AD8531_8532_8534.pdf)

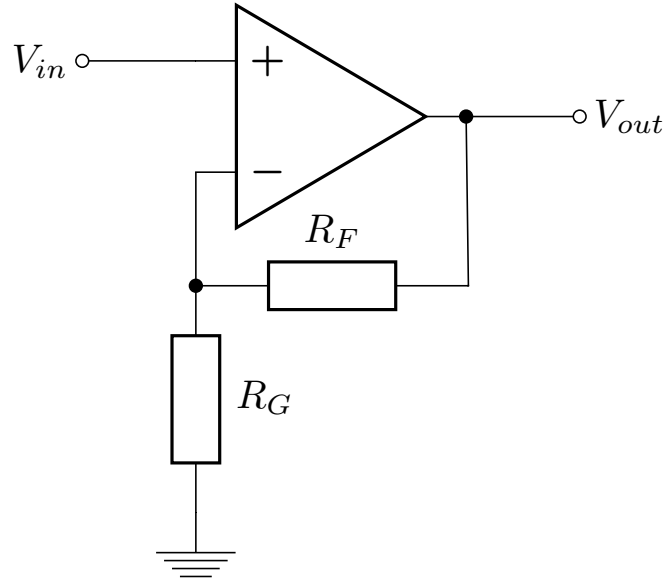


Figure 2.10: Circuit diagram of a non-inverting amplifier.

The amplification of the low-pass filtered signal is done by operating the operational amplifier as non-inverting amplifier. The PWM of the LAUNCHXL-F28069M has an amplitude of  $3.3V$  and hence the maximum of the low-pass filtered signal is also  $3.3V$ . The output of the signal-driver should have a maximum of  $5V$ . Thus, the gain  $g$  of the non-inverting amplifier can be calculated as

$$g = \frac{V_{out}}{V_{in}} = \frac{5V}{3.3V} = 1.52.$$

The gain of the non-inverting amplifier is given by

$$g = 1 + \frac{R_F}{R_G},$$

with  $R_F$  being the feedback resistor and  $R_G$  the ground resistor.

By selecting the ground resistor  $R_G$  of the non-inverting amplifier as  $100k\Omega$ , the feedback resistor  $R_F$  results as

$$R_F = (g - 1)R_G = (1.52 - 1)100k\Omega = 52k\Omega.$$

### 2.3.2.3 Final Design and Test Measurements

Figure 2.7 shows the circuit diagram for one channel of the signal driver. On the left side of the circuit diagram there is the designed second-order LPF that performs

digital-analogue conversion of the PWM-signal. Amplification is done with the non-inverting amplifier being on the right side of the circuit diagram. As defined in the requirements Section 1.2, there are two actuator signals, and thus two signal driver channels.

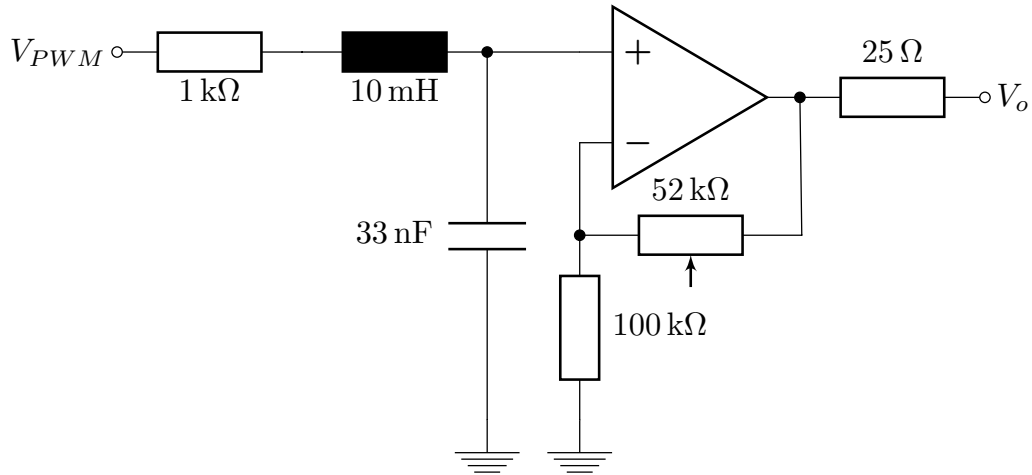


Figure 2.11: Circuit diagram of one channel of the signal driver. The positive input of the non-inverting amplifier is connected to the second-order LPF.

To compensate tolerances of the resistors, the feedback resistor  $R_F$  of the non-inverting amplifier is realised as a potentiometer. Figure 2.12 shows the test measurements of the two signal driver channels. The measurements were performed using the PWM of the evaluation board as input and an oscilloscope for measurement. As it is illustrated in Figure 2.12, after adjustment of the potentiometer both channels perform as expected, i.e. almost no deviation from the desired behaviour.

The output resistance of the signal driver was also measured. This was done by using a fixed voltage output at the signal driver and a known resistor to measure the current. Table 2.1 shows the measured results. As seen, the measured resistance differs from the used  $25\Omega$  resistor, however, output resistance of the operational amplifier, line resistance and resistance from the plugging interface also add up to the measured values.

channel	resistance
1	$31.7\Omega$
2	$31.6\Omega$

Table 2.1: Measured output resistance of the two signal driver channels.

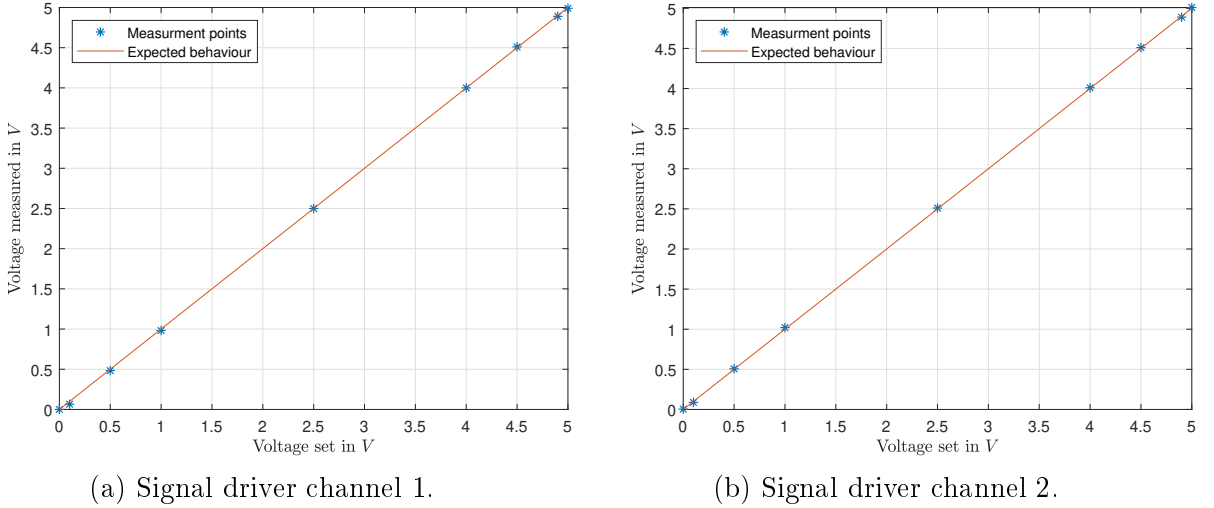


Figure 2.12: Test measurement of the two signal driver channels.

### 2.3.3 Measuring Amplifier

The third functional module of the connector board is the measuring amplifier. The differentially measured input signals from the test circuits are scaled according to the channel specification. The output are ground referenced signals that are within the ADC range of the evaluation board. To prevent faulty signals reconstruction due to discretisation and consequently reflections from frequencies above the Nyquist-frequency, the measuring amplifier also implements an anti-aliasing filter. Figure 2.13 shows the general circuit design of the four amplifier channels.

At the start of the amplifier design the input voltage is assumed to be constant, thus allowing to neglect the capacitors. The given differential amplifier with bias shift can be split in three parts that can be discussed separately using the superposition principle.

The first part is the negative input  $V_-$ . The input is amplified with an inverting amplifier

$$V_{out-} = -\frac{R_4}{R_3}V_- \quad (2.1)$$

The second part is the positive input  $V_+$ . At first, the input voltage is split via a voltage divider and then amplified with a non-inverting amplifier

$$V_{out+} = \frac{R_2 || R_{REF}}{R_1 + R_2 || R_{REF}} \left( 1 + \frac{R_4}{R_3} \right) V_+ \quad (2.2)$$

The third and last part is a bias shift using a reference voltage. The amplification is similar to the previous part of the positive input and given by

$$V_{out_{REF}} = \frac{R_1 || R_2}{R_{REF} + R_1 || R_2} \left( 1 + \frac{R_4}{R_3} \right) V_{REF} \quad (2.3)$$

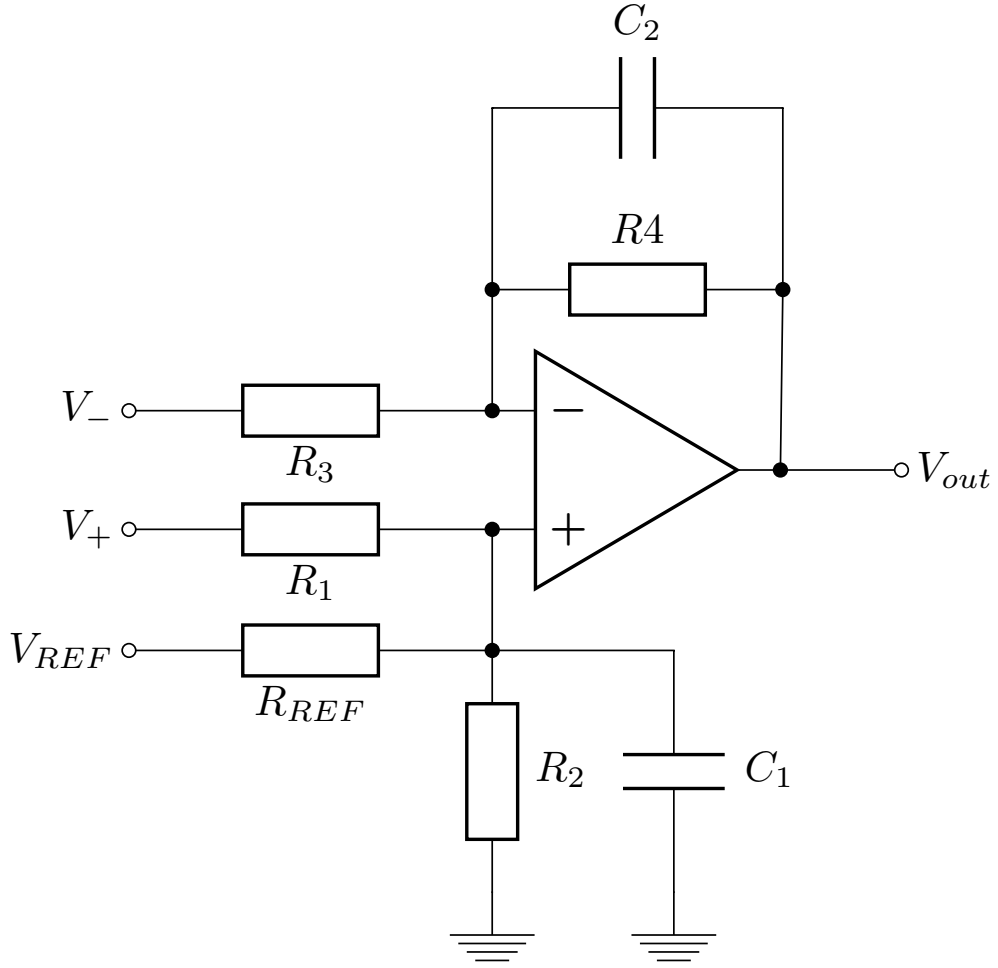


Figure 2.13: Circuit diagram of a differential amplifier with bias shift and anti-aliasing filter.

Thus, the output voltage of the differential amplifier adds up according to superposition principle as the sum of the different parts (2.1), (2.2) and (2.3), resulting in

$$V_{out} = V_{out+} + V_{out-} + V_{outREF},$$

$$V_{out} = \frac{R_2 || R_{REF}}{R_1 + R_2 || R_{REF}} \left( 1 + \frac{R_4}{R_3} \right) V_+ + \left( -\frac{R_4}{R_3} \right) V_- + \frac{R_1 || R_2}{R_{REF} + R_1 || R_2} \left( 1 + \frac{R_4}{R_3} \right) V_{REF}. \quad (2.4)$$

The amplification of the given differential amplifier with bias shift should equal a



linear equation of the form

$$V_{out} = gV_{in} + b, \quad (2.5)$$

$$V_{out} = g(V_+ - V_-) + b, \quad (2.6)$$

with a desired gain  $g$  and bias  $b$ .

Therefore, by expanding equation (2.4) and equate it with equation (2.6), the comparison of coefficients results the following three relations

$$\mathbf{V}_- : g = \frac{R_4}{R_3}, \quad (2.7)$$

$$\mathbf{V}_+ : g = \frac{R_2 R_{REF}}{R_1 R_2 + R_1 R_{REF} + R_2 R_{REF}} \left(1 + \frac{R_4}{R_3}\right), \quad (2.8)$$

$$\mathbf{V}_{REF} : b = \frac{R_1 R_2}{R_1 R_2 + R_1 R_{REF} + R_2 R_{REF}} \left(1 + \frac{R_4}{R_3}\right) V_{REF}. \quad (2.9)$$

Equations (2.8) and (2.9) can be further simplified by rearranging to their common denominator and equating the results to get resistor relations for  $R_{REF}$  depending on  $R_1$

$$\frac{R_{REF} R_2}{g} \left(1 + \frac{R_4}{R_3}\right) = \frac{R_1 R_2}{b} \left(1 + \frac{R_4}{R_3}\right) V_{REF},$$

$$\frac{R_{REF} \cancel{R_2}}{g} \left(1 + \frac{\cancel{R_4}}{\cancel{R_3}}\right) = \frac{R_1 \cancel{R_2}}{b} \left(1 + \frac{\cancel{R_4}}{\cancel{R_3}}\right) V_{REF},$$

$$\frac{R_{REF}}{g} = \frac{R_1}{b} V_{REF},$$

finally resulting in

$$R_{REF} = \frac{g V_{REF}}{b} R_1. \quad (2.10)$$

Also the relation for  $R_2$  can be expressed as a function of  $R_1$ , by rearranging equation

(2.9) and substituting the result from equation (2.7) and (2.10)

$$\begin{aligned}
 R_1 R_2 + R_1 R_{REF} + R_2 R_{REF} &= \frac{R_1 R_2}{b} \left( 1 + \frac{R_4}{R_3} \right) V_{REF}, \\
 R_1 R_2 + R_1 \frac{g V_{REF}}{b} R_1 + R_2 \frac{g V_{REF}}{b} R_1 &= \frac{R_1 R_2}{b} (1 + g) V_{REF}, \\
 \cancel{R_1} R_2 + R_1 \frac{g V_{REF}}{b} \cancel{R_1} + R_2 \frac{g V_{REF}}{b} \cancel{R_1} &= \frac{\cancel{R_1} R_2}{b} (1 + g) V_{REF}, \\
 R_2 + R_1 \frac{g V_{REF}}{b} + \cancel{R_2 \frac{g V_{REF}}{b}} &= R_2 \frac{V_{REF}}{b} + \cancel{R_2 \frac{g V_{REF}}{b}}, \\
 R_1 \frac{g V_{REF}}{b} &= R_2 \left( \frac{V_{REF}}{b} - 1 \right), \\
 R_2 &= \frac{\frac{g V_{REF}}{b}}{\frac{V_{REF}}{b} - 1} R_1,
 \end{aligned}$$

finally leading to

$$R_2 = \frac{g}{1 - \frac{b}{V_{REF}}} R_1. \quad (2.11)$$

As defined in the requirements, the laboratory set-up should be able to measure up to four different state variables, thus leading to four measurement channels. Three channels of the measuring amplifier ("type 1" amplifier), scale a differential input voltage of  $0V - 5V$  to a ground referenced output voltage of  $0V - 3.3V$  leading to a desired gain  $g = 0.66$  and a bias  $b = 0V$ . As no bias shift is needed, the reference voltage  $V_{REF}$  is not connected. Hence there is no resistor  $R_{REF}$  and equation (2.8) simplifies to

$$g = \frac{R_2}{R_1 + R_2} \left( 1 + \frac{R_4}{R_3} \right).$$

The remaining channel of the measuring amplifier ("type 2" amplifier), scales from  $-0.4V - 0.4V$  to  $0V - 3.3V$  leading to a desired gain  $g = 4.125$  and a bias  $b = 1.65V$ . Table 2.2 lists the component values for the two different types of amplifiers. The resistor values are calculated based on the derived relations, with the input resistors  $R_1$  and  $R_3$  chosen high enough, i.e. having no effect on the test circuits - also if high impedances are used. The values of the capacitors are identified based on simulation in order to obtain the desired anti-aliasing effect of the measuring amplifier. A

detailed step-by-step calculation of the resistor values is omitted here, as it is done similarly as in Section 2.4.1.3.

Since there are no special requirements for the operational amplifier, the *Microchip MCP6004*<sup>7</sup> is used. The amplifier is a standard four-channel rail-to-rail general-purpose amplifier which allows single supply.

amplifier	$R_1$	$R_2$	$R_3$	$R_4$	$R_{REF}$	$V_{REF}$	$C_1$	$C_2$
<i>type 1</i>	$1.5M\Omega$	$1M\Omega$	$1.5M\Omega$	$1M\Omega$	-	-	$100pF$	$100pF$
<i>type 2</i>	$100k\Omega$	$620k\Omega$	$100k\Omega$	$410k\Omega$	$1.22M\Omega$	$5V$	$150pF$	$150pF$

Table 2.2: Component values of the two differential amplifier types used in the measuring amplifier.

### 2.3.3.1 Amplifier parameters and Test Measurements

With the 12-bit ADC on the evaluation board and a designed measuring range of  $5V$  for the *type 1* differential amplifier the least significant bit (LSB) of the ADC corresponds to  $1.22mV$ , meaning a resolution of  $1.22mV$  for the whole measurement channel. Equally, this applies for the *type 2* differential amplifier with a measuring range of  $0.8V$  and consequently a resolution of  $0.195mV$ .

Figure 2.14 shows the test measurements of the measuring amplifier. As depicted therein, all amplifiers show the expected linear behaviour, although especially the *type 1* amplifiers have a slightly too high gain which leads to a slightly better resolution but smaller input range. The red lines show the fitted models according equation (2.5) using linear regression, whereas the ideal designed measuring amplifiers would exactly span the diagonal of the plots. The model parameters are summarised in Table 2.3.

channel	gain	bias
1 - type 1	$703.82 mV/V$	$2.68 mV$
2 - type 2	$4074.09 mV/V$	$1696.27 mV$
3 - type 1	$680.25 mV/V$	$-0.05 mV$
4 - type 1	$682.46 mV/V$	$2.38 mV$

Table 2.3: Fitted model parameters of the four different measurement amplifier channels.

<sup>7</sup><http://ww1.microchip.com/downloads/en/DeviceDoc/21733j.pdf>

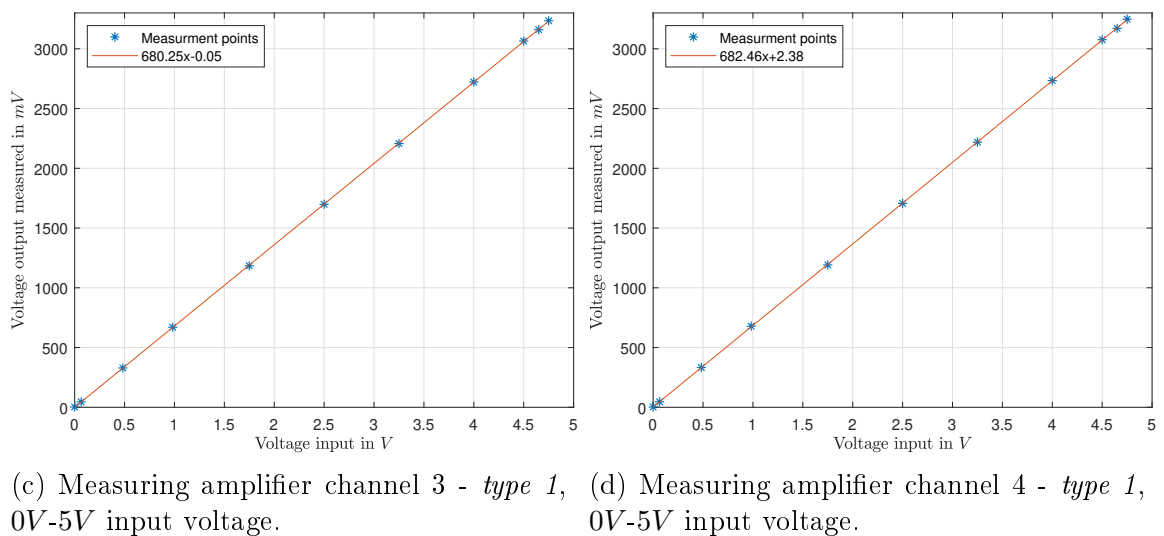
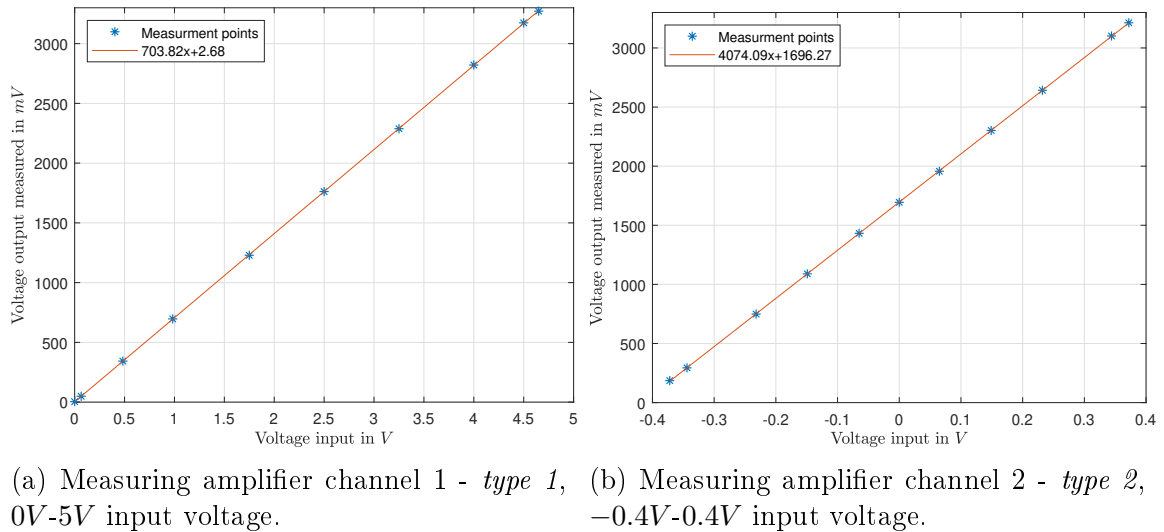


Figure 2.14: Test measurement of the four measuring amplifier channels.

### 2.3.4 Plugging Interface

The segmentation in three distinct components is an important feature of the laboratory set-up, as it provides a certain level of modularity. The task of the plugging interface is to easily connect respectively disconnect the three different parts, evaluation board, connector board and test circuits. Furthermore, the segmentation with a defined interface enables the design and implementation of further test circuits that simply need to be plugged in to work from a hardware perspective.

Since the connector board is "in the middle" of the laboratory set-up between the evaluation board and the test circuits, it has to connect the signal paths between them. As there are also two signal directions, the actuator signals from the evaluation board to the test circuits and the measurement signals from the test circuits

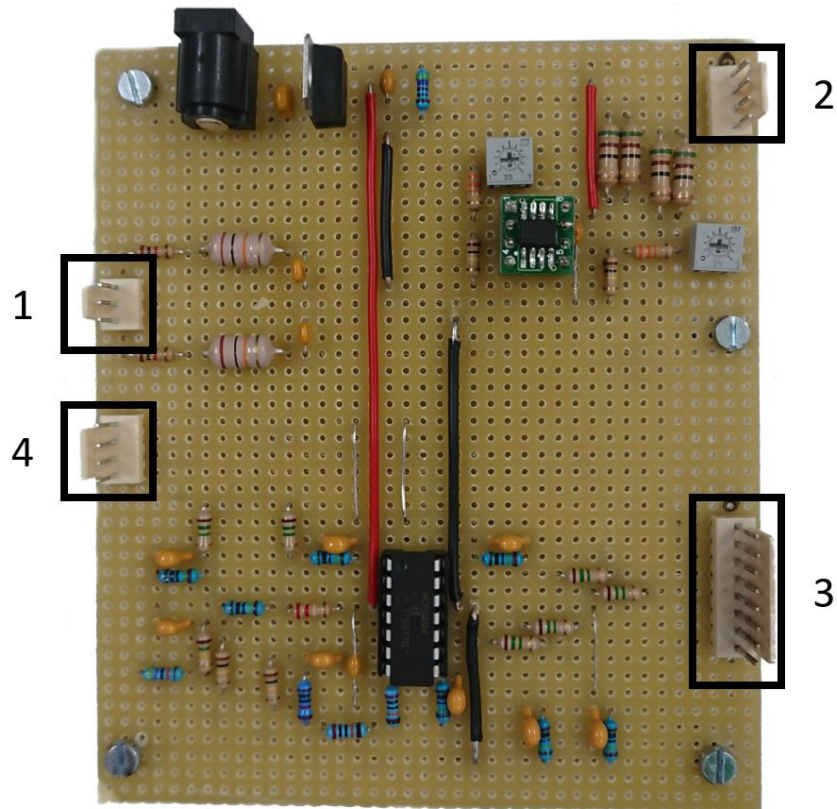


Figure 2.15: The four different sections of the plugging interface. The black dots above the plugs in section 2 and 3 indicate where the black signal must be located.

to the evaluation board, the plugging interface is divided into four sections

1. ground and actuator signals from evaluation board to connector board,
2. supply, ground and actuator signals from connector board to test circuits,
3. differential measurements from test circuits to connector board,
4. ground reference measurements from connector board to evaluation board.

There are corresponding counterparts of the interface on the test circuits. However, for the evaluation board the single wire-ends must be plugged in according to the used modules. The predefined pinout of the LAUNCHXL-F28069M is described in its user guide<sup>8</sup>.

Figure 2.15 shows the four connectors of the plugging interface as described above. The pinout of each of the interface sections is seen in Table 2.4, the used abbreviations are

- supply voltage  $V_+$ ,

<sup>8</sup><http://www.ti.com/lit/ug/sprui11b/sprui11b.pdf>

- common signal ground  $GND$ ,
- PWM outputs and signal driver inputs  $V_{PWM,i}$ ,
- signal driver outputs and test circuit inputs  $V_{S,i}$ ,
- differential measurements and measuring amplifier inputs  $V_{D,ix}$  and finally
- ground referenced outputs of the measuring amplifier and ADC inputs  $V_{M,i}$ .

section	pin 1	pin 2	pin 3	pin 4	pin 5	pin 6	pin 7	pin 8
1	$V_{PWM,1}$	$GND$	$V_{PWM,2}$	-	-	-	-	-
2	$V_+$	$GND$	$V_{S,1}$	$V_{S,2}$	-	-	-	-
3	$V_{D,1+}$	$V_{D,1-}$	$V_{D,2+}$	$V_{D,2-}$	$V_{D,3+}$	$V_{D,3-}$	$V_{D,4+}$	$V_{D,4-}$
4	$V_{M,1}$	$V_{M,2}$	$V_{M,3}$	$V_{M,4}$	-	-	-	-

Table 2.4: Pinout of the four sections of the plugging interface. The numbering of the pins for each section is done top to bottom, with *top* being considered according to Figure 2.15.

Each section of the plugging interface has an associated wire. The wires linking the evaluation board to the connector board have single jacks at side of the evaluation board and form-fitting jacks at the other side. The other two wires linking the connector board to the test circuits have form-fitting jacks at both ends. As seen in Figure 2.15, all plugging interface sections on the connector board have corresponding form-fitting plugs, ensuring that the wires can only be connected in one direction. However, for the wire linking to the test circuits, it is possible to plug in the wires incorrectly as not all jacks on the test circuits are form-fitting jacks. Hence, to reduce the risk of wrongly plugged connections there are black dots on the test circuits and on the connector board. These dots indicate the desired position of the black signal wire.

Figure 2.16 shows the fully connected laboratory set-up. As can be seen on the right side of the connector board in the middle, the black signal wires are located on the side of the black dots.

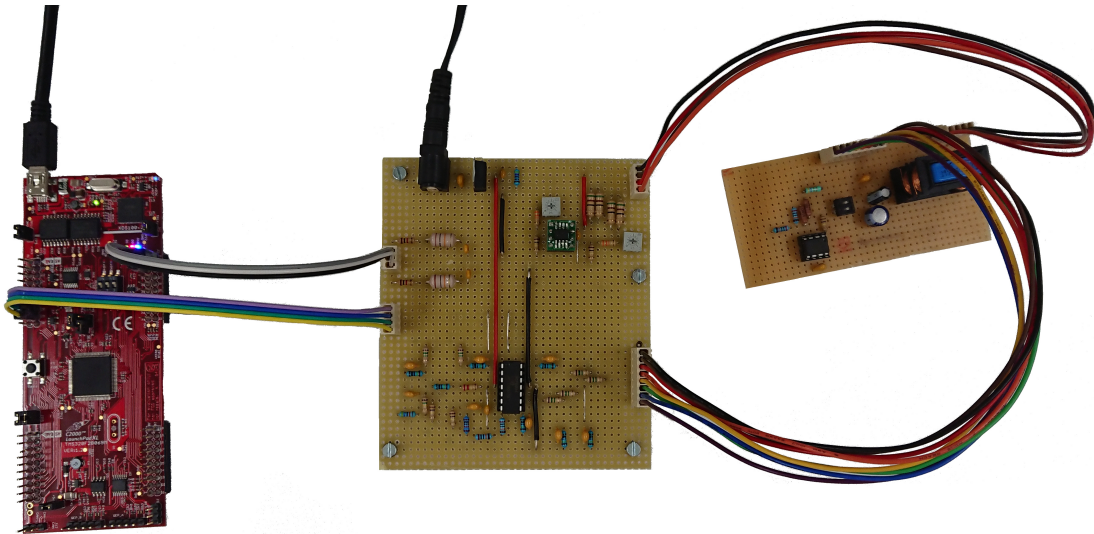


Figure 2.16: Fully wired laboratory set-up with the evaluation board on the left, the connector board in the middle and the series resonance circuit on the right side of the photo. The evaluation board is additionally connected to the host computer running Matlab Simulink, whereas the connector board is connected to an external power adapter.

## 2.4 Test Circuits

The test circuits represent the actual electronic circuits which are regarded as the plant. To demonstrate different controller and observer techniques, two simple test circuits are designed

- a RLC series resonance circuit and
- an integrator circuit.

Both circuits highlight different control problems and are easy to understand. The next subsections will explain the two different circuits in more detail.

### 2.4.1 Series Resonance Circuit

The series resonance circuit is a standard circuit in electrical engineering. Figure 2.17 shows the simplified structure of the RLC circuit. To retrieve information about the circuit's state there are two measurement points within the circuit. First, the voltage across the capacitor and second the voltage across the shunt resistor. The shunt voltage is used to indirectly measure the inductor current which equals the current through the circuit. To obtain an interesting control task, the circuit must be designed that the voltage across the capacitor naturally overshoots when applying an input step.

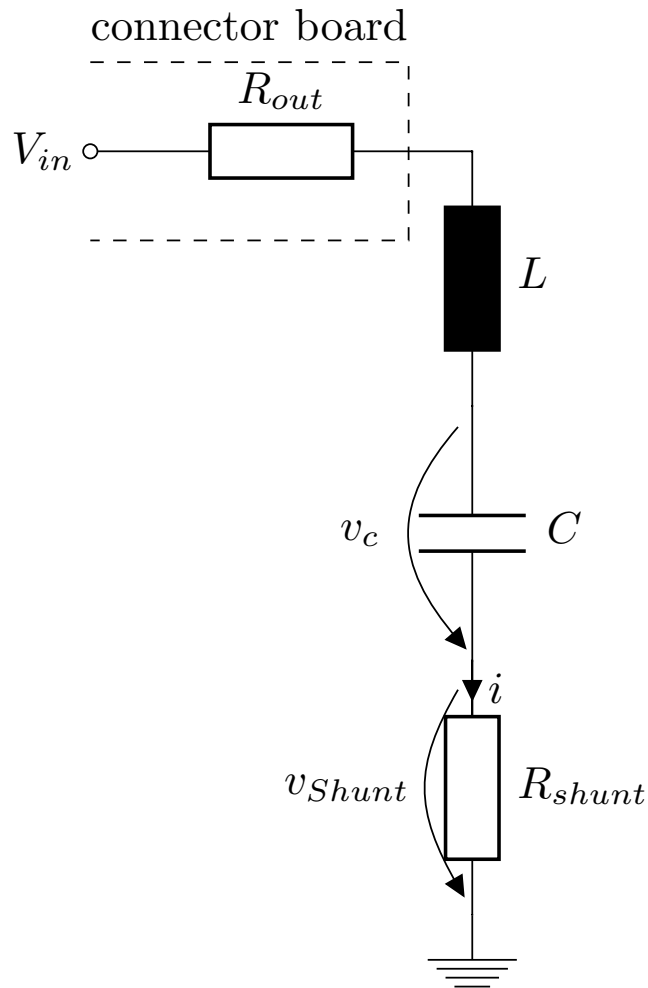


Figure 2.17: Simplified circuit diagram of the RLC series resonance circuit.

#### 2.4.1.1 State-Space Modelling

The state space model of the circuit is derived using Kirchoff's voltage law and the voltage-current relations of the inductor and capacitor

$$V_{in} = i(R_{out} + R_{shunt}) + v_L + v_C, \quad (2.12)$$

$$v_L = L \frac{d}{dt} i_L, \quad (2.13)$$

$$i = i_L = i_C = C \frac{d}{dt} v_C.$$

Inserting equation (2.13) in (2.12) results

$$V_{in} = i_L (R_{out} + R_{shunt}) + L \frac{d}{dt} i_L + v_C. \quad (2.14)$$



Rearranging equation (2.13) and (2.14) and setting  $R = R_{out} + R_{shunt}$  results first-order differential equations of the form

$$\frac{d}{dt}v_C = \frac{1}{C}i_L, \quad (2.15)$$

$$\frac{d}{dt}i_L = -\frac{1}{L}v_C - \frac{R}{L}i_L + \frac{1}{L}V_{in}. \quad (2.16)$$

With the given system equations (2.15) and (2.16), the circuit can be represented as linear time-invariant system (*LTI system*) of the form

$$\begin{aligned} \frac{d}{dt}\mathbf{x} &= \mathbf{A}\mathbf{x} + \mathbf{b}u, \\ y &= \mathbf{c}^T\mathbf{x}, \end{aligned}$$

with the system matrix  $\mathbf{A}$ , the input vector  $\mathbf{b}$  corresponding to the input  $u$  and the system state  $\mathbf{x}$ . The system output  $y$  is obtained using the state  $\mathbf{x}$  and the associated output vector  $\mathbf{c}^T$ .

The final model for the RLC series resonance circuit is given by

$$\mathbf{x} = \begin{bmatrix} v_C \\ i_L \end{bmatrix}, \quad u = V_{in},$$

$$\frac{d}{dt}\mathbf{x} = \begin{bmatrix} 0 & \frac{1}{C} \\ -\frac{1}{L} & -\frac{R}{L} \end{bmatrix} \mathbf{x} + \begin{bmatrix} 0 \\ \frac{1}{L} \end{bmatrix} u, \quad (2.17)$$

$$y = [1 \quad 0] \mathbf{x},$$

hence it is assumed that  $y = v_C$ .

### 2.4.1.2 Component Dimensioning

With the state space model (2.17) it is however hard to design the circuit to meet the requirements. Therefore, a structured approach is taken using the input output relations in the frequency domain where  $V_{in}$  is the input and  $v_C$  the output.

First Kirchhoff's voltage law is used again, this time however the frequency dependent resistance of the components is used

$$\begin{aligned} V_{in}(s) &= Ri_L(s) + sLi_L(s) + \frac{1}{sC}i_L(s), \\ V_{in}(s) &= i_L(s) \left[ R + sL + \frac{1}{sC} \right]. \end{aligned} \quad (2.18)$$

The current voltage relation of the capacitor in the frequency domain given as

$$i_L(s) = C s v_C.$$

Thus, equation (2.18) can further be expanded

$$\begin{aligned} V_{in}(s) &= C s v_C \left[ R + sL + \frac{1}{sC} \right], \\ V_{in}(s) &= u_C [sRC + s^2LC + 1], \\ \frac{u_C}{V_{in}} &= \frac{1}{s^2LC + sRC + 1}, \end{aligned}$$

leading to

$$\frac{u_C}{V_{in}} = \frac{1}{LC} \frac{1}{s^2 + s\frac{R}{L} + \frac{1}{LC}}. \quad (2.19)$$

This transfer function can also be obtained using the state-space model (2.17)

$$G(s) = \mathbf{c}^T (s\mathbf{E} - \mathbf{A})^{-1} \mathbf{b}.$$

Equation (2.19) equals a second-order system with complex conjugate pole pair

$$P(s) = \frac{1}{s^2 + 2d\omega_n s + \omega_n^2}. \quad (2.20)$$

These types of systems are well studied and it is known that for a damping factor  $d < 1$  the system response due to a step input shows an overshoot. A comparison of the coefficients in equations (2.19) and (2.20) shows that

$$\frac{R}{L} = 2d\omega_n \quad (2.21)$$

and

$$\omega_n = 2\pi f_n = \frac{1}{\sqrt{LC}}. \quad (2.22)$$

The frequency  $f_n$  and the damping factor  $d$  are chosen as  $80Hz$  and  $0.1$ . With these two values and equation (2.21) it is possible to calculate the inductance

$$L = \frac{R}{2d\omega_n}.$$

With a measured output resistance of  $31.7\Omega$  (Table 2.1) and a chosen  $5\Omega$  shunt resistor the value of the inductance is calculated as

$$\begin{aligned}\frac{R}{L} &= 2d\omega_n \\ L &= \frac{R}{2d\omega_n} = \frac{31.7\Omega + 5\Omega}{2 \cdot 0.1 \cdot 2\pi \cdot 80Hz} \\ L &= 0.3651H.\end{aligned}$$

Thus a  $0.4H$  inductance is used. The capacitor value is then derived using equation (2.22)

$$\begin{aligned}\omega_n &= \frac{1}{\sqrt{LC}}, \\ C &= \frac{1}{L\omega_n^2} = \frac{1}{0.4H \cdot (2 \cdot \pi \cdot 80Hz)^2}, \\ C &= 9.89\mu F.\end{aligned}$$

The capacitor is since chosen as  $10\mu F$ , which leads to a frequency  $f_n = 79.58Hz$ .

To double check if the chosen parameters lead to a damping factor  $d < 1$ , equation (2.22) is inserted into (2.21) and solved for  $d$

$$\begin{aligned}\frac{R}{L} &= 2d\frac{1}{\sqrt{LC}}, \\ d &= \frac{R\sqrt{LC}}{2L} = \frac{R\sqrt{C}}{2\sqrt{L}}, \\ d &= \frac{36.7\Omega \cdot \sqrt{10\mu F}}{2 \cdot \sqrt{0.4H}}, \\ d &= 0.0918.\end{aligned}$$

In order to change the circuit characteristics in a straight forward way, two additional capacitors are wired in parallel to the given capacitor as seen in Figure 2.18. The extra capacitors can be added to the circuit independently via switches. By wiring the capacitors parallel the values of the capacitors add up and it can be seen as one bigger capacitor in the model.

$L$	$R_{shunt}$	$C$	$C_2$	$C_3$
$0.4H$	$5\Omega$	$10\mu F$	$22\mu F$	$47\mu F$

Table 2.5: Component values of the series resonance circuit.

Table 2.5 shows the component values for the RLC series resonance circuit. With both capacitors added to the circuit, the maximum capacitance  $C_{max} = 79\mu F$ .

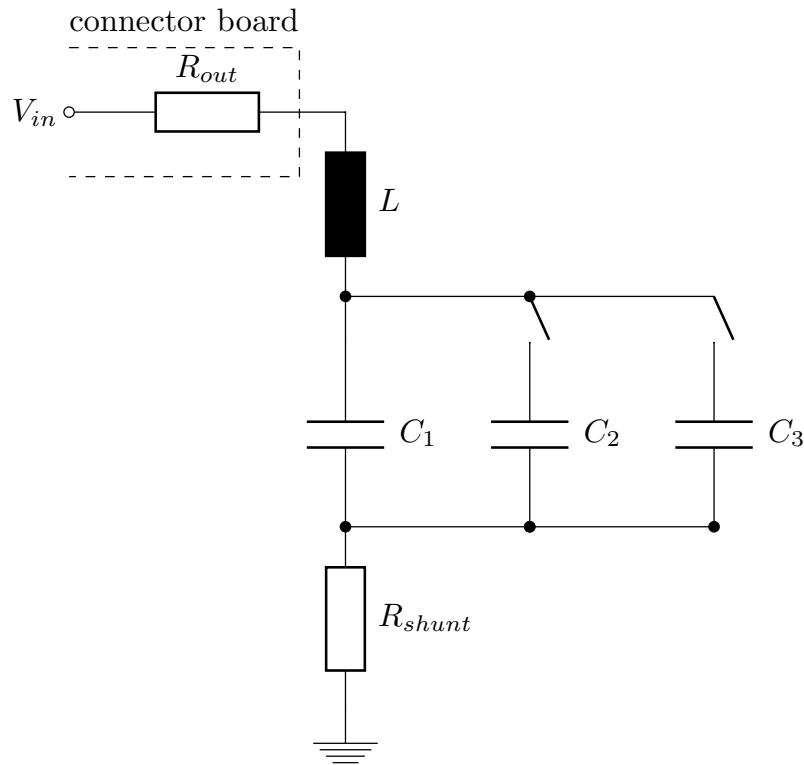


Figure 2.18: Circuit diagram of the RLC series resonance circuit with switchable capacitors.

Again calculating the damping factor  $d$  using equations (2.21) and (2.22) results

$$d = \frac{R\sqrt{C_{max}}}{2\sqrt{L}},$$

$$d = \frac{36.7\Omega \cdot \sqrt{79\mu F}}{2 \cdot \sqrt{0.4H}},$$

$$d = 0.257,$$

which still allows an overshoot in the system's step response. The resonance frequency  $f_n$  for the maximum capacitance is

$$f_{n,Cmax} = \frac{1}{2\pi\sqrt{LC_{max}}},$$

$$f_{n,Cmax} = \frac{1}{2 \cdot \pi \cdot \sqrt{79\mu F \cdot 0.4H}},$$

$$f_{n,Cmax} = 28.3Hz.$$

The addition of the two capacitors allows to test the different controllers with a "faster" or "slower" circuit. Furthermore, there is no need to change parts, but only to toggle a switch and the system dynamics change.

### 2.4.1.3 Shunt Voltage Amplification

With the series resonance circuit design from the previous section, the final circuit was simulated using MATLAB Simscape. Figures 2.19 and 2.20 show the simulation set-up and results for the shunt voltage for  $4V$  steps at the input. Since the system is designed to overshoot, an input step of  $4V$  is considered as maximum admissible amplitude in order to stay within, or just above the  $5V$  voltage range. From the measuring amplifier parameter (Section 2.3.3.1) the resolution of the *type 1* channels is known to be  $1.22mV$ . Especially Figure 2.20a shows that this may lead to problems when controlling the circuit, since the signal is only exploiting a very small region of the measuring range. Although the *type 2* channel has a much better resolution, the signal only spans half of the measuring range, thus, loosing accuracy of the measurements.

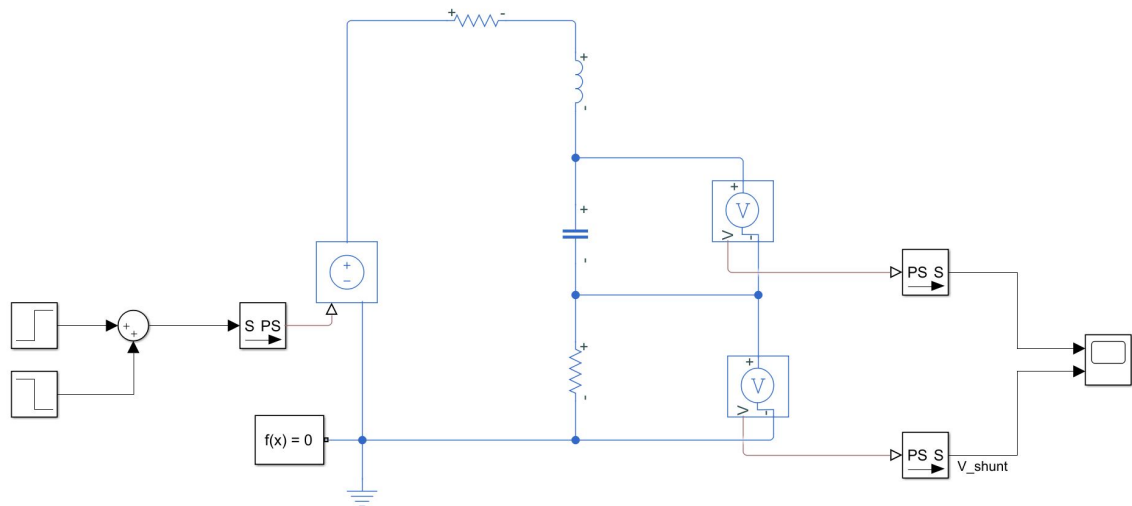


Figure 2.19: MATLAB Simscape simulation set-up for the series resonance circuit.

Hence, the shunt voltage is amplified to exploit most of the measuring range. An increase of the shunt resistor is not feasible since this would damp the series resonance circuit.

The differential amplifier design as shown in Figure 2.21 is similar to the one of the measuring amplifier, there are just no capacitors as no low-pass filter functionality is needed for this task.

Figure 2.20b shows that the maximum amplitude is slightly over  $0.2V$ , this leads to an input range of  $-0.25V - 0.25V$ . The signal should exploit most of the measurement range of  $5V$  for the *type 1* measuring channels. From the test measurements (Figure 2.14 it can be seen that these channels work approximately up to  $4.9V$ ). Thus, the designed amplifier should span the output range from  $0.1V - 4.9V$ . This results in a gain of

$$g = \frac{4.8V}{0.5V} = 9.6.$$

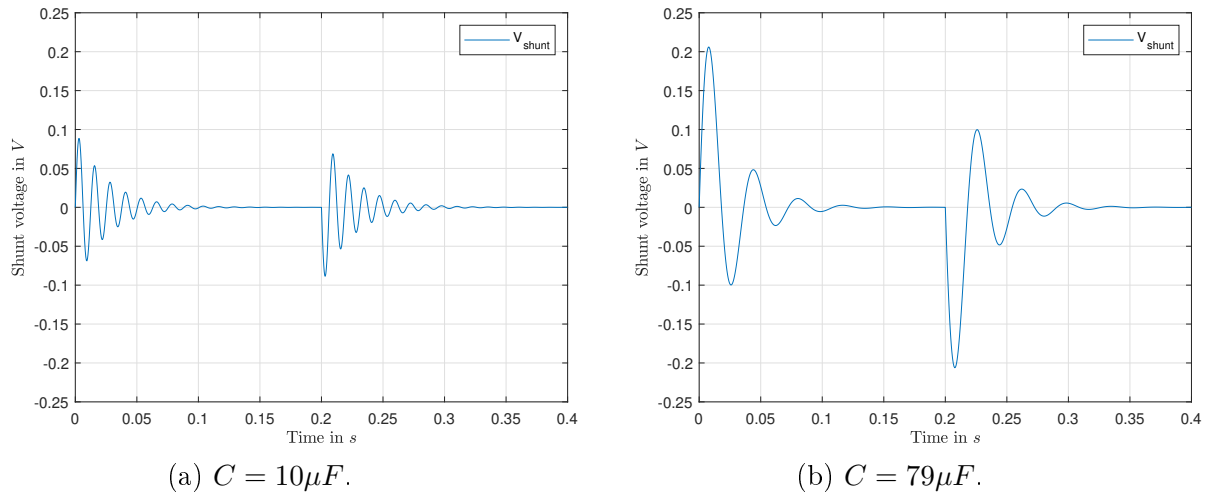


Figure 2.20: Series resonance circuit shunt voltage simulation results with  $\pm 4V$  input steps.

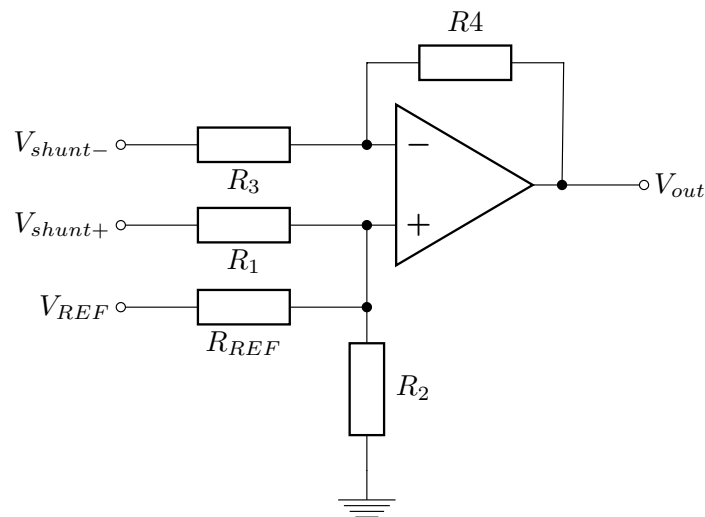


Figure 2.21: Circuit diagram of the differential amplifier used for amplification of the shunt voltage.

The amplifier also needs to shift the shunt voltage solely to be positive, hence, a bias of  $2.5V$  is applied.

For the circuit design equations (2.7), (2.10) and (2.11) are utilised. To choose the input resistors of the amplifier sufficiently high, the resistance of the capacitor is

calculated first. For the minimum capacitance this results

$$\begin{aligned} X_C &= \frac{1}{\omega_n C_1}, \\ X_C &= \frac{1}{2\pi \cdot 79.58 \cdot 10\mu F}, \\ X_C &= 200\Omega \end{aligned}$$

and consequently

$$\begin{aligned} X_{Cmax} &= \frac{1}{\omega_{n,Cmax} C_{max}}, \\ X_{Cmax} &= \frac{1}{2\pi \cdot 28.3 \cdot 79\mu F}, \\ X_{Cmax} &= 71.19\Omega \end{aligned}$$

for the maximum capacitance.

Thus, by choosing the resistors  $R_1 = R_3 = 10k\Omega$  the amplifier will not infer the actual serial resonance circuit and the calculation of the remaining resistors can be done.

The feedback resistor  $R_4$  of the inverting amplifier hence calculates according to equation (2.7) as

$$\begin{aligned} R_4 &= gR_3 = 9.6 \cdot 10k\Omega, \\ R_4 &= 96k\Omega, \end{aligned}$$

and is finally chosen as  $R_4 = 100k\Omega$ .

The ground resistor  $R_2$  of the non-inverting amplifier utilises equation (2.11), i.e.

$$\begin{aligned} R_2 &= \frac{g}{1 - \frac{b}{V_{REF}}} R_1, \\ R_2 &= \frac{9.6}{1 - \frac{2.5V}{5V}} 10k\Omega, \\ R_2 &= 192k\Omega, \end{aligned}$$

which leads to a ground resistance  $R_2 = 200k\Omega$ .

Finally, resistor  $R_{REF}$  for the reference voltage is calculated using equation (2.10)

$$\begin{aligned} R_{REF} &= \frac{gV_{REF}}{b} R_1, \\ R_{REF} &= \frac{9.6 \cdot 5V}{2.5V} 10k\Omega, \\ R_{REF} &= 192k\Omega, \end{aligned}$$

therefore choosing  $R_{REF} = 200k\Omega$ .

Table 2.6 summarises the used resistor values, with the resulting gain  $g = 10$  and bias  $b = 2.5V$ . As operational amplifier the *Microchip MCP6002*<sup>9</sup> is used. It is a general-purpose rail-to-rail amplifier from the same product family as the previously used *Microchip MCP6004* in the measuring amplifier. As only one channel of the operational amplifier is used, the second channel is wired as unity gain buffer, with the input coupled to the positive input of the first channel. This prevents any drawbacks on the used channel.

$R_1$	$R_2$	$R_3$	$R_4$	$R_{REF}$
$10k\Omega$	$200k\Omega$	$10k\Omega$	$100k\Omega$	$200k\Omega$

Table 2.6: Resistor values of the shunt voltage amplifier.

#### 2.4.1.4 Simulink Integration and Signal Flow

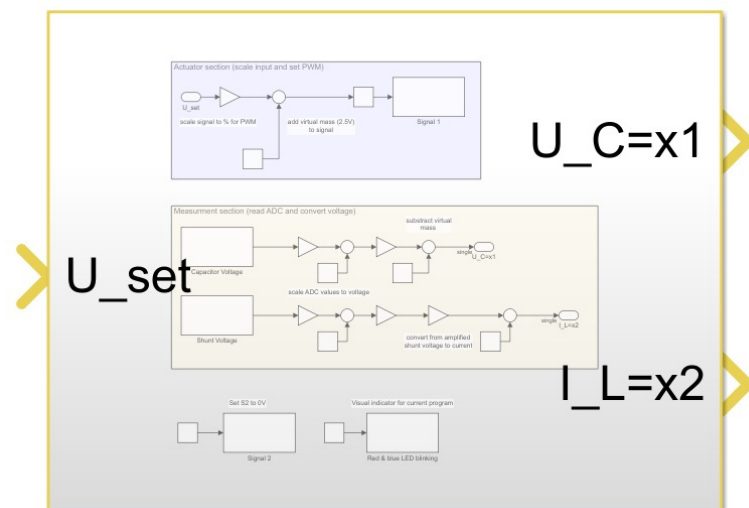


Figure 2.22: Abstracted MATLAB Simulink integration block of the serial resonance circuit. The block has one input and outputs the two state variables.

The given serial resonance circuit also needs to be integrated into MATLAB Simulink. Figure 2.22 shows the Simulink *series resonance circuit integration block* (SRCI-block). As in the state-space model (2.17), the SRCI-block has one input. The outputs are the two measured state variables, i.e. the voltage across the capacitor and the current through the circuit, with the system output  $y = x_1$  being the first variable. The block abstraction allows to easily exchange the integrated real-world model with a simulated state-space block without the need to change the outer model structure.

<sup>9</sup><http://ww1.microchip.com/downloads/en/DeviceDoc/21733j.pdf>



As indicated in Section 2.2.1 about the MATLAB Simulink compatibility of the evaluation board, when using the TI hardware support package, the model needs to be run in *external mode* to exchange data between the evaluation board and the host computer.

In Figure 2.23 the inner structure of the SRCI-block is shown in detail. The Simulink block diagram can be divided into an upper actuation section and a lower measuring section.

Since the voltage range of the signal driver is between  $0V$  and  $5V$  it is not possible to output a negative voltage. With the *type 1* channels of the measuring amplifier having the same range of  $0V - 5V$  as input, it is also not possible to measure a negative capacitor voltage. Hence, an input and state transformation is performed within the SRCI-block, as the input voltage and capacitor voltage virtually considered  $0V$  at an actual voltage of  $2.5V$ . Equations (2.23) and (2.24) illustrate this transformation.

$$V_{in,virtual} = V_{in} - 2.5V \quad (2.23)$$

$$x_{1,virtual} = x_1 - 2.5V \quad (2.24)$$

However, as the transformation is linear and the system is linear time-invariant, the transformation has no impact on the system behaviour. From "outside" the SRCI-block it looks as if the system operates in a range between  $-2.5V - 2.5V$ , whereas in real it operates between  $0V - 5V$ . There is no meaningful technical background for this transformation, it is just taken to handle with zero based signals.

The SRCI-block also hides the shifts between the  $3.3V$  domain of the evaluation board and the  $5V$  domain of the connector board and test circuits, which will also be explained in the next paragraphs.

Looking at Figure 2.23, the light blue actuator section takes the given input voltage and scales it into a percentage of the  $5V$  actuation range. Then the shift of the input voltage is performed. By adding 50% the addition of  $2.5V$  to convert from the virtual input voltage to the real input voltage is realised. The resulting percentage is then passed to a saturation function, where plant limitations for the input signal are considered. Finally, the percentage reaches the ePWM block of the *TI C2000 Piccolo Support from Embedded Coder hardware support package* highlighted in red. The ePWM block offers various different setting options for counter modes, period, etc. The settings of a PWM frequency of  $200kHz$  and up-counting mode are selected. The pin of the PWM can be chosen according the pinout of the  $\mu C$ . Eventually the ePWM block sets the ePWM output pin of the evaluation board with a duty cycle according to the given percentage. To further illustrate the signal path, the PWM signal is then processed by the signal driver of the connector board where the signal is digital-analogue converted, scaled and finally forwarded to the test circuit.

The whole signal flow is demonstrated by the following example. For instance a

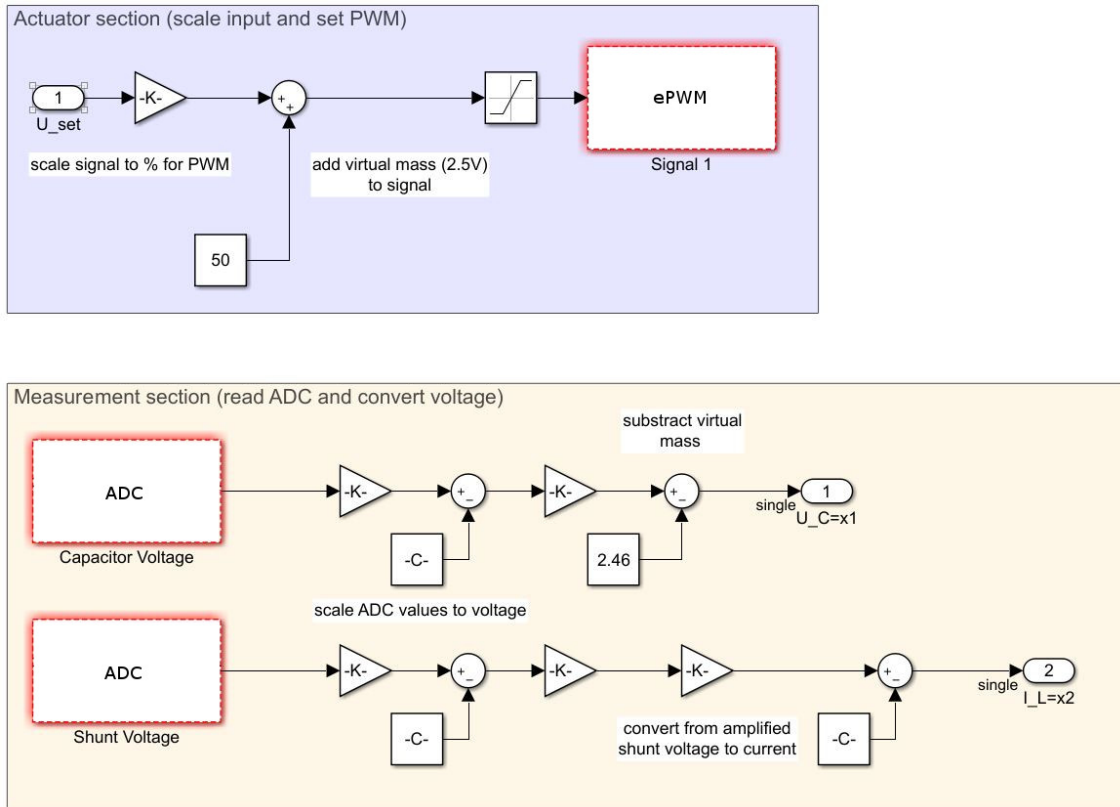


Figure 2.23: Block diagram of the MATLAB Simulink model for the serial resonance circuit integration. The structure of the test circuit integration block is divided into two sections, the upper actuator section in light blue and the lower measurement section in yellow. The ADC and ePWM blocks as parts of the *TI C2000 Piccolo Support from Embedded Coder hardware support package* are highlighted in red.

control algorithm sets  $1V$  input voltage at the input of the SRCI-block. In the block the signal is scaled to a percentage

$$1V/5V \cdot 100\% = 20\%.$$

Then the 50% input voltage shift is performed, i.e.

$$20\% + 50\% = 70\%,$$

followed by a possible action of the saturation function. After that, a  $3.3V$  PWM signal with 70% duty cycle is forwarded from the evaluation board to the LPF of the connector boards signal driver. The LPF performs a digital-analogue conversion of the signal

$$70\% \cdot 3.3V = 2.31V.$$

The resulting voltage is then amplified by the non-inverting amplifier of the signal driver with a factor of 1.52

$$2.31V \cdot 1.52 = 3.5V.$$

The final voltage of  $3.5V$  is then forwarded to the test circuit and equals exactly  $1V$  above the virtual zero of  $2.5V$  and 70% of the  $5V$  domain.

The flow of the two measurement signals, seen in the lower, yellow measurement section of Figure 2.23 is in opposite direction. The signals are taken from the test circuit, low-pass filtered and scaled via the measurement amplifier channels on the connector board and forwarded to the ADC pin on the evaluation board where the hardware path of the signals ends. Highlighted in red, the two ADC blocks of the *TI C2000 Piccolo Support from Embedded Coder hardware support package* convert the real-world signals to 12-bit integer values, with the ADC block set to  $1kHz$  sampling rate in continuous mode with internal reference voltage. The pin can again be chosen according the pinout of the  $\mu C$ . The resulting integer values are then translated to quantised voltage levels. Next is the backwards translation from the measuring amplifier, where the bias is subtracted and the results are divided by the amplifier gains - each signal according to its channel's parameters given in Table 2.3. Then the state transformation is done for the capacitor voltage and similarly the shunt voltage is converted to the circuits current, also considering the amplification and bias shift of the shunt voltage amplification.

Giving also an example for this case, the  $4V$  capacitor voltage is measured and scaled with channel 1 of the measuring amplifier on the connector board, i.e.

$$4V \cdot 0.70382 + 0.00268V = 2.818V.$$

The signal is measured with the ADC of the evaluation board and quantised

$$2.818V \hat{=} 3498.$$

Then the inverting procedure starts in Simulink, where first the ADC integer value is translated to a quantised voltage based on the ADC reference voltage of  $3.3V$ ,

$$\frac{3498}{4096} \cdot 3.3V = 2.818V.$$

The bias of the measuring amplifier channel 1 is subtracted from the voltage followed by a division of the channels gain

$$\frac{2.818V - 0.00268V}{0.70382} = 4V.$$

Finally, the state transformation is performed resulting a virtual output voltage of

$$4V - 2.5V = 1.5V.$$

#### 2.4.1.5 Final Series Resonance Circuit and Model Verification

Figure 2.24 shows the soldered series resonance circuit with wiring interfaces and shunt voltage amplification. The  $2.54mm$  pin strips allow easy and fast connection and disconnection of the test circuits, with the black dots indicating where the black signal wire must be located.

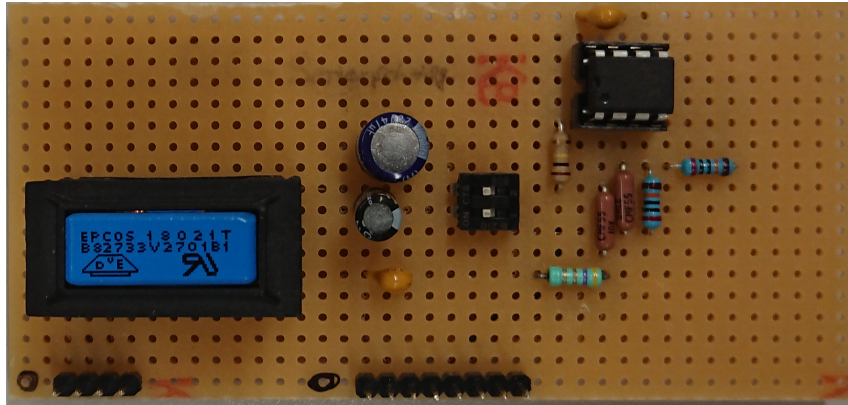


Figure 2.24: Implementation of the designed series resonance circuit with shunt voltage amplification. On the bottom are the wiring interfaces to the connector board with input & supply left and measurements on the right. Above from left to right are the inductor, the capacitors, the switches and the shunt resistor (turquoise) with the shunt voltage amplifier above.

Most left in blue is the inductor. As from the calculations in the previous sections, the coil should have  $0.4H$ . Since its given availability in the laboratory, the TDK B82733V2701B001<sup>10</sup> was used. The part features two  $0.1H$  inductors with 200 windings each and a ferrite core. By cross-connecting both inductors in series, the number of windings doubles. Thus, with the number of windings quadratically entering the inductance equation, the inductance quadruples to the desired  $0.4H$ .

Next to the inductor are the three capacitors  $C_1 = 10\mu F$ ,  $C_2 = 22\mu F$  and  $C_3 = 47\mu F$  (from bottom to top). The latter two capacitors can easily switched on and off using the switch next right.

On the right side of the circuit board is the shunt resistor in light turquoise with the amplification circuit above. The measured voltage across the capacitor is directed to the first measurement channel and the amplified shunt voltage to the third measurement channel.

A full circuit diagram of the series resonance circuit can be found in appendix.

To verify the behaviour of the soldered series resonance circuits test measurements were performed. Figures 2.25 and 2.26 show the results of the model verification with a capacitance  $C = C_{max} = 79\mu F$ . For the verification, the simulated model and the test circuit are run simultaneously as open-loop. Both blocks are fed with the same rectangular input signal of  $1V$  amplitude. The simulated and measured outputs are then visualised in the above mentioned figures. As can be seen, the test-circuit does not differ much from the simulated model. Especially when looking at the resonance frequency that can be seen in the overshooting, the model and test circuit match pretty well. Only the amplitude of overshooting deviates slightly from

<sup>10</sup>[https://www.tdk-electronics.tdk.com/inf/30/db/ind\\_2008/b82733f.pdf](https://www.tdk-electronics.tdk.com/inf/30/db/ind_2008/b82733f.pdf)

the model, however, this can be explained with deviations in the circuits resistance and the non-modelled hysteresis of the inductor as it utilises a ferrite core.

It is also worth noting, that the measurement noise of the laboratory set-up is quite low, therefore, not affecting any of the later performed control and observation tasks.

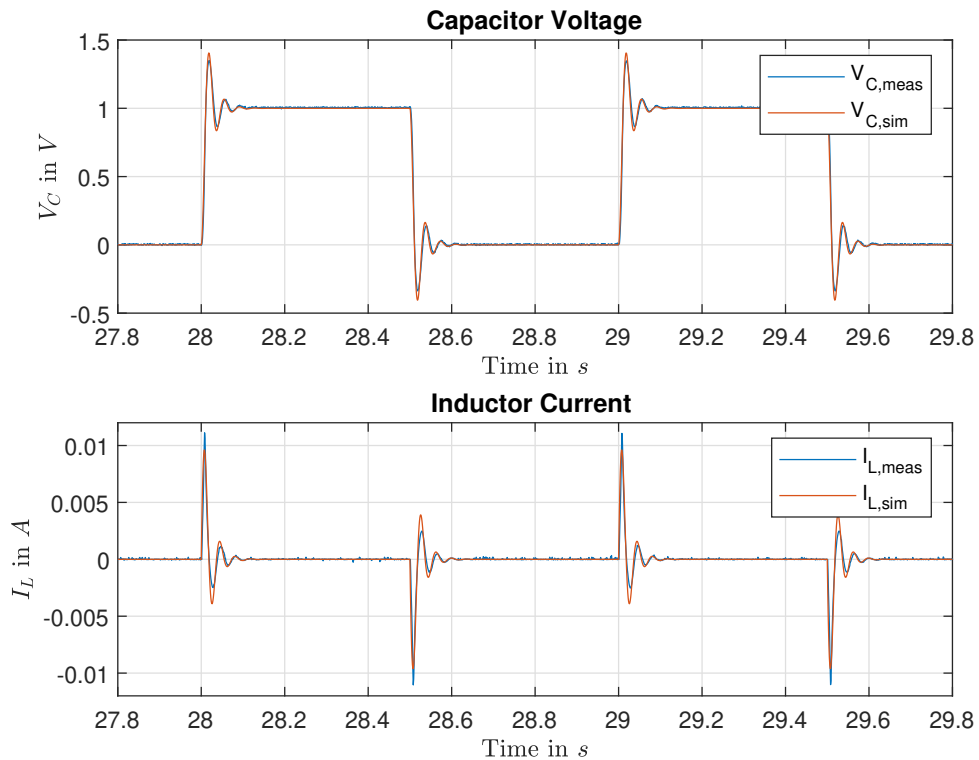


Figure 2.25: Comparison of the simulated model (orange) and the measured test circuit values (blue). Top, the capacitor voltage  $V_C$  and bottom the inductor current  $I_L$  for a rectangular input signal of 1V amplitude.

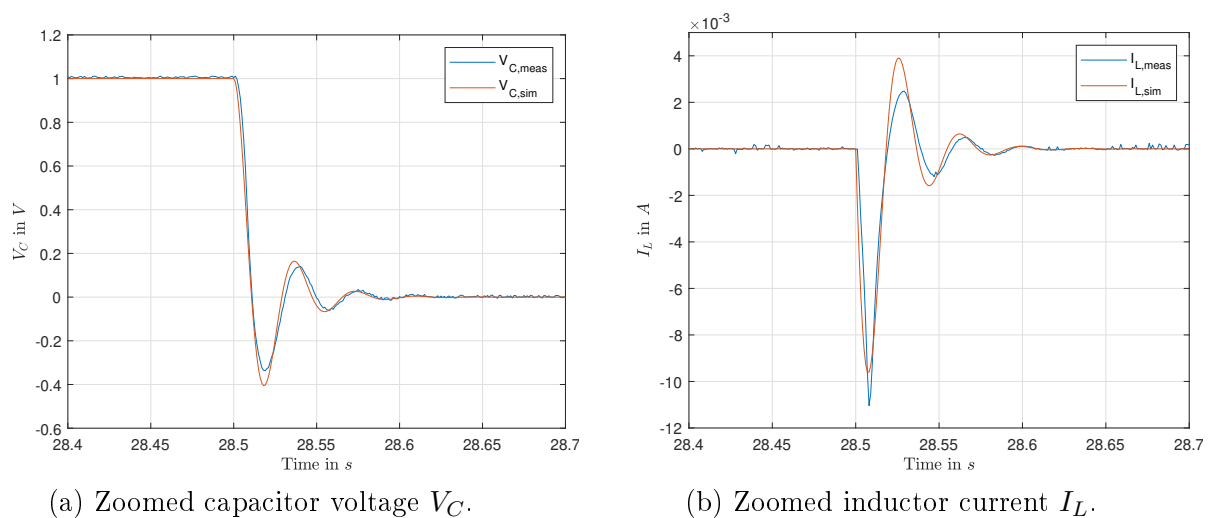


Figure 2.26: Detailed comparison of the simulated model (red) and the measured test circuit values (blue).

## 2.4.2 Integrator

The second implemented test circuit is a simple inverting integrator using an operational amplifier. Figure 2.27 shows the simplified circuit diagram of the integrator. To validate robustness and disturbance attenuation, it should also be possible to apply perturbations to the test circuit. Therefore, the integrator has two inputs, where one is considered as regular input and the other one as unknown disturbance.

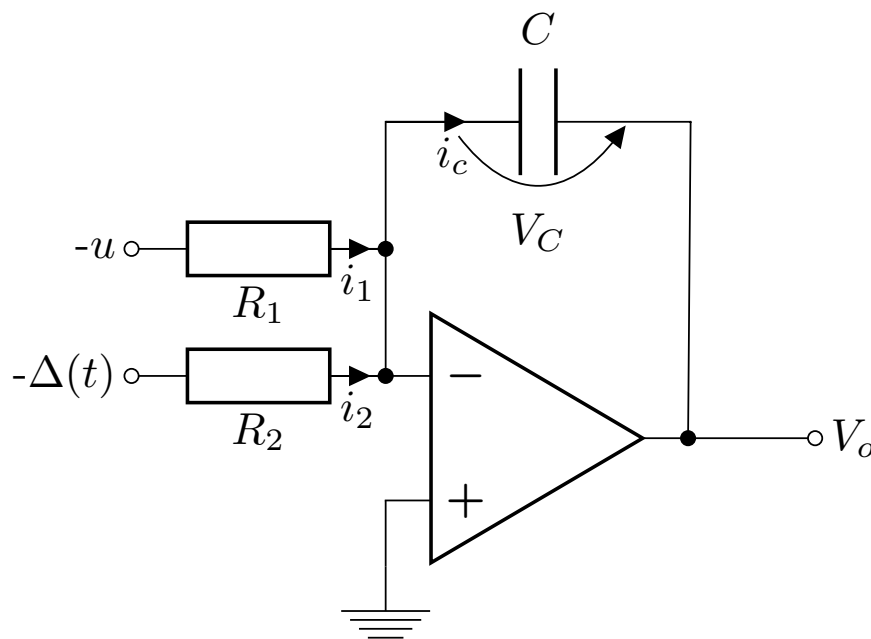


Figure 2.27: Simplified circuit diagram of the integrator. As the integrator inverts the signals, they are inverted as well. The lower input is considered as unknown perturbation.

### 2.4.2.1 State-Space Modelling

The modelling of the given integrator circuit is straight forward using the circuits current relations. The positive input of the operational amplifier is connected to ground. With the negative feedback path driving the differential voltage between the amplifiers inputs to zero, the negative input is hold at ground level. In literature this point is often referred as *virtual ground*. Using the superstition principle, the input  $-u$  is excited, whereas the input  $-\Delta(t)$  set to ground. As both sides of the resistor  $R_2$  are grounded, no current will flow and infer the remaining circuit.

By exiting input  $-u$ , a current  $i_1$  will be driven to the virtual ground. As no current flows into the operational amplifier and through the resistor  $R_2$ , the same current

must flow through the capacitor. This leads to

$$\begin{aligned} i_1 &= i_{C,1}, \\ \frac{-u}{R_1} &= C \frac{d}{dt} V_{C,1}, \\ \frac{d}{dt} V_{C,1} &= -\frac{1}{R_1 C} u, \\ \frac{d}{dt} V_{O,1} &= \frac{1}{R_1 C} u. \end{aligned}$$

The relations for the second input  $-\Delta(t)$  can be derived in the same way resulting in

$$\frac{d}{dt} V_{O,2} = \frac{1}{R_2 C} \Delta(t).$$

This leads to a combined output voltage of

$$\begin{aligned} \frac{d}{dt} V_O &= \frac{d}{dt} V_{O,1} + \frac{d}{dt} V_{O,2}, \\ \frac{d}{dt} V_O &= \frac{1}{R_1 C} u + \frac{1}{R_2 C} \Delta(t). \end{aligned} \tag{2.25}$$

By using the same resistor values  $R_1 = R_2 = R$  equation (2.25) simplifies to

$$\frac{d}{dt} V_O = \frac{1}{RC} [u + \Delta(t)]. \tag{2.26}$$

Integrating equation (2.26) leads to

$$V_O = V_O(0) + \frac{1}{RC} \int_0^t [u + \Delta(\tau)] d\tau,$$

clearly highlighting the circuit's integrating behaviour.

The state-space model can easily be derived using equation (2.26) leading to

$$\begin{aligned} x &= V_O, \quad u = u, \\ \frac{d}{dt} x &= \frac{1}{RC} u + \frac{1}{RC} \Delta(t), \\ y &= x. \end{aligned} \tag{2.27}$$

This equals a LTI system of the form

$$\begin{aligned} \frac{d}{dt} \mathbf{x} &= \mathbf{A} \mathbf{x} + \mathbf{b} u + \mathbf{b} w, \\ y &= \mathbf{c}^T \mathbf{x}, \end{aligned}$$

with  $\mathbf{A} = 0$ ,  $\mathbf{b} = \frac{1}{RC}$ ,  $\mathbf{c}^T = 1$  and input disturbance  $w = \Delta(t)$ .

### 2.4.2.2 Component Dimensioning

For the dimensioning of the integrator there are no special restrictions to be considered. However, it is practicable that the integrator does not drive the supply range of  $5V$  too fast. Therefore, a time of  $0.5s - 1s$  is targeted for an input  $u = 1V$ .

When considering the frequency domain, the frequency response of the integrator reads as

$$V_O = \frac{1}{j\omega RC}u.$$

As commonly known, the magnitude plot of an integrator decreases constantly with  $-20dB/decade$ , with the frequency at a gain of 1 is called gain crossover frequency. To keep things easy, a gain crossover frequency  $f_C = 1Hz$  is aimed.

The time constant  $\tau$  of the integrator is given by

$$\tau = RC.$$

The gain crossover frequency  $f_C$  is linked to the time constant  $\tau$  as follows

$$f_C = \frac{1}{2\pi\tau}.$$

This leads to a time constant  $\tau$

$$\begin{aligned} f_C &= \frac{1}{2\pi\tau}, \\ \tau &= \frac{1}{2\pi f_C} = \frac{1}{2\pi \cdot 1Hz}, \\ \tau &= 0.159s. \end{aligned}$$

Using a capacitor  $C = 1\mu F$  and a resistor  $R = 150k\Omega$  finally results a time constant  $\tau = 0.15s$  and consequently a crossover frequency of

$$\begin{aligned} f_C &= \frac{1}{2\pi\tau} = \frac{1}{2\pi \cdot 0.15s}, \\ f_C &= 1.06Hz. \end{aligned}$$

The resulting integrator satisfies the previously defined target of  $0.5s - 1s$  to drive the full supply range with a slew rate of  $6.67V/s$  and hence  $0.75s$  for a change of  $5V$ .

Figure 2.28 shows the magnitude plot of the integrator. As can be seen, the gain crossover frequency  $f_C$  is approximately at  $1Hz$ .



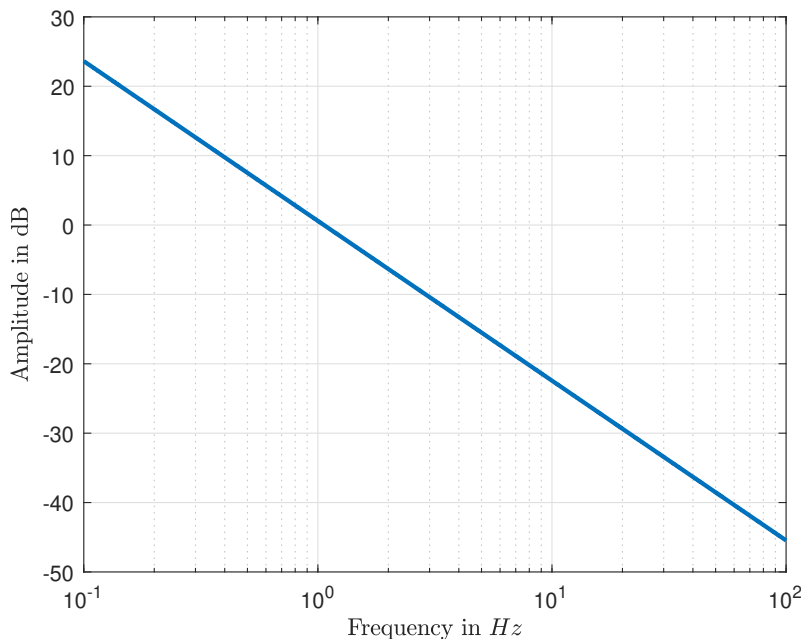


Figure 2.28: Magnitude plot of the designed integrator with a gain crossover frequency  $f_C = 1.06Hz$ .

As for the series resonance circuit there is an input and state transformation. However, for the integrator circuit this can not only be handled within the MATLAB Simulink environment, but also needs to be considered within the hardware design.

The signal driver channels of the connector board are only able to output a positive voltage (0V - 5V). Since the positive input of the operational amplifier is connected to ground, any positive input signal at the integrator leads to a negative output. However, as the operational amplifier is only supplied with positive voltage, it is not able to drive a negative output voltage. Hence, the output will always remain 0V.

To avoid this problem, the positive input is set to half of the supply voltage (2.5V) by using a simple voltage divider ( $R_{Div} = 150k\Omega$ ). Therefore, any input signal above 2.5V will lead to a decreasing integrator value and vice versa any signal below will lead to an increasing integrator output. Nevertheless, this leads to the next section, where input and state shift must also be considered in Simulink.

### 2.4.2.3 Simulink Integration

As for the series resonance circuit (Section 2.4.1.4), a MATLAB Simulink integration block was also implemented for the integrator. The abstracted *integrator circuit integration block* (ICI-block) is shown in Figure 2.29.

Both inputs are fed from the Simulink simulation, however,  $\Delta(t)$  is considered as unknown disturbance. The simulated perturbation  $\Delta(t)$  can be any given function,

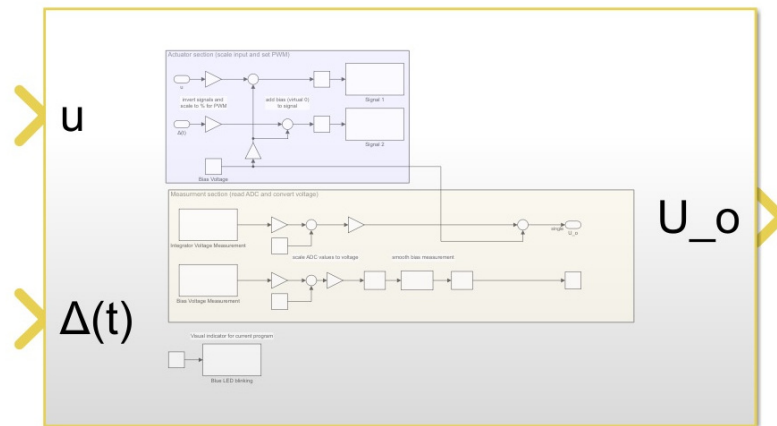


Figure 2.29: Abstracted MATLAB Simulink integration block of the integrator circuit. As the state-space model, the block has two inputs and one output. The second input  $\Delta(t)$  is considered as unknown perturbation.

as long as it stays within the input margins.

Figure 2.30 shows the inner structure of the ICI-block. Highlighted in red are the blocks of the *TI C2000 Piccolo Support from Embedded Coder hardware support package*. As for the SRCI-block, the structure of the integration block can be divided into an actuation section (light blue) and a measurement section (yellow).

Starting with the actuation section, the signal flow of both inputs is identical. First the input signal is inverted and scaled as percentage of the  $5V$  actuation range. The inversion is performed to mimic a "normal" integrator behaviour, although using an inverting integrator circuit. Then the previously mentioned input shift is performed in the same way as for the series resonance circuit

$$V_{in,virtual} = V_{in} - 2.5V.$$

The shift requires adding 50% in the integration block to obtain the real input value. Finally, the signal is passed through a saturation function where restrictions can be modelled. Eventually the Simulink based signal path ends at the ePWM block that outputs the corresponding PWM signal at the evaluation board. The PWM signal is then routed via the connector board, which does digital-analogue conversion and amplification, to the integrator test circuit. The settings for the ePWM block are  $200kHz$  frequency with up-counting mode and a pin chosen according pinout of the  $\mu C$ .

As also seen from Figure 2.30, the yellow measuring section takes two signals. The lower path is only to monitor and determine the voltage of the voltage divider. However, as this voltage defines the zero-point of the integrator circuit, any given deviation will lead to an error due to the input and state transformation. Neverthe-

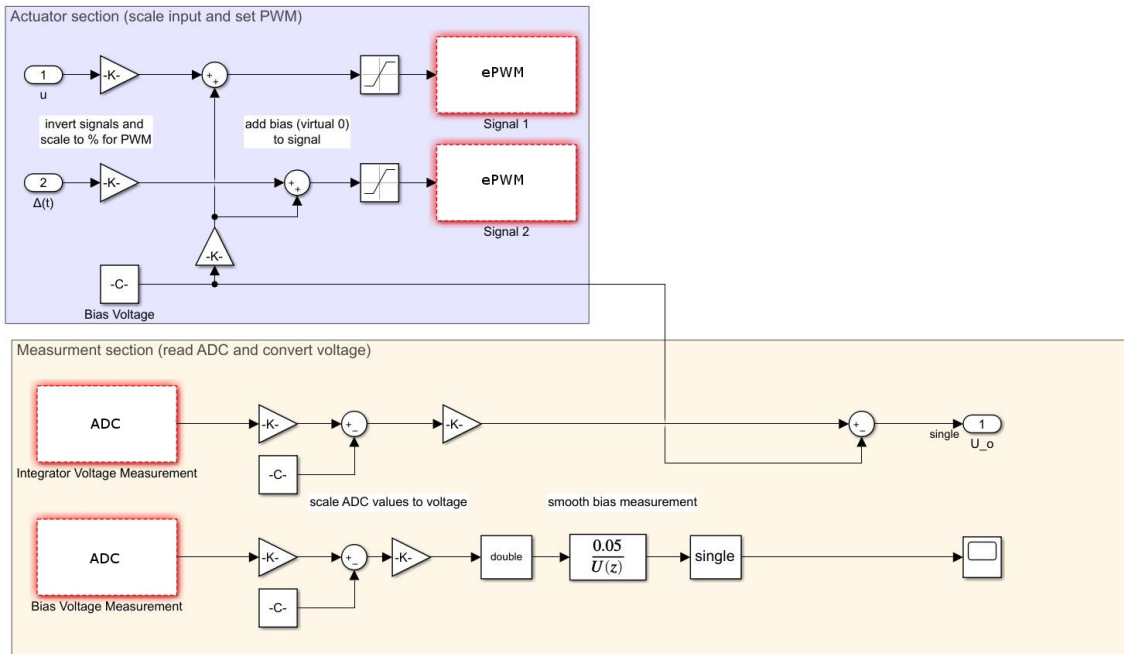


Figure 2.30: Block diagram of the MATLAB Simulink model for the integrator circuit integration. The structure of the test circuit integration block is divided into two sections, the upper actuator section in light blue and the lower measurement section in yellow. The ADC and ePWM blocks of the *TI C2000 Piccolo Support from Embedded Coder hardware support package* are highlighted in red.

less, the given voltage is not set as an output of the ICI-block, but can be checked in the block.

The second measured signal is the test circuits integrator output. The signal is scaled and anti-aliasing filtered via the connector board and then forwarded to an ADC on the evaluation board. The ADC block, is configured to  $1kHz$  sample rate in continuous mode with internal reference voltage, with the pin chosen according the pinout of the  $\mu C$ . The converted 12-bit integer value is transformed to a quantised voltage level and then translated to the real measured value using the parameters of the employed measurement amplifier channel given in Table 2.3. The last step is the state transformation as follows

$$x_{virtual} = x - 2.5V.$$

Again to clarify and as for the SRCI-block: Outside the block only the virtual input and state values appear. The actual values are only handled inside the ICI-block.

#### 2.4.2.4 Simulation and Final Integrator Circuit

Figure 2.31 shows the soldered integrator circuit. Starting left is the first wiring connection to the connector board, which includes supply, ground and the two input

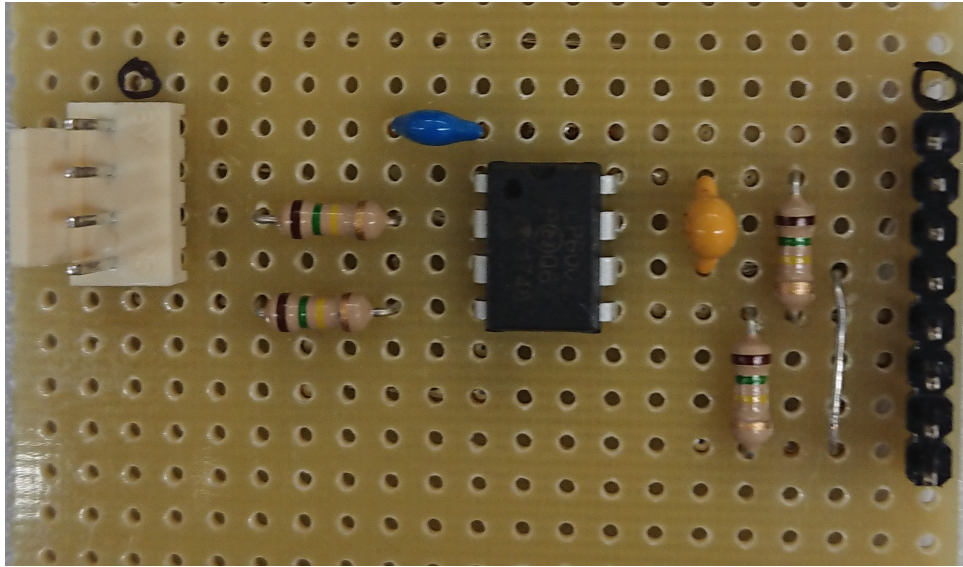


Figure 2.31: Implementation of the designed integrator circuit. Furthest left and right are the wiring interfaces. From left the two input signals are driven via the two resistors to the operational amplifier. On top in blue is the feedback capacitor. Right of the amplifier are a capacitor (yellow) to smooth supply drops and a voltage divider to set the positive input of the operational amplifier to half of the supply.

signals. Next are the two resistors at the integrator inputs, with the capacitor (blue) on top. Right of the operational amplifier are the capacitor (yellow) that smooths the amplifiers supply and the voltage divider that is used to set the positive input of the integrator to a half of the supply voltage. The second wiring connection takes the differential measurements, with the integrator output set to the first channel and the voltage of the voltage divider to the third channel.

As operational amplifier the *Microchip MCP6002*<sup>11</sup> is used again, with the second channel wired as unity gain buffer and the input set to half of the supply voltage. The detailed circuit diagram can be found in the appendix.

Figure 2.32 shows the integrator behaviour with different input signals. With an input of  $1.06\text{Hz}$ , corresponding to the gain crossover frequency, the signal is neither amplified, nor suppressed (figure 2.32a) whereas a  $10\text{Hz}$  input as seen in Figure 2.32b is strongly suppressed. As higher frequencies are suppressed even further, too high frequencies should not be used as input for this circuit since the relative measurement error is higher for smaller signals. Furthermore, as the  $5\text{V}$  supply is virtually split half around  $0\text{V}$ , the integrator circuit saturates at  $\pm 2.5\text{V}$ .

Finally Figure 2.33 shows the model verification of the integrator test circuit. Therefore, the integrator test circuit and a state space model of the integrator are run simultaneously in Simulink as open-loop with sine input of  $1.06\text{Hz}$  and  $1\text{V}$  amplitude. The measured output of the test circuit shows an offset which "slowly" drifts

<sup>11</sup><http://ww1.microchip.com/downloads/en/DeviceDoc/21733j.pdf>

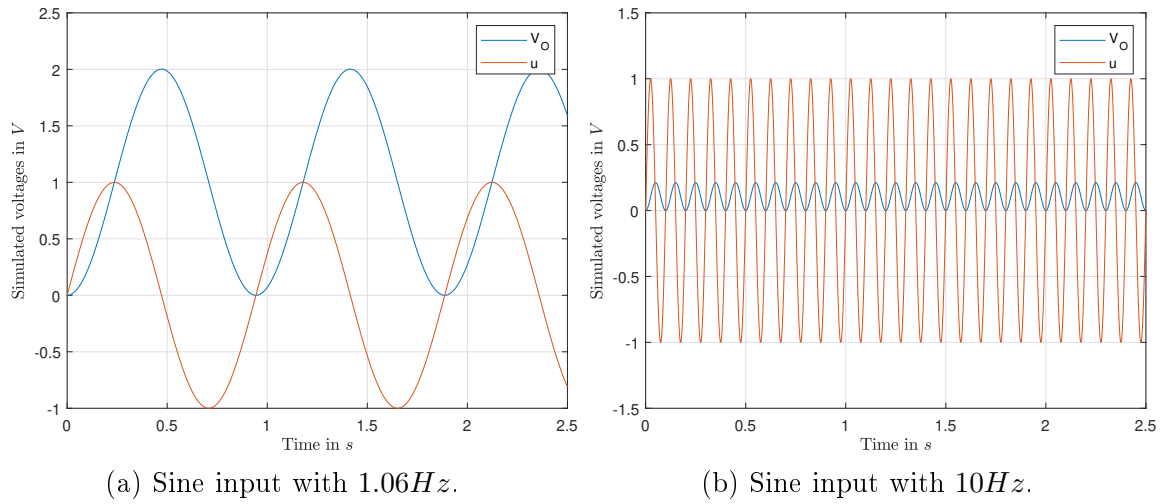


Figure 2.32: Simulation of designed the integrator with different input signals.

since the real integrator has a slight offset from zero.

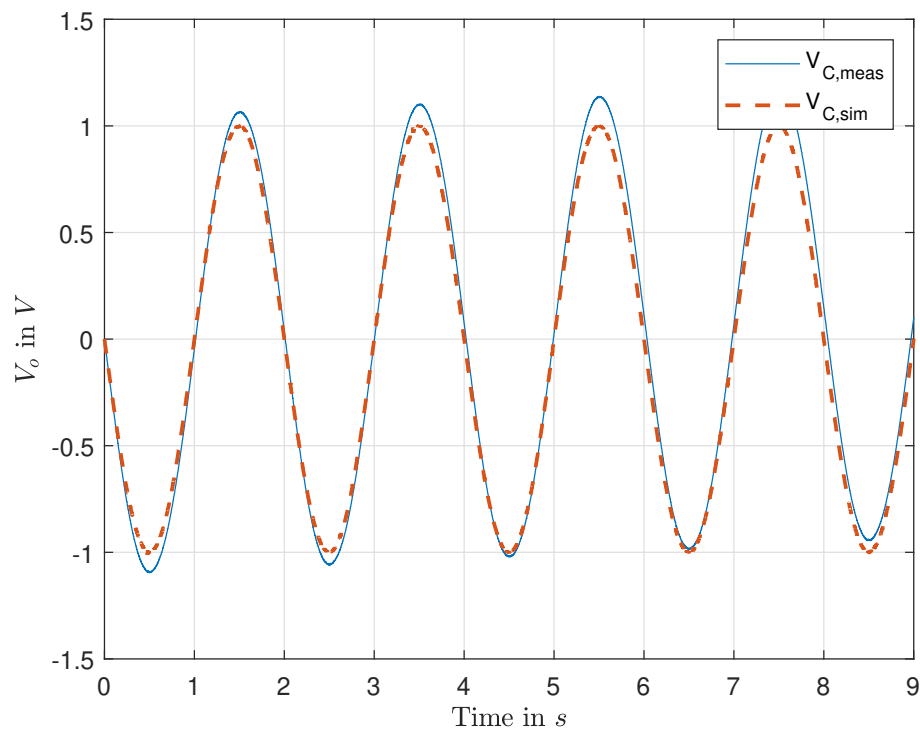


Figure 2.33: Comparison of the simulated model (orange) and the measured test circuit values (blue) for a sine input with  $1.06Hz$  and  $1V$ .

# 3 Controller and Observer Designs

In this chapter, various different controllers and observers are presented. The design process for each controller respectively observer is explained step-by-step. Furthermore, this chapter links to the corresponding literature providing more information.

The next section discusses several different controllers that are later designed for the test circuits. Subsequently, three different observer concepts will be presented. Finally, this chapter shows how controllers and observers can be combined.

## 3.1 Controller Designs

The selected controllers that are presented within this work have different design requirements. Some controllers need a linearised model of the plant (e.g. state controller). Therefore, an exact modelling of the plant is required which can be challenging especially for complex systems or systems with uncertainties. By contrast, other controllers only rely on the frequency response of the plant ("LS" controller) or simply have to be adjusted following certain rules (PID controller).

Within this section, the following controller concepts will be presented:

- PID control (*proportional-integral-derivative*),
- *loop-shaping* (LS), where the open-loop characteristics of the system are altered
- state feedback,
  - using eigenvalue assignment,
  - using linear quadratic regulators,
- PI-state control,
- first-order sliding mode control,
- second-order sliding mode control with the super-twisting algorithm and finally
- feedforward control.

### 3.1.1 Controllability

The first thing before starting with controller designs is to check whether the given system is *controllable* at all. The common definition for controllability is

A system is completely controllable if there exists an unconstrained control  $u(t)$  that can transfer any initial state  $\mathbf{x}(t_0)$  to any other desired location  $\mathbf{x}(t)$  in a finite time,  $t_0 \leq t \leq T$ . [1]

and similarly in [2–6].

To proof the controllability various different methods exist. In this work, the *Kalman's controllability criteria* [7], utilising the so-called controllability matrix

$$\mathbf{C}_u = [\mathbf{b}, \mathbf{A}\mathbf{b}, \mathbf{A}^2\mathbf{b}, \dots, \mathbf{A}^{n-1}\mathbf{b}].$$

is used. A LTI system is considered fully controllable if the controllability matrix  $\mathbf{C}_u$  has full rank

$$\text{rank}(\mathbf{C}_u) = n \tag{3.1}$$

[1–6]. Therefore, if condition (3.1) is satisfied, the pair  $(\mathbf{A}, \mathbf{b})$  is controllable and a controller design for the system is feasible.

### 3.1.2 PID Controller

The first discussed control method is the proportional-integral-derivative (PID) controller. The PID control approach is by far the most used feedback control approach applied to "simple devices" as well as large factories. As written in [8], PID controllers are used in over 97% of controllers within refining, chemicals and pulp and paper industries. Furthermore, the functionality of PID controllers can be extended by approaches like *automatic tuning*, *gain scheduling* and *anti-windup* [4] or the PID approach can be coupled with other control algorithms the obtain mixed control architectures like PI-state controllers (Section 3.1.5).

Obvious reasons for the use of PID controllers are their structure and the small amount of plant knowledge required.

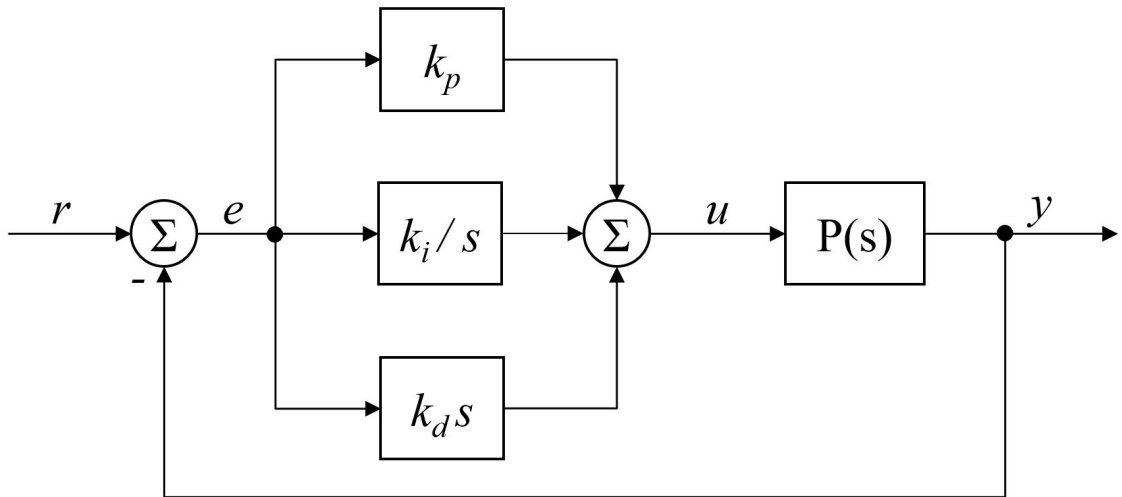


Figure 3.1: Block diagram of a closed-loop system with PID controller.

The control law of a standard PID controller is given as

$$u(t) = k_p e(t) + k_i \int_0^t e(\tau) d\tau + k_d \frac{de(t)}{dt} \quad (3.2)$$

or

$$u(t) = k_p \left( e(t) + \frac{1}{T_i} \int_0^t e(\tau) d\tau + T_d \frac{de(t)}{dt} \right),$$

with

$$T_i = \frac{k_p}{k_i} \quad \text{and} \quad T_d = \frac{k_d}{k_p}.$$

The control error is defined as  $e = r - y$ , where  $r$  is the reference signal and  $y$  the plant output. As can be seen in equation (3.2), the control law is a sum of three terms, a proportional error feedback, the integrated error and error derivative. The parameters of the controller are the gain of each term,  $k_p$ ,  $k_i$  and  $k_d$ . Figure 3.1 shows the block diagram of a closed-loop system with PID controller.

The structure of the controller can easily be changed by setting the parameters of the different parts to 0 obtaining e.g. a P, PD or PI controller. The different control actions of the single controller parts are highlighted by applying an unit step as reference input seen in Figure 3.2.

The proportional action depicted in Figure 3.2a, always counteracts the control error. By increasing the gain, the remaining stationary error decreases, however, the system tends to oscillate more.

Figure 3.2b shows the results when also considering the integral part. As can be seen, the integrator guarantees that any steady state error vanishes for step inputs. Higher gains ensure "faster" actions, but again lead to a more oscillating system. Nevertheless, if the plant is of integrating behaviour, no integral part is needed in



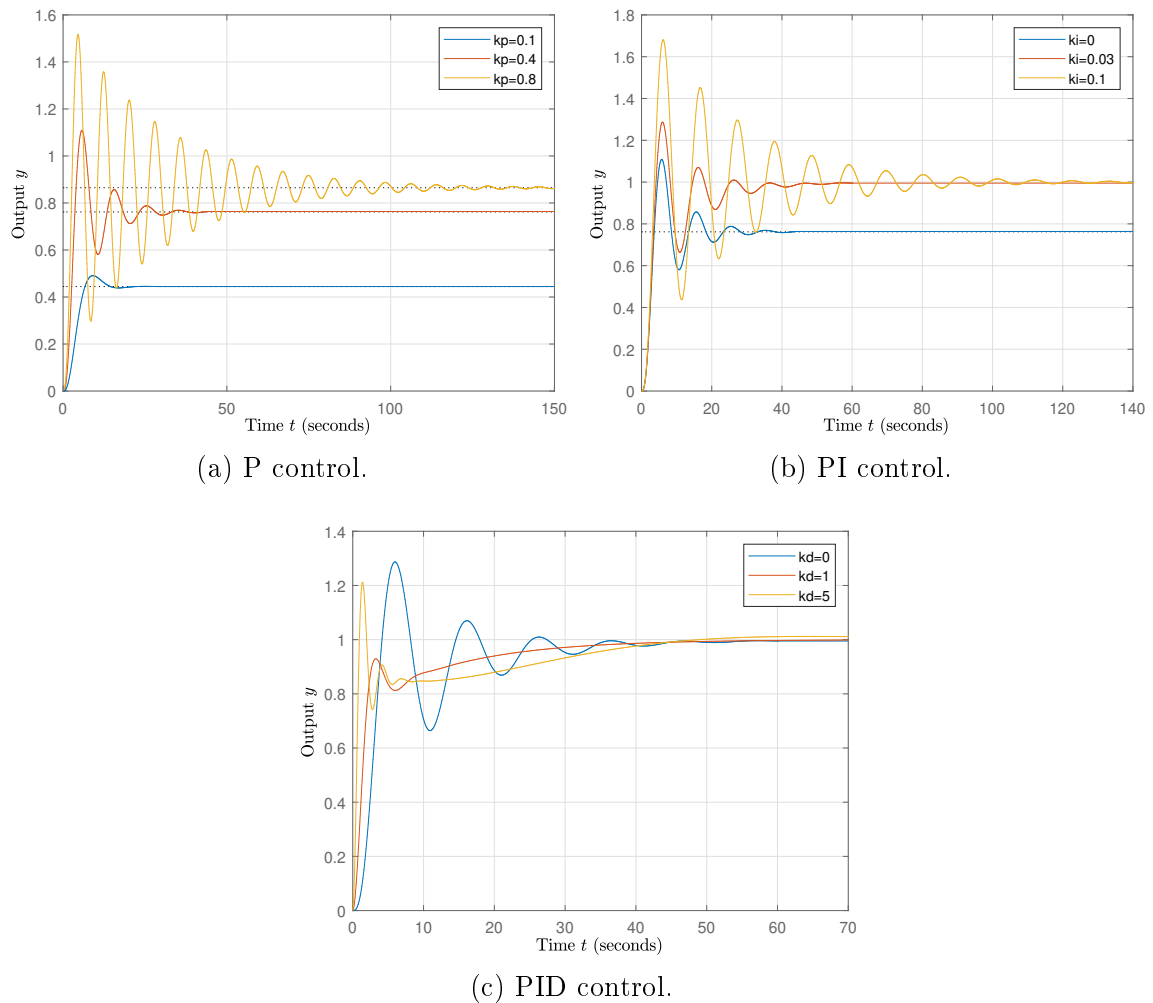


Figure 3.2: Closed-loop response with an unit step as reference input for a P controlled (a), a PI controlled (b) and a PID controlled (c) system. The transfer function of the plant is given as  $P(s) = 1/(s + 0.5)^3$ . The proportional parameter for the PI controller is  $k_p = 0.4$ . For the PID the parameters  $k_p = 0.4$  and  $k_i = 0.03$  are fixed.

the controller as any steady state error will vanish due to the plant behaviour.

Finally, the impact of the derivative control action can be seen in Figure 3.2c. Higher derivative gains damp the oscillating system behaviour. The derivative part is especially good for step changes of the reference signal, since the resulting fast change of the control error triggers a strong control action impulse.

The effects of increased controller gains using a step reference signal as in [1] are summarised in Table 3.1.

There are many heuristic approaches to get an initial setting for the PID parameters like the *Ziegler-Nichols step response method* where the experimentally obtained plant response to unit-step is used [1, 2, 4, 9, 10] or the *T-sum method* [11]. However, both methods require a 'S'-shaped step response which does not apply since the

gain	overshooting / oscillation	settling time	steady-state error
$k_p$	increases	minimal effect	decreases
$k_i$	increases	increases	no steady-state error
$k_d$	decreases	decreases	no impact

Table 3.1: Increased PID gains effect.

circuit is designed to overshoot.

Various other parameter tuning methods as well as "little modifications" to the PID structure exist [2, 4]. However, this work concentrates on the traditional PID control structure as in (3.2), with the parameter obtained using *Ziegler Nichols ultimate gain method* [1, 2, 4, 9, 10].

### 3.1.2.1 Ziegler-Nichols Ultimate Gain Method

*Ziegler Nichols ultimate gain method* (or *closed-loop method*) is a well-known tuning method for PID controller gains and exists since the early 1940s [12]. For this method it is necessary that experiments can be performed with the given circuit, or the transfer function of the circuit is known and the experiments can be done using simulation.

The method considers the closed-loop system response to a step input, while only using proportional feedback. Figure 3.3 shows the block diagram of the experiment.

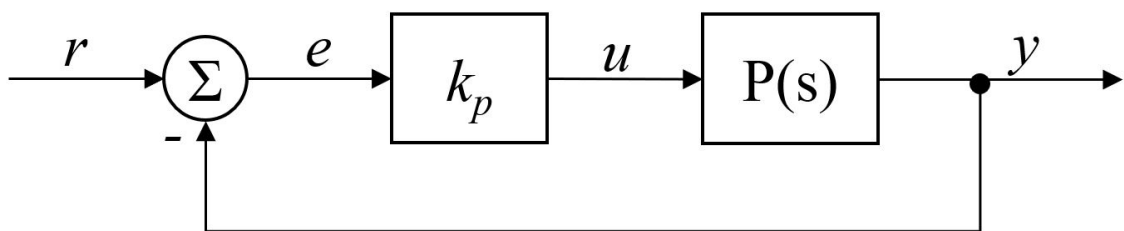


Figure 3.3: Block diagram of a closed-loop system with proportional controller to obtain the systems ultimate gain  $k_u$  and ultimate period  $T_u$  of the resulting oscillation.

To identify the system parameters for this method, the gain of the proportional feedback is increased until the closed-loop exhibits a limit cycle. The final proportional gain is called *ultimate gain* (or *critical gain*)  $k_u$ , with the period of the sustained oscillation called *ultimate period* (or *critical period*)  $T_u$ .

Table 3.2 lists the suggested gain settings based on the obtained parameters  $k_u$  and

$T_u$ . However, the resulting gain parameters of the PID controller should not be considered as fixed, but more as a starting point for further manual tuning.

controller type	$k_p$	$k_i$	$k_d$
P	$0.5k_u$	-	-
PI	$0.45k_u$	$\frac{0.54k_u}{T_u}$	-
PID	$0.6k_u$	$\frac{1.2k_u}{T_u}$	$\frac{0.6k_u T_u}{8}$

Table 3.2: Ziegler-Nichols suggested gain setting using the ultimate gain (closed-loop) method.

### 3.1.3 Loop-Shaping Design

As second method, a frequency-response design approach as in [1–4, 10, 13] is presented for the controller design. Therefore, the open-loop characteristics of the plant are analysed and shaped using bode plots. Hence this method is often referred as *loop-shaping* (LS).

As previously for the PID controller, also the LS controller relies solely on the control error  $e$ . For the design of the controller, the frequency-response of the plant must be known. This can either be done by experiments to determine the magnitude and phase characteristics of the plant or by having a linear mathematical model describing the plant dynamics.

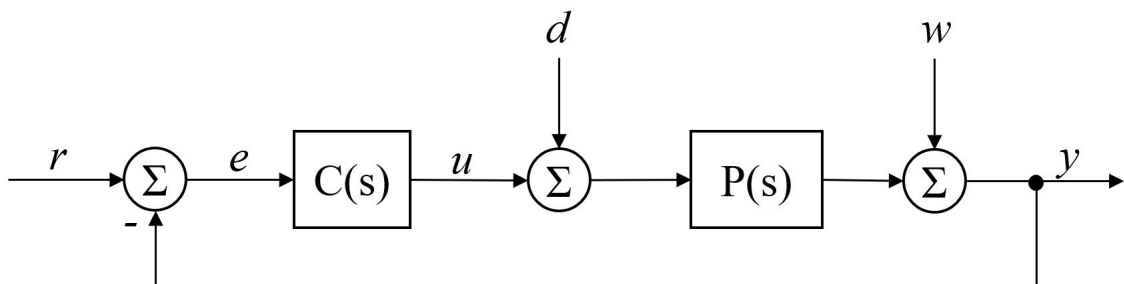


Figure 3.4: Block diagram of a standard control system with input disturbance and measurement noise.

Figure 3.4 shows the block diagram of an unity feedback loop control system. The modelled structure also includes input disturbance  $d$  and measurement noise  $w$  that occur in real-world systems.

### 3.1.3.1 Design considerations

The open-loop frequency response  $C(j\omega)P(j\omega)$  can roughly be divided into three sections as shown in Figure 3.5. A low-frequency region well below the crossover frequency, the section around the crossover frequency and finally the high-frequency region well above the crossover frequency.

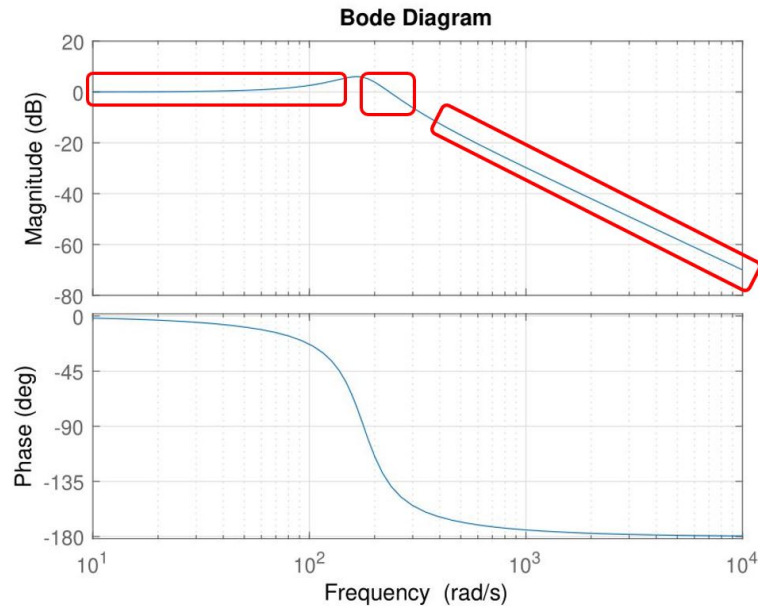


Figure 3.5: Bode plot of the given series resonance circuit. The magnitude plot is roughly divided into three sections, one section well below the crossover frequency (left), one region around the crossover frequency (middle) and one section well above (right). The design rules for the loop-shaping are based on requirements for these sections to obtain the desired behaviour.

There are five design points to be considered

1. the open-loop should have a high gain for the low-frequency section,
2. the slope around the unity gain crossover should be  $-20dB/decade$ ,
3. a good open-loop attenuation for the high-frequency section,
4. a desired cutoff frequency  $\omega_c$  and
5. a desired phase margin  $\phi_m$ .

Design specification 1. follows from the *complementary sensitivity function*  $T(s)$  (from  $r \rightarrow y$  and  $e \rightarrow y$ ) and the *input sensitivity function*  $S_d(s)$  (from  $u \rightarrow y$  and  $d \rightarrow y$ ). From Figure 3.4 it can be seen, that the open-loop is given as

$$L(s) = C(s)P(s).$$

the input sensitivity function given as

$$S_d(s) = \frac{P(s)}{1 + L(s)},$$

and the complementary sensitivity function given as

$$T(s) = \frac{L(s)}{1 + L(s)}.$$

Input disturbances  $d$  are typically low frequency signals. Considering the sensitivity function, a high open-loop gain for low frequencies assures that the input disturbances are attenuated ( $|L(s)| \gg 1 \rightarrow |S_d(s)| \ll 1$ ). Furthermore, when considering the complementary sensitivity function, the high gain dominates the denominator, hence guaranteeing good reference tracking ( $|L(s)| \gg 1 \rightarrow |T(s)| \approx 1$ ).

Design point 2 coheres with the stability respectively the robustness of the system as a slope of  $-20dB/decade$  guarantees a certain robustness of the system, coupled to the systems *sensitivity function*

$$S(s) = \frac{1}{1 + L(s)}.$$

Design specification 3 tries to minimise the effect of measurement noise. The two remaining design points are closely related to the response of the closed-loop system to an input step.

The bandwidth of the open-loop coheres with the "speed" of the system. A higher bandwidth and thus a higher cutoff frequency  $\omega_c$  of the open-loop leads to a faster rise time  $t_r$  of the closed-loop step response. The overshoot percentage of the closed-loop unit step response is given as

$$o_p = (M_p - 1)100\%,$$

where  $M_p$  is the maximum response peak. The overshooting of the closed-loop step response is associated with the phase margin  $\phi_m$  of the open-loop. A smaller phase margin implies an increased overshoot since the system is "closer to the instability".

From the correlations above two rules of thumb are defined in [10] leading to the last two design points

$$\begin{aligned} \omega_c t_r &\approx 1.5, \\ \phi_m + o_p &\approx 70. \end{aligned}$$

The rise time within [10] is defined as

$$t_r = \frac{1}{\dot{y}(t_{0.5})} \quad \text{where} \quad y(t_{0.5}) = 0.5.$$

Although given well defined specifications for the controller design, loop-shaping is a trial and error process where the designed controller may not fully satisfy the desired closed-loop behaviour.

### 3.1.3.2 Design Approach and Compensators

To modify the open-loop characteristics mainly three different types of compensators are used in the controller

- a. proportional compensators,
- b. integral compensators and
- c. lead/lag compensators.

Since the bode plot is a double-logarithmic plot, the multiplicative addition of compensators to the open-loop  $L(s) = C(s)P(s)$  leads to an addition of single frequency characteristics.

The proportional compensator

$$C(s) = K, \quad K > 0,$$

shifts the magnitude of the open-loop by  $|K|_{db}$ . If  $K > 1$  the magnitude is lifted, for  $K < 1$  the magnitude is lowered. There is no phase shift for the proportional compensator.

The integral compensator is given as

$$C(s) = \frac{1}{s^m}, \quad m \geq 1.$$

The phase is therefore reduced by  $m \cdot 90^\circ$  and the magnitude has a gain crossover frequency at  $\omega = 1 \text{ rad/s}$  and slope of  $m \cdot (-20 \text{ dB/decade})$ .

To shift the phase but keeping the impact on the magnitude small so-called lead/lag compensators are used. A lead compensator increases the phase within a certain area whereas a lag compensator reduces the phase.

The form of such compensators is given as

$$\frac{1 + \frac{s}{\omega_n}}{1 + \frac{s}{\omega_d}},$$

with  $\omega_n < \omega_d$  for the lead compensator and  $\omega_d < \omega_n$  for the lag compensator. The maximum phase shift can be at the middle frequency

$$\omega_m = \sqrt{\omega_n \omega_d}.$$

By setting

$$m = \frac{\omega_d}{\omega_n},$$

this further leads to

$$m = \frac{1 + \sin(\Delta\phi)}{1 - \sin(\Delta\phi)}$$

and

$$\omega_n = \frac{\omega_m}{\sqrt{m}}, \quad \omega_d = \omega_m \sqrt{m},$$

where  $\Delta\phi$  denotes the required phase shift.

The actual design processes can be described with an algorithm

- I. analyse frequency characteristics of the open-loop  $L(s)$
- II. modify the open-loop by adding a compensator  $L'(s) = L(s)C_i(s)$
- III. analyse the changed frequency characteristics  $L(s) = L'(s)$ 
  - if design specification fulfilled continue, else go to II
- IV. simulate closed-loop circuit  $T(s)$ 
  - if the resulting output response satisfies the specifications the design process is finished, else go to I.

The final controller

$$C(s) = \prod_{i=1}^p C_i(s),$$

is the product of the  $p$  compensators.

### 3.1.4 State Feedback

State controller alter the system dynamics by using state feedback [1–6, 9, 10, 14]. Therefore, a precise state-space model of the plant is needed.

The design of state controller is mainly driven by two objectives

1. the system output should match the reference signal for steady-state conditions

$$\lim_{t \rightarrow \infty} y(t) = \lim_{t \rightarrow \infty} r(t),$$

2. the system dynamics can be altered to satisfy certain specifications.

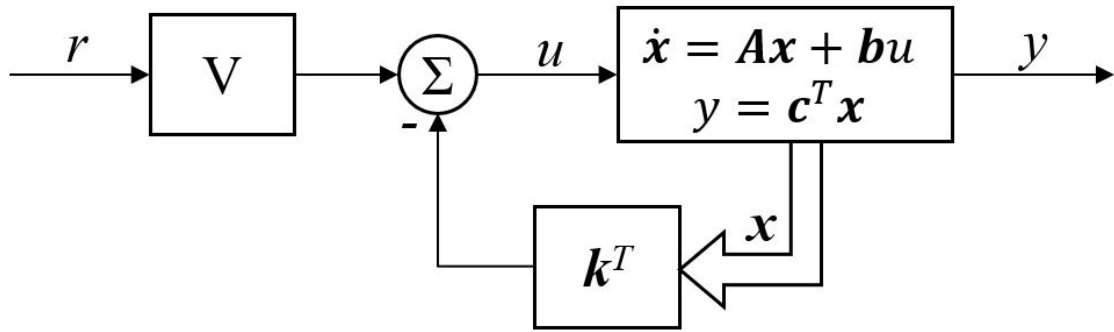


Figure 3.6: Block diagram of a closed-loop system with state controller. The input gain  $V$  ensures correct output scaling whereas the state feedback  $\mathbf{k}^T$  changes the system dynamics.

Figure 3.6 shows the structure of a closed-loop system using a linear state controller. The control law of a state controller is given by

$$u(t) = -\mathbf{k}^T \mathbf{x}(t) + Vr(t).$$

Hence, this leads to the closed-loop system dynamics

$$\frac{d}{dt} \mathbf{x} = (\mathbf{A} - \mathbf{b}\mathbf{k}^T) \mathbf{x} + \mathbf{b}Vr.$$

Two common ways to define the systems dynamics are *eigenvalue assignment* and the *linear quadratic regulator* (LQR) approach. Both approaches demonstrated and discussed subsequently.

### 3.1.4.1 Eigenvalue Assignment

With eigenvalue assignment, the state feedback is calculated so that the eigenvalues of the closed-loop dynamic matrix equal specified eigenvalues  $s_1, \dots, s_n$ . This is done using *Ackermann's formula* [15]. By placing the eigenvalues in the left open half space of the complex plane ( $\Re\{s_i\} < 0$ ), it can be ensured that the system is asymptotically stable.

At first a system in controllable canonical form is considered

$$\frac{d}{dt} \mathbf{x} = \begin{bmatrix} 0 & 1 & 0 & \dots & 0 \\ 0 & 0 & 1 & \dots & 0 \\ \vdots & \vdots & \vdots & \ddots & \vdots \\ 0 & 0 & 0 & \dots & 1 \\ -\alpha_0 & -\alpha_1 & -\alpha_2 & \dots & -\alpha_{n-1} \end{bmatrix} \mathbf{x} + \begin{bmatrix} 0 \\ 0 \\ \vdots \\ 0 \\ 1 \end{bmatrix} u,$$



with the associated characteristic equation given as

$$\Delta(s) = \det(s\mathbf{E} - \mathbf{A}) = s^n + (\alpha_{n-1})s^{n-1} + \cdots + \alpha_1s + \alpha_0 = 0.$$

By using state feedback

$$u = -\mathbf{k}_c^T \mathbf{x}, \quad \mathbf{k}_c^T = [k_{c,1} \quad k_{c,2} \quad \cdots \quad k_{c,n}],$$

the system dynamics are changed to

$$\frac{d}{dt} \mathbf{x} = \begin{bmatrix} 0 & 1 & 0 & \cdots & 0 \\ 0 & 0 & 1 & \cdots & 0 \\ \vdots & \vdots & \vdots & \ddots & \vdots \\ 0 & 0 & 0 & \cdots & 1 \\ (-\alpha_0 - k_{c,1}) & (-\alpha_1 - k_{c,2}) & (-\alpha_2 - k_{c,3}) & \cdots & (-\alpha_{n-1} - k_{c,n}) \end{bmatrix} \mathbf{x},$$

leading to a characteristic equation that can be altered to match the specified eigenvalues  $s_i$  and its corresponding characteristic equation  $w(s)$  as follows

$$\det(s\mathbf{E} - (\mathbf{A} - \mathbf{b}\mathbf{k}_c^T)) = s^n + (\alpha_{n-1} + k_{c,n})s^{n-1} + \cdots + (\alpha_1 + k_{c,2})s + (\alpha_0 + k_{c,1}),$$

$$\det(s\mathbf{E} - (\mathbf{A} - \mathbf{b}\mathbf{k}_c^T)) \stackrel{!}{=} \prod_{i=1}^n (s - s_i),$$

$$\det(s\mathbf{E} - (\mathbf{A} - \mathbf{b}\mathbf{k}_c^T)) \stackrel{!}{=} s^n + (w_{n-1})s^{n-1} + \cdots + w_1s + w_0 = w(s) = 0.$$

Hence, the controller parameters can easily be obtained by equating the coefficients. This resulting in

$$\mathbf{k}_c^T = [w_0 - \alpha_0 \quad w_1 - \alpha_1 \quad \cdots \quad w_{n-1} - \alpha_{n-1}]. \quad (3.3)$$

However, usually systems are not in controllable canonical form. Thus, a system transformation

$$\mathbf{z} = \mathbf{T}\mathbf{x}, \quad \mathbf{T} = \begin{bmatrix} \mathbf{t}_1^T \\ \mathbf{t}_1^T \mathbf{A} \\ \mathbf{t}_1^T \mathbf{A}^2 \\ \vdots \\ \mathbf{t}_1^T \mathbf{A}^{n-1} \end{bmatrix}$$

as explained in [2, 3, 5, 6, 9, 10] is used. Thereby  $\mathbf{t}_1^T$  is the last row of the inverse controllability matrix  $\mathbf{C}_u$ .

The transformed system reads as

$$\frac{d}{dt} \mathbf{z} = \mathbf{T}\mathbf{A}\mathbf{T}^{-1} \mathbf{z} - \mathbf{T}\mathbf{b}u,$$

where  $\mathbf{TAT}^{-1}$  is in companion form and  $\mathbf{Tb}$  is the  $n$ -th unity vector. The feedback for the canonical form  $\mathbf{k}_c^T$  can be calculated as in equation (3.3).

Using  $\mathbf{x} = \mathbf{T}^{-1}\mathbf{z}$  in order to transform back to the original states yields the controller equations

$$\mathbf{k}^T = \mathbf{k}_c^T \mathbf{T},$$

$$\mathbf{k}^T = [w_0 - \alpha_0 \quad w_1 - \alpha_1 \quad \dots \quad w_{n-1} - \alpha_{n-1}] \begin{bmatrix} \mathbf{t}_1^T \\ \mathbf{t}_1^T \mathbf{A} \\ \mathbf{t}_1^T \mathbf{A}^2 \\ \vdots \\ \mathbf{t}_1^T \mathbf{A}^{n-1} \end{bmatrix}.$$

By expanding, this reads as

$$\begin{aligned} \mathbf{k}^T &= \mathbf{t}_1^T (w_0 \mathbf{I} + w_1 \mathbf{A} + \dots + w_{n-1} \mathbf{A}^{n-1}) \\ &\quad - \mathbf{t}_1^T (\alpha_0 \mathbf{I} + \alpha_1 \mathbf{A} + \dots + \alpha_{n-1} \mathbf{A}^{n-1}). \end{aligned} \quad (3.4)$$

The Cayley-Hamilton theorem states that every quadratic matrix satisfies its own characteristic equation

$$\begin{aligned} \Delta(\mathbf{A}) &= \alpha_0 \mathbf{I} + \alpha_1 \mathbf{A} + \dots + \alpha_{n-1} \mathbf{A}^{n-1} + \mathbf{A}^n = 0, \\ \mathbf{A}^n &= -(\alpha_0 \mathbf{I} + \alpha_1 \mathbf{A} + \dots + \alpha_{n-1} \mathbf{A}^{n-1}), \end{aligned}$$

which exactly matches the bracket expression of the second term in equation (3.4). Therefore, leading to

$$\begin{aligned} \mathbf{k}^T &= \mathbf{t}_1^T (w_0 \mathbf{I} + w_1 \mathbf{A} + \dots + w_{n-1} \mathbf{A}^{n-1}) + \mathbf{t}_1^T \mathbf{A}^n, \\ \mathbf{k}^T &= \mathbf{t}_1^T (w_0 \mathbf{I} + w_1 \mathbf{A} + \dots + w_{n-1} \mathbf{A}^{n-1} + \mathbf{A}^n), \end{aligned}$$

and finally *Ackermann's formula*

$$\mathbf{k}^T = \mathbf{t}_1^T w(\mathbf{A}).$$

Hence, the controller parameters are calculated using  $\mathbf{t}_1^T$ , the last row of the inverse controllability matrix and  $w(\mathbf{A})$ , the desired characteristic equation with  $s$  substituted by  $\mathbf{A}$ . The calculation of the transformation matrix  $\mathbf{T}$  is actually never required.

The system has now the desired dynamics, however it does not track the input correctly. Hence, the reference variable is added to the control law

$$u(t) = -\mathbf{k}^T \mathbf{x}(t) + Vr(t).$$

To accomplish no steady-state error for constant input signals  $r$ , the reference signal must be scaled by the inverse of the system gain

$$\begin{aligned} V &= \frac{1}{T(s)} \Big|_{s=0}, \\ V &= \frac{1}{\mathbf{c}^T (s\mathbf{E} - (\mathbf{A} - \mathbf{b}\mathbf{k}^T))^{-1} \mathbf{b}} \Big|_{s=0}, \\ V &= -\frac{1}{\mathbf{c}^T (\mathbf{A} - \mathbf{b}\mathbf{k}^T)^{-1} \mathbf{b}}. \end{aligned} \tag{3.5}$$

For eigenvalue assignment it may be regarded as ideal if the eigenvalues are located far left in the complex plane to obtain a fast closed-loop system. However, this speed increase of the original system requires "big" control signals and is more sensitive to measurement noise and other imperfections. Thus, the next discussed approach leads to a more intuitive way by specifying weights for state variables and the control signal.

#### 3.1.4.2 LQR

The second common specification for the system dynamics with state feedback is done using the LQR with a quadratic cost function [1, 2, 4–6, 9].

Consider a dynamic system of the form

$$\frac{d}{dt} \mathbf{x} = \mathbf{A}\mathbf{x} + \mathbf{B}\mathbf{u}.$$

The cost function is often given as

$$J = \frac{1}{2} \int_0^\infty [\mathbf{x}^T \mathbf{Q} \mathbf{x} + \mathbf{u}^T \mathbf{R} \mathbf{u}] dt, \tag{3.6}$$

where  $\mathbf{Q} = \mathbf{Q}^T \succeq 0$  and  $\mathbf{R} = \mathbf{R}^T \succ 0$ .  $\mathbf{Q}$  and  $\mathbf{R}$  determine the "importance" of the system state (distance from the origin) relative to the expenditure of the control signal, therefore obtaining an optimal control in the sense of the given cost function. Thus, also referred as optimal control. Often  $\mathbf{Q}$  is chosen as diagonal matrix only defining the importance of the single state variables. Cross products of the state variables can be weighted using elements off the diagonal.

Using the control law

$$u(t) = -\mathbf{K}\mathbf{x}(t),$$

equation (3.6) changes to

$$J = \frac{1}{2} \int_0^{\infty} [\mathbf{x}^T \mathbf{Q} \mathbf{x} + (-\mathbf{x}^T \mathbf{K}^T) \mathbf{R} (-\mathbf{K} \mathbf{x})] dt,$$

$$J = \frac{1}{2} \int_0^{\infty} [\mathbf{x}^T (\mathbf{Q} + \mathbf{K}^T \mathbf{R} \mathbf{K}) \mathbf{x}] dt.$$

The optimal controller for the above cost function is given as

$$\mathbf{K} = \mathbf{R}^{-1} \mathbf{B}^T \mathbf{P} \mathbf{x}, \quad (3.7)$$

where  $\mathbf{P}$  is the unique positive-definite solution of the *algebraic-Riccati-equation* (ARE)

$$\mathbf{P} \mathbf{A} + \mathbf{A}^T \mathbf{P} - \mathbf{P} \mathbf{B} \mathbf{R}^{-1} \mathbf{B}^T \mathbf{P} + \mathbf{Q} = \mathbf{0}, \quad (3.8)$$

that can be solved using numerical methods. Due the use of the ARE, the controller is also referred as *riccati controller*. An exact derivation of the solution can be found in [2, 5, 6].

### 3.1.5 PI-State Controller

The PI-state controller is a combination of a state controller and a PI controller [1–3, 5, 10]. The resulting controller inherits the good control characteristics of the state controller but additionally obtains asymptotic tracking of the reference signal due to the integrating part even if constant disturbances exist.

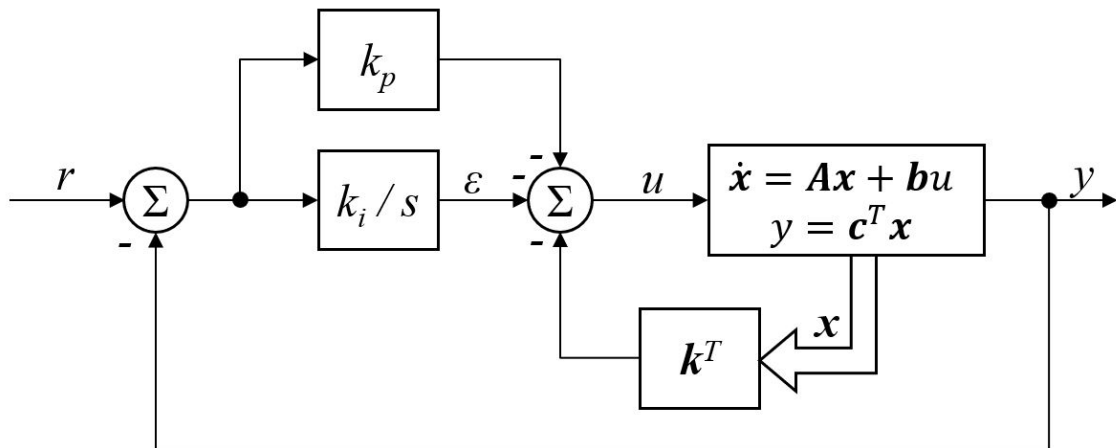


Figure 3.7: Block diagram of a closed-loop system with PI state controller.

Figure 3.7 shows the block diagram of the PI-state controller. The control law is

given as

$$\begin{aligned} u(t) &= -k_p e(t) - k_i \int_0^t e(\tau) dt - \mathbf{k}^T \mathbf{x}(t), \\ u(t) &= -k_p (r(t) - \mathbf{c}^T \mathbf{x}(t)) - k_i \epsilon - \mathbf{k}^T \mathbf{x}(t), \\ u(t) &= -k_p r(t) - k_i \epsilon - (\mathbf{k}^T - k_p \mathbf{c}^T) \mathbf{x}(t). \end{aligned}$$

Therefore, the system can be extended with the integrator state  $\epsilon$  leading to a closed-loop system of the form

$$\begin{aligned} \frac{d}{dt} \begin{bmatrix} \mathbf{x} \\ \epsilon \end{bmatrix} &= \begin{bmatrix} \mathbf{A} - \mathbf{b}(\mathbf{k}^T - k_p \mathbf{c}^T) & -\mathbf{b}k_i \\ -\mathbf{c}^T & 0 \end{bmatrix} \begin{bmatrix} \mathbf{x} \\ \epsilon \end{bmatrix} + \begin{bmatrix} -\mathbf{b}k_p \\ 1 \end{bmatrix} r, \\ \mathbf{y} &= \begin{bmatrix} \mathbf{c}^T & 0 \end{bmatrix} \begin{bmatrix} \mathbf{x} \\ \epsilon \end{bmatrix}. \end{aligned}$$

By defining

$$\tilde{\mathbf{A}} = \begin{bmatrix} \mathbf{A} & 0 \\ -\mathbf{c}^T & 0 \end{bmatrix}, \quad \tilde{\mathbf{b}} = \begin{bmatrix} \mathbf{b} \\ 0 \end{bmatrix} \quad \text{and} \quad \tilde{\mathbf{k}}^T = [\mathbf{k}^T - k_p \mathbf{c}^T \quad k_i], \quad (3.9)$$

the controller parameters can be obtained using the previously discussed methods *eigenvalue assignment* or *LQR*. However, it must be noted that due to the state extension the new system order is  $(n+1)$ . Furthermore, to allow arbitrary eigenvalues of the closed-loop  $(\tilde{\mathbf{A}} - \tilde{\mathbf{b}}\tilde{\mathbf{k}}^T)$ , the series of integrator and plant must be controllable. This requirement is satisfied if the controllable plant has no zeros at  $s = 0$  which is given by

$$\mathbf{c}^T (-\mathbf{A})^{-1} \mathbf{b} \neq 0. \quad (3.10)$$

As from equation (3.9) the integrator gain can be directly obtained from the parameter vector  $\tilde{\mathbf{k}}^T$ , i.e.

$$k_i = \tilde{k}_{n+1}.$$

This is not true for  $k_p$  and  $\mathbf{k}^T$  as those are related. Therefore,  $k_p$  is chosen allowing to calculate  $\mathbf{k}^T$  as

$$\mathbf{k}^T = [\tilde{k}_1 \quad \dots \quad \tilde{k}_n] + k_p \mathbf{c}^T.$$

A possible choice for  $k_p$  is

$$k_p = \frac{1}{\mathbf{c}^T \mathbf{A}^{-1} \mathbf{b}}. \quad (3.11)$$

Due to the previous assumption in equation (3.10)  $k_p$  always exists.

### 3.1.6 1-Sliding Controller

The sliding mode controllers discussed within this thesis are based on sliding mode approaches as presented in [16, 17]. Sliding mode approaches are robust controller design methods. Compared to other concepts, the main difference is the use of a discontinuous control signal with the control law relying on a switching function, a function of the current system state that may be regarded as an output of the system (sliding variable  $\sigma(\mathbf{x})$ ). Typically, a sliding mode controlled system may be characterised by two phases, a *reaching phase* ( $\sigma \neq 0$ ), in which the system reaches  $\sigma = 0$  in finite time. Whenever  $\sigma = 0$  is maintained, the system state is in the so-called *sliding mode* (or *sliding phase*) where the control law ensures that the trajectories "slide" along the sliding-manifold until the origin is reached. While sliding, there is a reduction of the system order since the sliding variable vanishes and the system dynamics are governed by parameters enforced through the control law only.

In theory, the system is able to maintain  $\sigma = 0$ . The solutions of such systems at  $\sigma = 0$  are understood in the sense of Filippov [18]. However, in terms of real systems, fast switching of the control signal is required to keep the sliding variable in a vicinity around zero. This is a major drawback for sliding mode control as actuator dynamics might cause problems or the actuator simply cannot execute the fast switches of the control signal.

For 1-sliding controller, the discontinuity is directly obtained in the first derivative of the sliding variable  $\sigma$ . The design of sliding mode controllers is pretty much straight forward using three steps. Assume a system of the form

$$\begin{aligned}\frac{d}{dt}x_1 &= f_1(x_1, x_2), \\ \frac{d}{dt}x_2 &= f_2(x_1, x_2) + B_2(x_1, x_2)u.\end{aligned}$$

At first  $x_2$  is considered as virtual control of  $x_1$ . Therefore

$$x_2 = -d(x_1)$$

is designed to produce a desired dynamic

$$\frac{d}{dt}x_1 = f_{1,d}(x_1).$$

The sliding manifold is then chosen as

$$\sigma = x_2 + d(x_1) = 0.$$

Hence, when the system reaches the sliding manifold,  $x_2 = -d(x_1)$  and  $x_1$  follows the previously designed dynamics

$$\frac{d}{dt}x_1 = f_1(x_1, -d(x_1)) = f_{1,d}(x_1).$$

The last step for the design process is the calculation of the control law. The control law has to ensure that the sliding manifold is reached. This is satisfied by choosing

$$\frac{d}{dt}\sigma \stackrel{!}{=} -k \operatorname{sgn}(\sigma),$$

where  $\operatorname{sgn}$  denotes the sign function.

### 3.1.7 Super-Twisting Controller

At the previously discussed 1-sliding controller, the discontinuous  $\operatorname{sgn}$  function produces a discontinuous control law. The *super-twisting* algorithm as discussed in [16, 17], tackles this problem to generate continuous control signals. The *super-twisting* algorithm reads as

$$\begin{aligned} v &= -k_1 \sqrt{|\sigma|} \operatorname{sgn}(\sigma) + w, \\ \frac{d}{dt}w &= -k_2 \operatorname{sgn}(\sigma), \end{aligned} \tag{3.12}$$

and

$$\frac{d}{dt}\sigma \stackrel{!}{=} v.$$

Due to the square root function the discontinuity is eliminated. However, the integrand of the state  $w$  is discontinuous. Hence, the discontinuity appears in the second derivative of the sliding variable and the super-twisting algorithm represents a second-order sliding mode algorithm. Furthermore,  $w$  also allows to estimate parameter uncertainties or disturbances.

### 3.1.8 Feedforward control

All the previously designed controllers are based on feedback in order to obtain the desired system behaviour. Another control design approach additionally uses feedforward control [4, 13, 19]. Feedforward control cannot replace feedback control but complements it. By using additional feedforward control, the tracking behaviour of the system can be improved without affecting the system's stability. Hence, the design of the two controllers can be done independently.

Figure 3.8 shows the structure of a two degrees of freedom design approach using feedforward and feedback control. The transfer function from the reference signal to the output ( $r_p \rightarrow y$ ) is given as

$$G_{ff+fb}(s) = \frac{C(s)P(s) + F(s)P(s)}{1 + C(s)P(s)}.$$

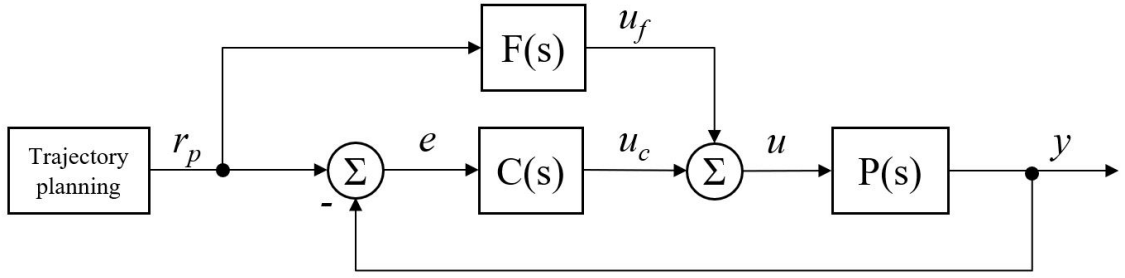


Figure 3.8: Block diagram of a closed-loop system with a two degrees of freedom control design. On one hand there is a conventional feedback control  $C(s)$  which compensates for tracking errors, on the other hand the feedforward control  $F(s)$  is used to "steer" the trajectories.

In [4, 13] it is proposed to choose the feedforward controller as inverse of the plant, i.e.

$$F(s) = P^{-1}(s).$$

Therefore, the system output exactly follows the reference input. However, the inverse of the plant must be stable, i.e. the numerator polynomial of the plant must be *Hurwitz* to ensure a bounded feedforward control signal  $u_f$ . Although this applies for some systems, a flatness based method as suggested in [19] is used in this thesis to present a more universal approach.

Figure 3.9a shows the slightly modified block diagram with the auxiliary variable  $z$ .

By choosing  $F(s) = \nu(s)$  and  $E(s) = \mu(s)$ , the auxiliary variable can be calculated as

$$\tilde{z} = \frac{1}{\nu(s)} \tilde{u}_f = \frac{1}{\mu(s)} \tilde{y}(s), \quad (3.13)$$

where

$$P(s) = \frac{\mu(s)}{\nu(s)} = \frac{\mu_0 + \mu_1 s + \mu_2 s^2 + \dots + \mu_m s^m}{\nu_0 + \nu_1 s + \nu_2 s^2 + \dots + \nu_n s^n}, \quad m < n$$

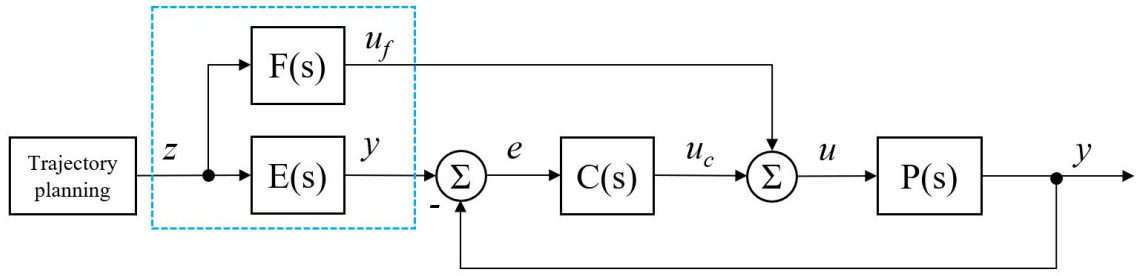
and  $\mu(s)$ ,  $\nu(s)$  are coprime.

Using equation (3.13), the time-domain relations are

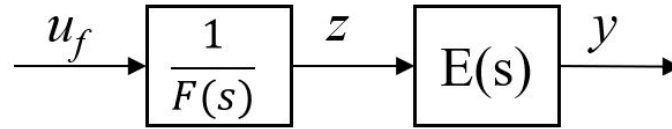
$$\begin{aligned} \nu_0 + \nu_1 \frac{d}{dt} z + \nu_2 \frac{d^2}{dt^2} z + \dots + \nu_n \frac{d^n}{dt^n} z &= u_f, \\ \mu_0 + \mu_1 \frac{d}{dt} z + \mu_2 \frac{d^2}{dt^2} z + \dots + \mu_m \frac{d^m}{dt^m} z &= y. \end{aligned} \quad (3.14)$$

Hence  $z$  must be at least  $n$  times differentiable which leads to the trajectory planning of  $z$ . Although the filters  $F(s) = \nu(s)$  and  $E(s) = \mu(s)$  are not proper, they must be seen in context with the planned trajectory  $z^*$  which is constructed to be sufficiently often differentiable.





(a) Modified block diagram of a closed-loop system with a two degrees of freedom control design. The auxiliary variable  $z$  is calculated to obtain the desired output  $y$ .



(b) Reshape of the blue section in (a) to interpret the auxiliary variable  $z$  as intermediate variable.

Figure 3.9: Closed-loop system with a flatness based two degrees of freedom control design (a). By reshaping, the auxiliary variable  $z$  can be considered as intermediate variable between the feedforward control signal  $u_f$  and the reference signal  $r = y$  to cause no feedback control action (b).

### 3.1.8.1 Trajectory planning

The task of trajectory planning is to obtain a desired trajectory  $z = z^*$  that transfers the system from a given state into another state.

For the change of the operation point, the trajectory  $z^*$  has to fulfil conditions concerning the start and end point of the transition according equation (3.14)

$$z^*(t = 0) = z_s^* = \frac{y_s}{\mu_0}, \quad z^*(t = T_t) = z_e^* = \frac{y_e}{\mu_0}, \quad (3.15)$$

where  $T_t$  is the transition time,  $y_s$  the system output at the start and  $y_e$  the system output at the end of the transition. Furthermore, it is required that the system has a sufficient flat trajectory at these points

$$\left. \frac{d^i}{dt^i} z^* \right|_{t=0} = \left. \frac{d^i}{dt^i} z^* \right|_{t=T_t} = 0 \quad \text{for } i = 1, \dots, n. \quad (3.16)$$

One possible solution is to use a polynomial of order  $p = 2n + 1$

$$z^*(t) = \gamma_0 + \gamma_1 t + \gamma_2 t^2 + \dots + \gamma_p t^p.$$

The polynomial allows to fulfil all previously defined requirements for start and end point respectively flatness. Furthermore,  $z^*$  is more than  $n$  times differentiable, hence, able to be processed by the filters  $F(s)$  and  $E(s)$ .

With equations (3.15) and (3.16) a general form for the desired trajectory can be derived as

$$z^*(t) = z_s^* + (z_e^* - z_s^*) \sum_{i=n+1}^{2n+1} \tilde{\gamma}_i \frac{t^i}{T^i}. \quad (3.17)$$

The coefficients  $\tilde{\gamma}_i$  up to system order  $n = 5$  are given in Table 3.3.

$n$	$\tilde{\gamma}_{n+1}$	$\tilde{\gamma}_{n+2}$	$\tilde{\gamma}_{n+3}$	$\tilde{\gamma}_{n+4}$	$\tilde{\gamma}_{n+5}$	$\tilde{\gamma}_{n+5}$
1	3	-2				
2	10	-15	6			
3	35	-84	70	-20		
4	126	-420	540	-315	70	
5	462	-1980	3465	-3080	1386	-252

Table 3.3: Auxiliary coefficients for the design of the planned trajectory. (Excerpt from *Regelungstechnik lecture notes version 5.10.2018*)

## 3.2 Observer Designs

The previous Section 3.1 about controller design showed that a lot of control laws rely on the system state. However, the state variables are not always available via measurement. Therefore, it is necessary to reconstruct the system states using so called state observers or state estimators. To emulate the state, the observer uses a copy of the plant and a correction term to reduce the observation error.

In this section three different observers are discussed

- a *Luenberger* observer,
- a reduced observer and
- a super-twisting observer.

### 3.2.1 Observability

As for the controllability (Section 3.1.1), there are also conditions to examine the *observability* of a system. The common definition of the observability is:

A system is completely observable if and only if there exists a finite time  $T$  such that the initial state  $x(0)$  can be determined from the observation history  $y(t)$  given the control  $u(t)$ ,  $0 \leq t \leq T$ . [1]

and similarly in [2–6].

Analogous to the proof of controllability, the proof of the observability is carried out using *Kalman's observability criteria*, this time, however, utilising the observability matrix

$$\mathbf{O}_y = \begin{bmatrix} \mathbf{c}^T \\ \mathbf{c}^T \mathbf{A} \\ \mathbf{c}^T \mathbf{A}^2 \\ \vdots \\ \mathbf{c}^T \mathbf{A}^{n-1} \end{bmatrix}.$$

The pair  $(\mathbf{A}, \mathbf{c}^T)$  is therefore considered fully observable if

$$\text{rank}(\mathbf{O}_y) = n.$$

### 3.2.2 Luenberger Observer

The *Luenberger* observer as in [1–6, 9, 10, 14] is kind of the standard approach for state estimation.

The Luenberger estimator is formulated as

$$\frac{d}{dt} \hat{\mathbf{x}} = \mathbf{A} \hat{\mathbf{x}} + \mathbf{b}u + \mathbf{l}(y - \hat{y}).$$

Hence, the resulting observer error  $\tilde{\mathbf{x}} = \mathbf{x} - \hat{\mathbf{x}}$  is given as

$$\begin{aligned} \frac{d}{dt} \tilde{\mathbf{x}} &= \mathbf{A} \mathbf{x} + \mathbf{b}u - \mathbf{A} \hat{\mathbf{x}} - \mathbf{b}u - \mathbf{l}(y - \hat{y}), \\ \frac{d}{dt} \tilde{\mathbf{x}} &= \mathbf{A} (\mathbf{x} - \hat{\mathbf{x}}) - \mathbf{l} \mathbf{c}^T (\mathbf{x} - \hat{\mathbf{x}}), \\ \frac{d}{dt} \tilde{\mathbf{x}} &= (\mathbf{A} - \mathbf{l} \mathbf{c}^T) \tilde{\mathbf{x}} \end{aligned}.$$

Therefore, the error dynamics  $(\mathbf{A} - \mathbf{l} \mathbf{c}^T)$  are chosen to be *Hurwitz*, ensuring that the estimation error vanishes asymptotically. The problem is similar to the design problem of the state controller where the vector  $\mathbf{k}^T$  is calculated for the dynamics  $(\mathbf{A} - \mathbf{b} \mathbf{k}^T)$ . The eigenvalues and the characteristic polynomial do not change when transposing a quadratic matrix. Hence, by transposing the given dynamics  $(\mathbf{A}^T - \mathbf{c} \mathbf{l}^T)$ , the calculation of the observer gains can be done using the methods from the state controller design in Section 3.1.4. Therefore, this is often considered as the dual design problem.

The poles should be chosen "far" left in the complex plane. Nevertheless, with too high gains the measurement noise has an impact the observation error. In the case of a noisy output

$$\begin{aligned} \mathbf{y} &= \mathbf{C}\mathbf{x} + \eta, \\ \frac{d}{dt}\tilde{\mathbf{x}} &= (\mathbf{A} - \mathbf{l}\mathbf{c}^T)\tilde{\mathbf{x}} - \mathbf{l}\eta, \end{aligned}$$

where  $\eta$  is the measurement noise. Therefore, a trade-off between a fast decay of the observation error and the influence due to measurement noise must be made.

### 3.2.3 Reduced Observer

The reduced observer, as explained in [2, 5, 6, 9, 14], follows the approach of the Luenberger observer, however  $q$  state variables are considered measurable. Therefore, the observer only has to estimate  $n - q$  state variables, thus having a reduced order of  $n - q$ .

To derive the reduced observer, consider a LTI system of the form

$$\begin{aligned} \frac{d}{dt} \begin{bmatrix} \mathbf{x}_m \\ \mathbf{x}_o \end{bmatrix} &= \begin{bmatrix} \mathbf{A}_{11} & \mathbf{A}_{12} \\ \mathbf{A}_{21} & \mathbf{A}_{22} \end{bmatrix} \begin{bmatrix} \mathbf{x}_m \\ \mathbf{x}_o \end{bmatrix} + \begin{bmatrix} \mathbf{B}_m \\ \mathbf{B}_o \end{bmatrix} \mathbf{u}, \\ \mathbf{y} &= \begin{bmatrix} \mathbf{I} & \mathbf{0} \end{bmatrix} \begin{bmatrix} \mathbf{x}_m \\ \mathbf{x}_o \end{bmatrix} = \mathbf{x}_m, \end{aligned} \tag{3.18}$$

where  $\mathbf{x}_m$  denotes the  $q$  measurable state variables and  $\mathbf{x}_o$  the  $n - q$  state variables to observe.

The dynamics of the observed state is given as

$$\frac{d}{dt} \underbrace{\mathbf{x}_o}_{\mathbf{z}} = \underbrace{\mathbf{A}_{22}\mathbf{x}_o}_{\mathbf{A}_z\mathbf{z}} + \underbrace{[\mathbf{A}_{21} \quad \mathbf{B}_o]}_{\mathbf{B}_z} \underbrace{\begin{bmatrix} \mathbf{x}_m \\ \mathbf{u} \end{bmatrix}}_{\mathbf{u}_z}$$

and the output relations using the measured state dynamics as

$$\underbrace{\frac{d}{dt}\mathbf{x}_m - \mathbf{A}_{11}\mathbf{x}_m - \mathbf{B}_m\mathbf{u}}_{\mathbf{y}_z} = \underbrace{\mathbf{A}_{12}}_{\mathbf{C}_z} \underbrace{\mathbf{x}_o}_{\mathbf{z}}.$$

Formulating the Luenberger observer for the virtual state  $\mathbf{z}$  reads

$$\frac{d}{dt}\hat{\mathbf{z}} = \mathbf{A}_z\hat{\mathbf{z}} + \mathbf{B}_z\mathbf{u}_z + \mathbf{L}(\mathbf{y}_z - \hat{\mathbf{y}}_z).$$

Substituting

$$\begin{aligned} \mathbf{x}_o &\rightarrow \mathbf{z}, \\ \mathbf{A}_{22} &\rightarrow \mathbf{A}_z, \\ [\mathbf{A}_{21} \ \mathbf{B}_o] &\rightarrow \mathbf{B}_z, \\ \begin{bmatrix} \mathbf{x}_m \\ \mathbf{u} \end{bmatrix} &\rightarrow \mathbf{u}_z, \\ \frac{d}{dt}\mathbf{x}_m - \mathbf{A}_{11}\mathbf{x}_m - \mathbf{B}_m\mathbf{u} &\rightarrow \mathbf{y}_z, \\ \mathbf{A}_{12} &\rightarrow \mathbf{C}_z, \end{aligned}$$

leads to

$$\begin{aligned} \frac{d}{dt}\hat{\mathbf{x}}_o &= \mathbf{A}_{22}\hat{\mathbf{x}}_o + [\mathbf{A}_{21} \ \mathbf{B}_o] \begin{bmatrix} \mathbf{x}_m \\ \mathbf{u} \end{bmatrix} + \mathbf{L} \left( \frac{d}{dt}\mathbf{x}_m - \mathbf{A}_{11}\mathbf{x}_m - \mathbf{B}_m\mathbf{u} - \mathbf{A}_{12}\hat{\mathbf{x}}_o \right), \\ \frac{d}{dt}\hat{\mathbf{x}}_o &= (\mathbf{A}_{22} - \mathbf{L}\mathbf{A}_{12})\hat{\mathbf{x}}_o + (\mathbf{B}_o - \mathbf{L}\mathbf{B}_m)\mathbf{u} + (\mathbf{A}_{21} - \mathbf{L}\mathbf{A}_{11})\mathbf{y} + \mathbf{L}\frac{d}{dt}\mathbf{y}, \end{aligned}$$

with the derivative of  $\mathbf{y}$  still "troublesome". Therefore, a new state

$$\bar{\mathbf{x}}_o = \hat{\mathbf{x}}_o - \mathbf{L}\mathbf{y}$$

is defined, with the final reduced observer given as

$$\begin{aligned} \frac{d}{dt}\bar{\mathbf{x}}_o &= (\mathbf{A}_{22} - \mathbf{L}\mathbf{A}_{12})\bar{\mathbf{x}}_o + (\mathbf{B}_o - \mathbf{L}\mathbf{B}_m)\mathbf{u} \\ &\quad + (\mathbf{A}_{21} - \mathbf{L}\mathbf{A}_{11} + \mathbf{A}_{22}\mathbf{L} - \mathbf{L}\mathbf{A}_{12}\mathbf{L})\mathbf{y}, \\ \hat{\mathbf{x}}_o &= \bar{\mathbf{x}}_o + \mathbf{L}\mathbf{y}. \end{aligned} \tag{3.19}$$

The matrix  $\mathbf{L}$  is then to be chosen that  $(\mathbf{A}_{22} - \mathbf{L}\mathbf{A}_{12})$  is Hurwitz and hence the estimation error  $\tilde{\mathbf{x}}_o = \mathbf{x}_o - \hat{\mathbf{x}}_o$  vanishes asymptotically.

### 3.2.4 Super-Twisting Observer

Sliding mode approaches can also be used for state estimation [16, 17]. The super-twisting algorithm, as subsequently discussed, can not only be used to estimate the states but also to estimate system parameters or uncertainties but also perturbations.

Therefore, a LTI system of the form

$$\begin{aligned} \frac{d}{dt} \underbrace{\begin{bmatrix} \mathbf{x}_1 \\ \mathbf{x}_2 \end{bmatrix}}_{\mathbf{x}} &= \underbrace{\begin{bmatrix} \mathbf{A}_{11} & \mathbf{A}_{12} \\ \mathbf{A}_{21} & \mathbf{A}_{22} \end{bmatrix}}_{\mathbf{A}} \mathbf{x} + \underbrace{\begin{bmatrix} \mathbf{B}_1 & \mathbf{B}_2 \end{bmatrix}}_{\mathbf{B}} \mathbf{u}, \\ \mathbf{y} &= \underbrace{\begin{bmatrix} \mathbf{0} & \mathbf{I} \end{bmatrix}}_{\mathbf{C}} \mathbf{x} = \mathbf{x}_2, \end{aligned}$$

is considered that has  $q$  measurable state variables  $\mathbf{x}_2$  as output.

The observer errors are defined as  $\tilde{\mathbf{x}}_1 = \mathbf{x}_1 - \hat{\mathbf{x}}_1$ , while the last  $q$  errors denoted as  $\tilde{\mathbf{x}}_2 = \mathbf{x}_2 - \hat{\mathbf{x}}_2$

The proposed observer in [17] is given as

$$\frac{d}{dt}\hat{\mathbf{x}} = \mathbf{A}\hat{\mathbf{x}} + \mathbf{B}\mathbf{u} - \mathbf{G}_n\mathbf{v}, \quad \mathbf{G}_n = \begin{bmatrix} \mathbf{L} \\ \mathbf{I} \end{bmatrix}, \quad \mathbf{v} = \begin{bmatrix} v_1 \\ \vdots \\ v_q \end{bmatrix},$$

where  $v_i$  are the inserted discontinuous injection terms. Here, the super-twisting algorithm is used as injection term and component wise given as

$$\begin{aligned} v_i &= -k_{1,i}\sqrt{|\tilde{x}_{2,i}|} \operatorname{sgn}(\tilde{x}_{2,i}) + w_i, \\ \frac{d}{dt}w_i &= -k_{2,i} \operatorname{sgn}(\tilde{x}_{2,i}), \end{aligned} \quad i = 1, \dots, q. \quad (3.20)$$

The error equations yield

$$\begin{aligned} \frac{d}{dt}\tilde{\mathbf{x}}_1 &= \mathbf{A}_{11}\tilde{\mathbf{x}}_1 + \mathbf{A}_{12}\tilde{\mathbf{x}}_2 + \mathbf{L}\mathbf{v}, \\ \frac{d}{dt}\tilde{\mathbf{x}}_2 &= \mathbf{A}_{21}\tilde{\mathbf{x}}_1 + \mathbf{A}_{22}\tilde{\mathbf{x}}_2 + \mathbf{v}, \end{aligned} \quad (3.21)$$

and for a single component of  $\tilde{\mathbf{x}}_2$  the error reads as

$$\frac{d}{dt}\tilde{x}_{2,i} = \mathbf{A}_{21,i}\tilde{\mathbf{x}}_1 + \mathbf{A}_{22,i}\tilde{\mathbf{x}}_2 - k_{1,i}\sqrt{|\tilde{x}_{2,i}|} \operatorname{sgn}(\tilde{x}_{2,i}) + w_i, \quad i = 1, \dots, q.$$

The associated dynamics of  $w_i$  are further not listed explicitly as they are already given in equation (3.20).

By choosing the parameters  $M_i$  and therefore the gains

$$k_{1,i} = 1.5\sqrt{M_i}, \quad k_{2,i} = 1.1M_i,$$

high enough that the error dynamics are always governed by the injection term, the errors  $\tilde{x}_{2,i}$  will vanish in finite time. After each observer error  $\tilde{x}_{2,i} = 0$ , the sliding mode is reached. Thus, the observer dynamics change and yield

$$\begin{aligned} \tilde{\mathbf{x}}_2 &= \frac{d}{dt}\tilde{\mathbf{x}}_2 = \mathbf{0}, \\ \mathbf{0} &= \mathbf{A}_{21}\tilde{\mathbf{x}}_1 + \mathbf{w}, \\ \mathbf{w} &= -\mathbf{A}_{21}\tilde{\mathbf{x}}_1, \end{aligned}$$

where

$$\mathbf{w} = \begin{bmatrix} w_1 \\ \vdots \\ w_p \end{bmatrix}, \quad i = 1, \dots, q.$$

Therefore, the error dynamics from equations (3.21) change to

$$\begin{aligned}\frac{d}{dt}\tilde{\mathbf{x}}_1 &= \mathbf{A}_{11}\tilde{\mathbf{x}}_1 - \mathbf{L}\mathbf{A}_{21}\tilde{\mathbf{x}}_1, \\ \frac{d}{dt}\tilde{\mathbf{x}}_2 &= (\mathbf{A}_{11} - \mathbf{L}\mathbf{A}_{21})\tilde{\mathbf{x}}_1.\end{aligned}\tag{3.22}$$

To obtain an asymptotically decay of the observer error  $\tilde{\mathbf{x}}_1$ , the matrix  $\mathbf{L}$  must be chosen that  $(\mathbf{A}_{11} - \mathbf{L}\mathbf{A}_{21})$  is Hurwitz.

### 3.3 Observer-Based control

In the previous two sections different controller and observer approaches were presented. This section shows how these concepts can be combined and what needs to be considered in doing so.

#### 3.3.1 Separation Theorem

The *separation theorem* (or separation principle) states that controller and observer can be designed individually although the observed state vector  $\hat{\mathbf{x}}$  is used for control [1, 4–6, 10, 14]. This can be easily shown by considering a standard LTI system of the form

$$\begin{aligned}\frac{d}{dt}\mathbf{x} &= \mathbf{A}\mathbf{x} + \mathbf{B}\mathbf{u}, \\ \mathbf{y} &= \mathbf{C}\mathbf{x}.\end{aligned}$$

Furthermore, there is a state feedback gain  $\mathbf{K}$  and an observer gain  $\mathbf{L}$  that  $(\mathbf{A} - \mathbf{B}\mathbf{K})$  and  $(\mathbf{A} - \mathbf{L}\mathbf{C})$  are Hurwitz.

With the control law

$$\mathbf{u} = -\mathbf{K}\hat{\mathbf{x}} + \mathbf{V}\mathbf{r} = -\mathbf{K}(\mathbf{x} - \tilde{\mathbf{x}}) + \mathbf{V}\mathbf{r},$$

the extended system dynamics read

$$\frac{d}{dt}\begin{bmatrix} \mathbf{x} \\ \tilde{\mathbf{x}} \end{bmatrix} = \begin{bmatrix} \mathbf{A} - \mathbf{B}\mathbf{K} & \mathbf{B}\mathbf{K} \\ \mathbf{0} & \mathbf{A} - \mathbf{L}\mathbf{C} \end{bmatrix} \begin{bmatrix} \mathbf{x} \\ \tilde{\mathbf{x}} \end{bmatrix} + \begin{bmatrix} \mathbf{B}\mathbf{V} \\ \mathbf{0} \end{bmatrix} \mathbf{r}$$

The resulting characteristic polynomial follows as

$$\Delta(s) = (s\mathbf{E} - (\mathbf{A} - \mathbf{B}\mathbf{K}))(s\mathbf{E} - (\mathbf{A} - \mathbf{L}\mathbf{C})) = 0.$$

Thus, the poles of the controller and observer do no impact each other and both can be designed independently. However, by using the estimated state in the control law the transient behaviour of the circuit is usually impaired.

[6] suggests to choose the observer poles  $s_{o,i}$  to have a 2 – 6 times higher magnitude than the controller poles. Thus, the error dynamics of the observer decay 2 – 6 times faster than the error dynamics of the controller, with the eigenvalues of the controller therefore governing the systems behaviour.

### 3.3.2 Observer-Based Disturbance Attenuating Controller

So far, there were only systems without disturbances considered for state control. Now an input disturbance is assumed similarly to [5, 13]. Figure 3.10 shows the structure of closed-loop system with conventional observer-based state control and input disturbance. Subsequently this concept is extended to obtain an observer-based disturbance attenuation controller (*OBDA controller*) as similarly presented in [20, 21].

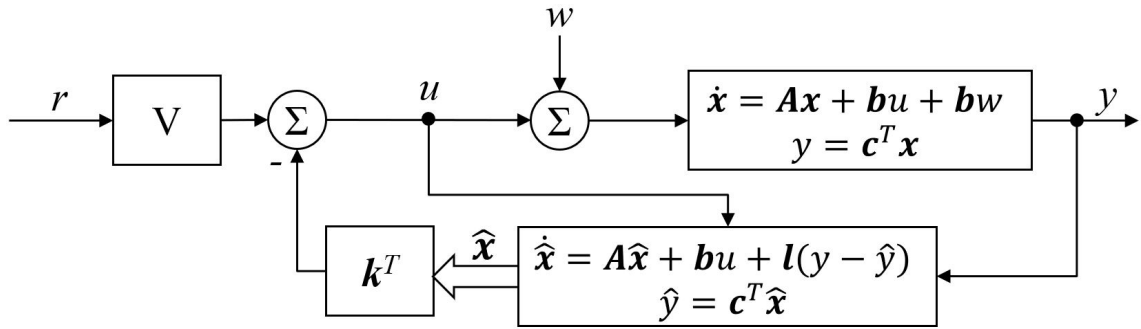


Figure 3.10: Block diagram of a closed-loop system with observer-based state feedback and input disturbance  $w$ .

Consider the plant as a LTI system of the form

$$\begin{aligned} \frac{d}{dt} \mathbf{x} &= \mathbf{A} \mathbf{x} + \mathbf{b} u + \mathbf{b} w, \\ y &= \mathbf{c}^T \mathbf{x}, \end{aligned}$$

and the observer is given as

$$\begin{aligned} \frac{d}{dt} \hat{\mathbf{x}} &= \mathbf{A} \hat{\mathbf{x}} + \mathbf{b} u + \mathbf{l}(y - \hat{y}), \\ \hat{y} &= \mathbf{c}^T \hat{\mathbf{x}}. \end{aligned}$$

The state feedback gain  $\mathbf{k}^T$  and observer gain  $\mathbf{l}$  are chosen such that  $(\mathbf{A} - \mathbf{b}\mathbf{k}^T)$  and  $(\mathbf{A} - \mathbf{l}\mathbf{c}^T)$  are Hurwitz.



Assuming a constant input disturbance  $w$ . The disturbance yields a constant estimation error for the equilibrium point given as

$$\begin{aligned}\frac{d}{dt}\tilde{\mathbf{x}} &= 0 = (\mathbf{A} - \mathbf{l}\mathbf{c}^T)\tilde{\mathbf{x}}_e + \mathbf{b}w, \\ \tilde{\mathbf{x}}_e &= -(\mathbf{A} - \mathbf{l}\mathbf{c}^T)^{-1}\mathbf{b}w\end{aligned}$$

A corrected estimation state  $\bar{\mathbf{x}}$  can therefore be calculated as

$$\bar{\mathbf{x}} = \hat{\mathbf{x}} - (\mathbf{A} - \mathbf{l}\mathbf{c}^T)^{-1}\mathbf{b}\hat{w},$$

where  $\hat{w}$  is an estimate of the unknown disturbance. With the corrected output estimate given as

$$\bar{y} = \mathbf{c}^T\bar{\mathbf{x}},$$

the disturbance estimate is obtained by

$$\begin{aligned}\frac{d}{dt}\hat{w} &= \mathbf{L}_w(y - \bar{y}), \\ \frac{d}{dt}\hat{w} &= \mathbf{L}_w\mathbf{c}^T(\mathbf{x} - \bar{\mathbf{x}}), \\ \frac{d}{dt}\hat{w} &= \mathbf{L}_w\mathbf{c}^T[\mathbf{x} - \hat{\mathbf{x}} + (\mathbf{A} - \mathbf{l}\mathbf{c}^T)^{-1}\mathbf{b}\hat{w}], \\ \frac{d}{dt}\hat{w} &= \mathbf{L}_w\mathbf{c}^T(\mathbf{A} - \mathbf{l}\mathbf{c}^T)^{-1}\mathbf{b}\hat{w} + \mathbf{L}_w\mathbf{c}^T\tilde{\mathbf{x}}.\end{aligned}\tag{3.23}$$

To get an asymptotic exact estimate of the disturbance  $w$ ,  $\mathbf{L}_w$  is chosen as

$$\mathbf{L}_w = \frac{-\alpha}{\mathbf{c}^T(\mathbf{A} - \mathbf{l}\mathbf{c}^T)^{-1}\mathbf{b}}, \quad \alpha > 0$$

and equation (3.23) reads

$$\frac{d}{dt}\hat{w} = -\alpha\hat{w} - \frac{-\alpha}{\mathbf{c}^T(\mathbf{A} - \mathbf{l}\mathbf{c}^T)^{-1}\mathbf{b}}(y - \hat{y}).$$

Hence, the corrected control law is given as

$$\begin{aligned}u &= -\mathbf{k}^T\bar{\mathbf{x}} - \hat{w} + Vr, \\ u &= -\mathbf{k}^T\hat{\mathbf{x}} + \left[\mathbf{k}^T(\mathbf{A} - \mathbf{l}\mathbf{c}^T)^{-1}\mathbf{b} - 1\right]\hat{w} + Vr.\end{aligned}$$

Figure 3.11 shows the corresponding block diagram of the OBDA controller. As indicated in the figure, the compensation of the disturbance can be summarised in the transfer function  $Q(s)$ . In order to systematically design an OBDA controller which suppresses sinusoidal disturbances of the form  $w = A\sin(\omega_w t + \phi_w)$  a design relying on transfer functions is used. Therefore, the transfer function  $G_{yw}(s)$  is obtained next.

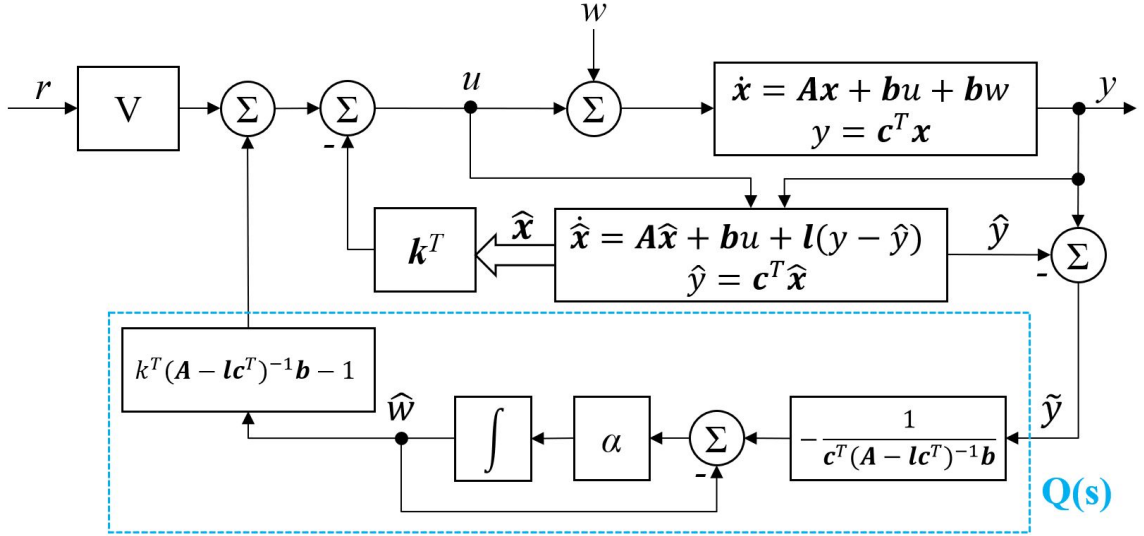


Figure 3.11: Block diagram of a closed-loop system with observer-based state feedback and disturbance rejection.

The estimation errors in the frequency domain are given as

$$\begin{aligned}\tilde{\mathbf{x}} &= (s\mathbf{E} - \mathbf{A} + \mathbf{l}\mathbf{c}^T)^{-1} \mathbf{b}w(s), \\ \tilde{y} &= \mathbf{c}^T \tilde{\mathbf{x}},\end{aligned}$$

with the transfer function  $G_{yw}(s)$  therefore derived as

$$\begin{aligned}s\mathbf{x}(s) &= (\mathbf{A} - \mathbf{b}\mathbf{k}^T) \mathbf{x}(s) + \mathbf{b} (\mathbf{k}^T \tilde{\mathbf{x}}(s) + Q(s)\tilde{y}(s) + w(s)), \\ \mathbf{x}(s) &= (s\mathbf{E} - \mathbf{A} + \mathbf{b}\mathbf{k}^T)^{-1} \mathbf{b} (\mathbf{k}^T \tilde{\mathbf{x}}(s) + Q(s)\mathbf{c}^T \tilde{\mathbf{x}}(s) + w(s)), \\ \mathbf{x}(s) &= (s\mathbf{E} - \mathbf{A} + \mathbf{b}\mathbf{k}^T)^{-1} \mathbf{b} \left[ (\mathbf{k}^T + Q(s)\mathbf{c}^T) (s\mathbf{E} - \mathbf{A} + \mathbf{l}\mathbf{c}^T)^{-1} \mathbf{b}w(s) + w(s) \right], \\ \mathbf{x}(s) &= (s\mathbf{E} - \mathbf{A} + \mathbf{b}\mathbf{k}^T)^{-1} \mathbf{b} \left[ \mathbf{k}^T (s\mathbf{E} - \mathbf{A} + \mathbf{l}\mathbf{c}^T)^{-1} \mathbf{b} \right. \\ &\quad \left. + Q(s)\mathbf{c}^T (s\mathbf{E} - \mathbf{A} + \mathbf{l}\mathbf{c}^T)^{-1} \mathbf{b} + 1 \right] w(s),\end{aligned}$$

finally yielding

$$\begin{aligned}G_{yw}(s) &= \frac{\mathbf{c}^T \mathbf{x}(s)}{w(s)}, \\ G_{yw}(s) &= \underbrace{\mathbf{c}^T (s\mathbf{E} - \mathbf{A} + \mathbf{b}\mathbf{k}^T)^{-1} \mathbf{b}}_{G_{yw1}(s)} \\ &\quad \cdot \underbrace{\left[ \mathbf{k}^T (s\mathbf{E} - \mathbf{A} + \mathbf{l}\mathbf{c}^T)^{-1} \mathbf{b} + Q(s)\mathbf{c}^T (s\mathbf{E} - \mathbf{A} + \mathbf{l}\mathbf{c}^T)^{-1} \mathbf{b} + 1 \right]}_{G_{yw2}(s)}.\end{aligned}$$

To suppress a disturbance with frequency  $\omega_w$ ,  $G_{yw}(j\omega_w) \stackrel{!}{=} 0$ . Since the zeros of  $G_{yw,1}(s)$  are the plant's zeros and cannot be changed  $G_{yw2}(j\omega_w) \stackrel{!}{=} 0$ . Therefore,

leading to

$$0 = \mathbf{k}^T (s\mathbf{E} - \mathbf{A} + \mathbf{l}\mathbf{c}^T)^{-1} \mathbf{b} + Q(s)\mathbf{c}^T (s\mathbf{E} - \mathbf{A} + \mathbf{l}\mathbf{c}^T)^{-1} \mathbf{b} + 1.$$

This finally yields the ideal transfer function

$$Q(s) = -\frac{1 + \mathbf{k}^T (s\mathbf{E} - \mathbf{A} + \mathbf{l}\mathbf{c}^T)^{-1} \mathbf{b}}{\mathbf{c}^T (s\mathbf{E} - \mathbf{A} + \mathbf{l}\mathbf{c}^T)^{-1} \mathbf{b}} \quad (3.24)$$

Considering the structure of the ideal transfer function

$$Q(s) = \frac{1 + \frac{\gamma(s)}{\hat{w}_o(s)}}{\frac{\mu(s)}{\hat{w}_o(s)}} = \frac{\hat{w}_o(s) + \gamma(s)}{\mu(s)}.$$

$\mu(s)$  is the numerator of the plant,  $\hat{w}_o(s)$  the desired characteristic equation of the observer and  $\gamma(s)$  a new obtained polynomial of maximum degree  $\deg(\gamma) \leq n$ . As previously mentioned,  $Q(s)$  must be stable, hence,  $\mu(s)$  must be stable. Furthermore,

$$\deg(\hat{w} + \gamma) = n \geq \deg(\mu),$$

and the transfer function is not proper if  $\deg(\mu) < n$ .

To circumvent this  $Q(s)$  can be approximated as

$$\tilde{Q}(s) = \frac{Q(s)}{\left(1 + \frac{s}{\beta}\right)^\rho}, \quad \rho = n - \deg(\mu), \quad \beta \gg \omega_w.$$

This ensures that  $|Q(s) - \tilde{Q}(s)| < \epsilon$  for  $\omega_w \ll \beta$ . However, the actual goal is  $G_{yw}(j\omega_w) = 0$  or at least very small. The approximation therefore yields

$$|G_{yw}(j\omega)| = |G_{yw1}(j\omega)| \left| \underbrace{\{G_{yw21}(j\omega) + Q(j\omega)G_{yw22}(j\omega)\}}_{0, \text{ by design}} - [Q(j\omega) - \tilde{Q}(j\omega)]G_{yw22}(j\omega) \right|,$$

$$|G_{yw}(j\omega)| = |G_{yw1}(j\omega)| |G_{yw22}(j\omega)| |\epsilon|.$$

Hence, when considering more disturbance frequencies, it is generally advisable to evaluate and replicate  $Q(j\omega)$  for the given frequencies  $\omega_{w,i}$

$$Q(j\omega_{w,i}) = \bar{Q}(j\omega_{w,i}), \quad i = 0, \dots, \kappa,$$

where  $\kappa$  is the numbers of frequencies to suppress, not counting the constant disturbance for  $\omega_{w,0} = 0$ . The final approximation can be formulated as

$$\bar{Q}(s) = \frac{b_{2\kappa}s^{2\kappa} + b_{2\kappa-1}s^{2\kappa-1} + \dots + b_1s + b_0}{(s + \lambda)^{2\kappa}}, \quad \lambda > 0. \quad (3.25)$$

The final system is shown in Figure 3.12, where  $Q(s)$  is approximated by the just derived  $\bar{Q}(s)$ .

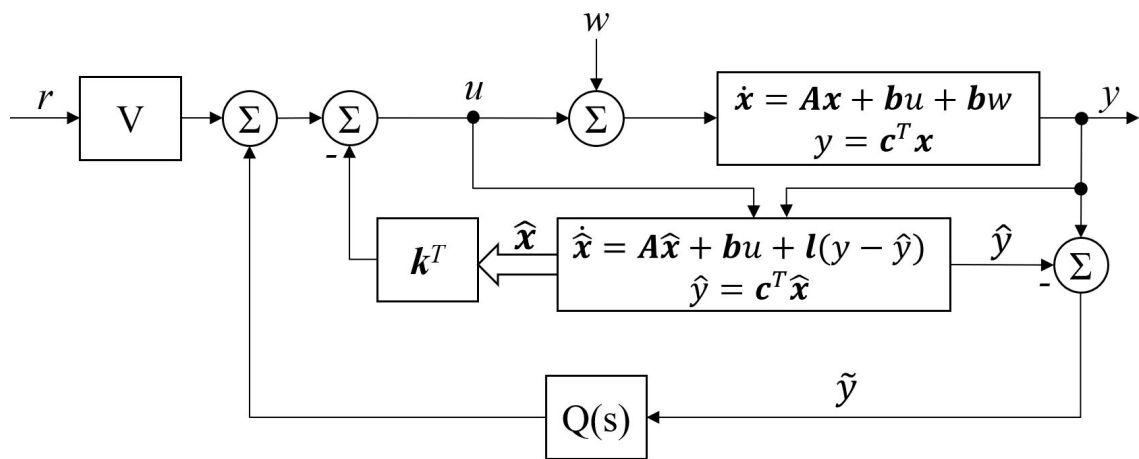


Figure 3.12: Block diagram of a closed-loop system with observer-based state feedback and disturbance rejection of the OBDA controller.  $Q(s)$  is designed to strongly attenuate constant disturbances and disturbances with specified frequencies at the system output.

# 4 Controller and Observer Designs for the test circuits

In this chapter, the different controller and observer approaches from the previous chapter are applied to the two test circuits discussed in Section 2.4.

Firstly, the designs for the series resonance circuit focus on conventional reference tracking and the capabilities of the presented observers. The controller designs for the integrator concentrate on disturbance attenuation.

Calculations and evaluations necessary for the subsequent design of the controllers and observers are mainly carried out with MATLAB as it provides a lot of useful tools and functions.

## 4.1 Series Resonance Test Circuit

As known from Section 2.4.1, the series resonance circuit is designed such that the output shows an overshoot when applying an input step. The circuit itself represents a stable plant. When the voltage across the capacitor finally matches the input voltage, the current through the circuit vanishes.

The state-space model already given in equation (2.17) reads as

$$\mathbf{x} = \begin{bmatrix} v_C \\ i_L \end{bmatrix}, \quad u = V_{in},$$

$$\frac{d}{dt}\mathbf{x} = \begin{bmatrix} 0 & \frac{1}{C} \\ -\frac{1}{L} & -\frac{R}{L} \end{bmatrix} \mathbf{x} + \begin{bmatrix} 0 \\ \frac{1}{L} \end{bmatrix} u,$$

$$y = [1 \quad 0] \mathbf{x},$$

with the component values given in Table 2.5.

For the controller designs, the circuit is supposed to have the maximum capacitance  $C_{max} = 79\mu F$ . This leads to the following numerical dynamics of the LTI system

$$\frac{d}{dt}\mathbf{x} = \begin{bmatrix} 0 & \frac{1}{0.000079} \\ -\frac{1}{0.4} & -\frac{36.7}{0.4} \end{bmatrix} \mathbf{x} + \begin{bmatrix} 0 \\ \frac{1}{0.4} \end{bmatrix} u, \quad (4.1)$$

$$\frac{d}{dt}\mathbf{x} = \underbrace{\begin{bmatrix} 0 & 12658.2 \\ -2.5 & -91.75 \end{bmatrix}}_{\mathbf{A}} \mathbf{x} + \underbrace{\begin{bmatrix} 0 \\ 2.5 \end{bmatrix}}_{\mathbf{b}} u.$$

The associated eigenvalues of the system matrix  $\mathbf{A}$  are  $s_1 = -45.88 + 171.88i$  and  $s_2 = -45.88 - 171.88i$ . As seen, the eigenvalues of the system matrix are complex conjugate which complies with the model referred as a system with complex conjugate poles in the modelling section. Furthermore, the real part of the eigenvalues is negative, confirming that the system is stable.

### 4.1.1 Controller Designs

With the numeric system for the series resonance system given (4.1), the controllability is checked first using *Kalman's controllability method* as in 3.1.1.

For the series resonance circuit, the system order  $n = 2$ . The resulting controllability matrix is

$$\mathbf{C}_u = [\mathbf{b}, \mathbf{A}\mathbf{b}],$$

$$\mathbf{C}_u = \left[ \begin{bmatrix} 0 \\ 2.5 \end{bmatrix}, \begin{bmatrix} 0 & 12658.2 \\ -2.5 & -91.75 \end{bmatrix} \begin{bmatrix} 0 \\ 2.5 \end{bmatrix} \right],$$

$$\mathbf{C}_u = \begin{bmatrix} 0 & 31645.57 \\ 2.5 & -229.38 \end{bmatrix}.$$

As can be seen, the matrix  $\mathbf{C}_u$  has two linearly independent column vectors and hence

$$\text{rank}(\mathbf{C}_u) = 2 = n.$$

Therefore, the pair  $(\mathbf{A}, \mathbf{b})$  is considered controllable and a controller design for the system is feasible.

#### 4.1.1.1 PID Controller

The PID controller is designed using *Ziegler-Nichols Ultimate Gain Method*. The previously described experiment from Section 3.1.2.1 was carried out on the laboratory set-up with the series resonance test circuit. Within the MATLAB Simulink

simulation, the proportional gain was slowly increased until the instability boarder was reached with an ultimate gain  $k_u = 1.5$ . Figure 4.1 shows the resulting oscillation with an ultimate period  $T_u = 22ms$ .

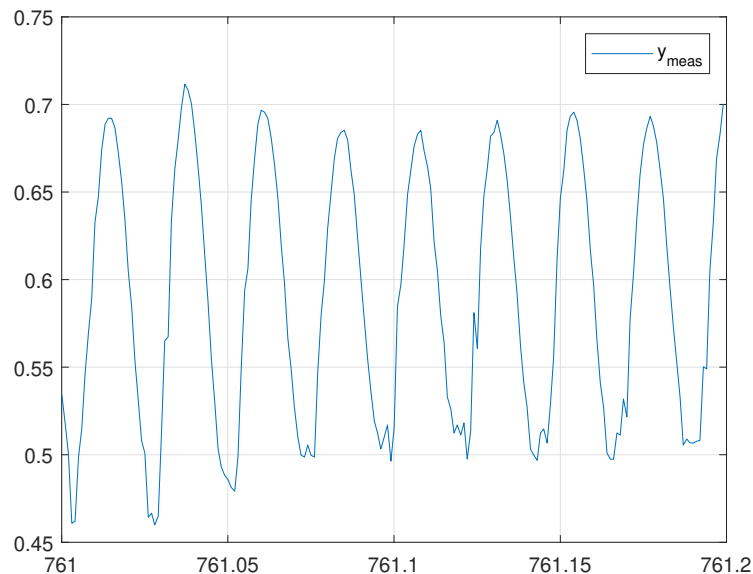


Figure 4.1: Resulting oscillation of the series resonance test circuit experiment with ultimate gain  $k_u = 1.5$ . The measured ultimate period is  $T_u = 22ms$ .

Figure 4.2 shows the bode plot of the series resonance with the phase margin. As can be seen, the gain margin is listed as infinite, since the phase plot does not reach  $-180^\circ$ . Hence, there should not be an ultimate gain, or at least a really high one. However, in the experimental set-up, the proportional gain of 1.5 lead to a nearly constant oscillation with a very small amplitude decay. Higher gains resulted in an immediate saturation of the test circuit probably due to the limitations of the actuation range. Nevertheless, the resulting parameters were taken as initial values for further tuning of the PID parameters.

Using the obtained experimental parameters and the Ziegler-Nichols tuning rules from Table 3.2 leads to the suggested PID parameter setting shown in Table 4.1.

$k_p$	$k_i$	$k_d$
0.9	81.8	0.0025

Table 4.1: Experimentally obtain PID gains using Ziegler-Nichols ultimate gain method.

#### 4.1.1.2 LS Controller

The second controller is designed via *loop-shaping* as discussed in Section 3.1.3. As the mathematical model of the series resonance test circuit is already given in

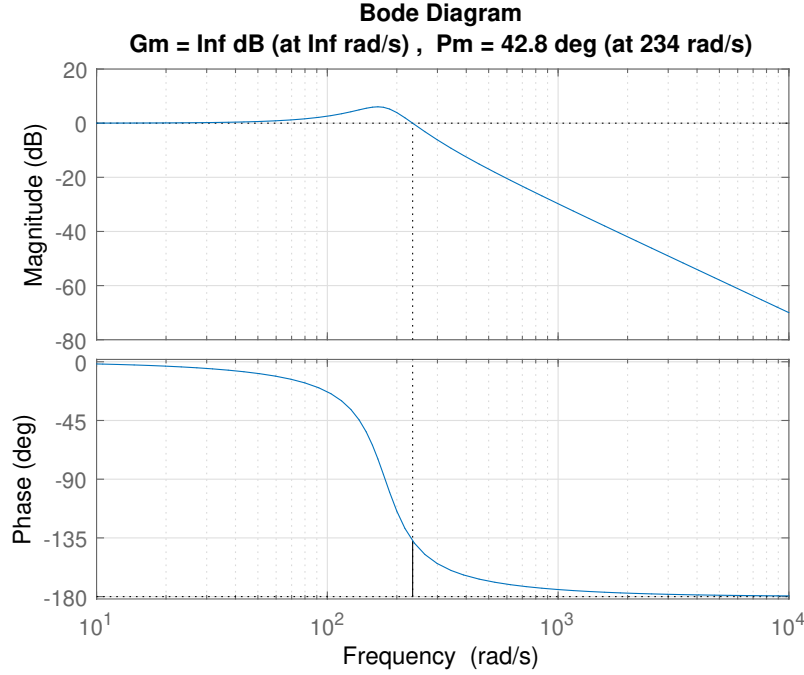


Figure 4.2: Bode plot of the given series resonance circuit. As can be seen, the phase margin is  $42.8^\circ$  at  $234\text{rad/s}$ . However, since the circuit does not reach  $-180^\circ$  phase, there is no finite gain margin listed.

(4.1), no further experiments need to be performed to obtain the frequency-domain characteristics. However, since the mathematical model is a state-space model, at first the transfer function of the plant must be obtained. The equation therefore is given as

$$P(s) = \mathbf{c}^T (s\mathbf{E} - \mathbf{A})^{-1} \mathbf{b} + d,$$

where  $\mathbf{E}$  represents the identity matrix of size  $n \times n$ , and  $d$  the direct feedthrough of the plant input to its output.

For the given series resonance circuit, this leads to

$$\begin{aligned} P(s) &= \mathbf{c}^T (s\mathbf{E} - \mathbf{A})^{-1} \mathbf{b} + d, \\ P(s) &= [1 \ 0] \left( s \begin{bmatrix} 1 & 0 \\ 0 & 1 \end{bmatrix} - \begin{bmatrix} 0 & 12658.2 \\ -2.5 & -91.75 \end{bmatrix} \right)^{-1} \begin{bmatrix} 0 \\ 2.5 \end{bmatrix} + 0, \\ P(s) &= \frac{31645.57}{s^2 + 91.65s + 31645.57}. \end{aligned} \quad (4.2)$$

The corresponding bode plot is shown already in Figure 4.2. As can be seen, the maximum magnitude spike is at about  $175\text{rad/s}$  which corresponds to calculated resonance frequency of the series resonance circuit of about  $28\text{Hz}$ .

The actual design process is started by defining the desired response of the closed-loop system. Hence, a rise time  $t_r = 0.05\text{s}$  and an overshooting percentage  $o_p = 10\%$



are specified. This leads to a cutoff frequency

$$\omega_c \approx \frac{1.5}{t_r} = \frac{1.5}{0.05},$$

$$\omega_c \approx 30 \text{ rad/s},$$

and a phase margin

$$\phi_m \approx 70 - o_p = 70 - 10,$$

$$\phi_m \approx 60^\circ.$$

As seen in Figure 4.2, the plant has no integrating behaviour as it does not amplify low frequencies. Hence, the first controller term is an integrator

$$C_1(s) = \frac{1}{s}.$$

The integrator has a constant slope of  $-20_{dB}/decade$  with gain crossover frequency of  $1 \text{ rad/s}$  and a phase shift of  $-90^\circ$ . Figure 4.3 shows resulting open-loop  $L_1(s)$  after adding the integrator. Although the magnitude at the cutoff frequency is now well below the unity gain, frequencies below the cutoff frequency are attenuated less. By adding a constant gain to the controller later on, the whole magnitude can be shifted upward leading to an amplification for lower frequencies which satisfies design point 1 from Section 3.1.3.1.

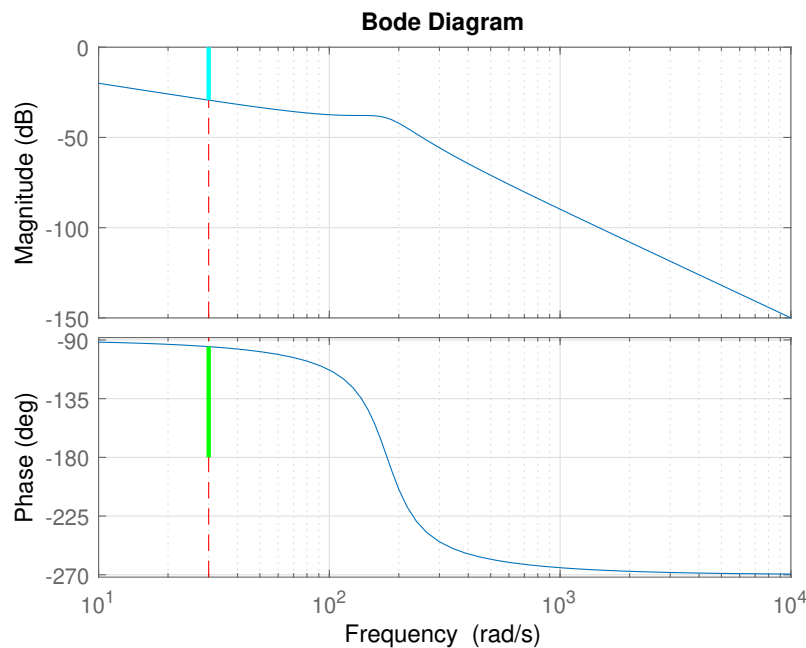


Figure 4.3: Bode plot of the open-loop  $L_1(s) = C_1(s)P(s)$ . The dashed red line highlights the desired cutoff frequency. The magnitude difference  $g_c$  to the unity gain is emphasised in cyan and the green line highlights the phase margin  $\phi_m$ .

Next design step is to determine the phase margin. From the specification a phase margin of  $60^\circ$  is desired. As seen in Figure 4.3, the actual phase margin is about  $85^\circ$ , hence overachieving the specification. Therefore, two actions can be taken

- A a conservative approach where no further phase shaping is done or
- B a more aggressive approach following the rule of thumb that pushes the phase down at the desired cutoff frequency to satisfy  $60^\circ$  phase margin.

For demonstration purposes both approaches are carried out. At first, approach A is considered:

With sufficient phase margin, the open-loop is subsequently checked if the slope at the desired cutoff frequency is about  $-20_{dB}/decade$ . Again looking at Figure 4.3, it can be seen that the magnitude slope around the dashed red line satisfies this criteria and hence design point 2.

Also design point 3 is fulfilled since high frequencies are attenuated strongly.

The final design step is to shift the magnitude upwards that the magnitude at the desired cutoff frequency is 1 or  $0_{dB}$  in the bode plot. Hence, the magnitude  $g_c$  at the desired cutoff frequency is evaluated. For the controller this consequently yields

$$C_2(s) = \frac{1}{g_c} = \frac{1}{0.0342},$$

$$C_2(s) = 29.26.$$

Since the controller  $C_2(s)$  is only proportional, there is no phase shift. The final LS controller is given by

$$C_A(s) = C_1(s)C_2(s),$$

$$C_A(s) = \frac{29.26}{s}.$$

Figure 4.4 shows the final open-loop circuit using the conservative approach A.

With approach A finished, design approach B is carried out next continuing from  $L_1(s) = C_1(s)P(s)$ . The phase margin at the desired cutoff was  $25^\circ$  to high. To shift the phase downwards but keeping the impact on magnitude small, a *lag compensator*, as discussed in Section 3.1.3.2, is used.

For a desired phase shift  $\Delta\phi = -25^\circ$ , this leads to

$$m = \frac{1 + \sin(\Delta\phi)}{1 - \sin(\Delta\phi)} = \frac{1 + \sin(-25^\circ)}{1 - \sin(-25^\circ)},$$

$$m = 0.4059.$$

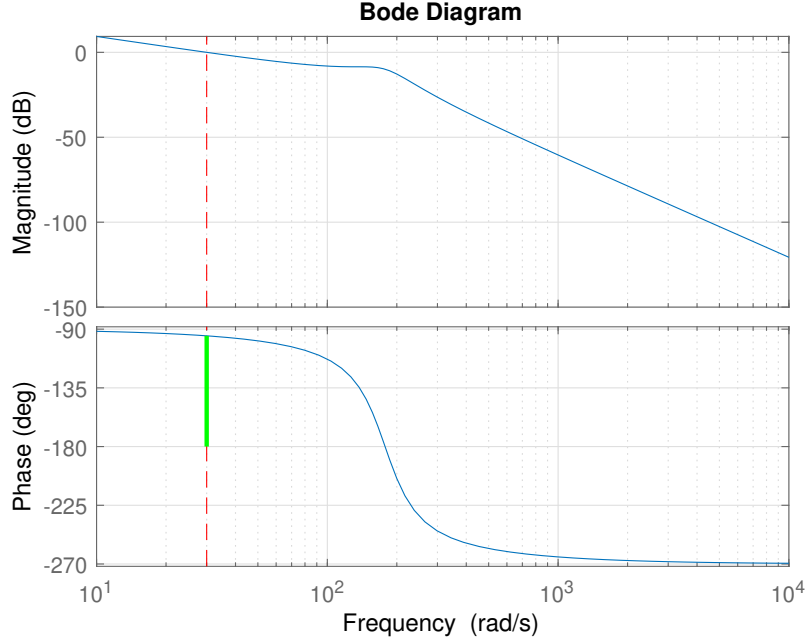


Figure 4.4: Bode plot of the final open-loop  $L_A(s) = C_1(s)C_2(s)P(s)$  using the conservative design approach A. The dashed red line highlights the desired cutoff frequency and the green line the phase margin  $\phi_m$ . Frequencies far below the cutoff frequency are amplified yielding good reference tracking, whereas high frequencies are strongly attenuated. The magnitude cuts the unity gain approximately with the desired  $-20_{dB}/decade$ .

and further to

$$\omega_n = \frac{\omega_m}{\sqrt{m}} = \frac{30rad/s}{\sqrt{0.4059}},$$

$$\omega_n = 47.09rad/s,$$

and

$$\omega_d = \omega_m \sqrt{m} = 30rad/s \sqrt{0.4059},$$

$$\omega_d = 19.11rad/s.$$

The resulting compensator reads as

$$C_3(s) = \frac{1 + \frac{s}{\omega_n}}{1 + \frac{s}{\omega_d}},$$

$$C_3(s) = \frac{1 + \frac{s}{47.09}}{1 + \frac{s}{19.11}},$$

with the bode plot of this lag compensator shown in Figure 4.5.

The updated open-loop  $L_3(s)$  is seen in Figure 4.6. As desired, the phase margin at the cutoff frequency now equals  $60^\circ$ .

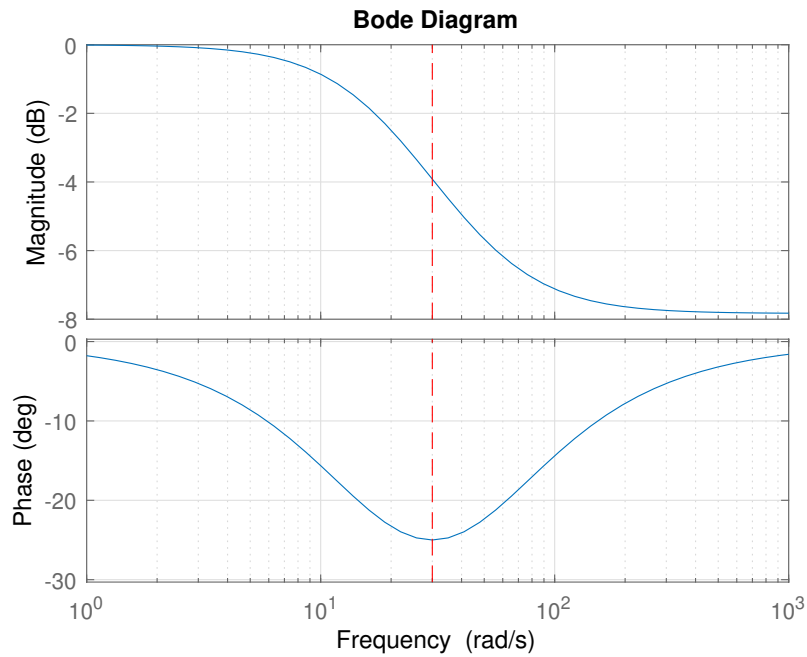


Figure 4.5: Bode plot of the lag compensator. The maximum phase shift is at the desired cutoff frequency (dashed red line).

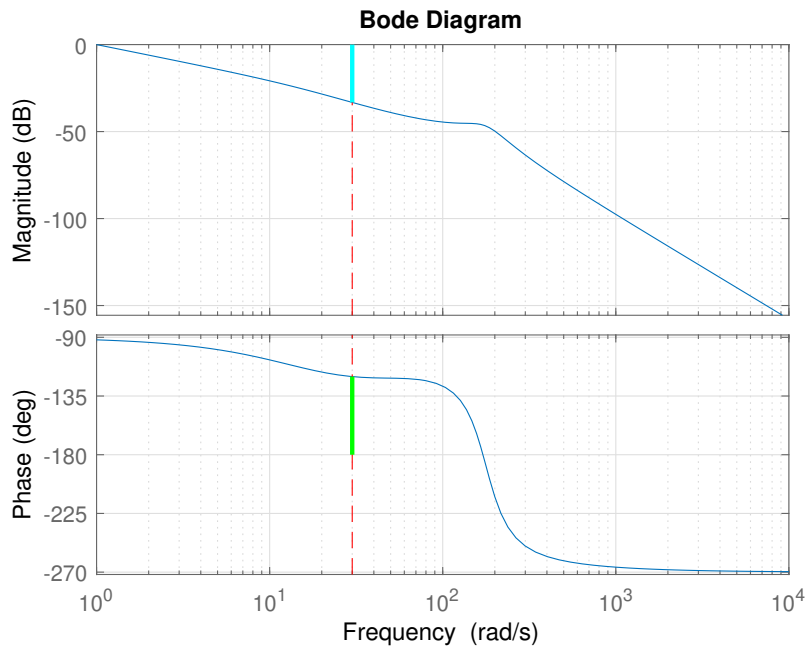


Figure 4.6: Bode plot of the open-loop  $L_3(s) = C_1(s)C_3(s)P(s)$ . The dashed red line highlights the desired cutoff frequency and due to the introduced lag compensator the phase margin  $\phi_m$  now equals  $60^\circ$  (green). The magnitude difference  $g_c$  to the unity gain is indicated in cyan.

As for the design approach A, the last step of the loop-shaping is to shift the magnitude up to obtain unity gain at the desired cutoff frequency. This is again done using the current gain at the desired cutoff frequency yielding

$$C_4(s) = \frac{1}{g_c} = \frac{1}{0.0218},$$

$$C_4(s) = 45.93.$$

Therefore, the final controller using design approach B is given as

$$C_B(s) = C_1(s)C_3(s)C_4(s),$$

$$C_B(s) = \frac{1}{s} \cdot \frac{1 + \frac{s}{47.09}}{1 + \frac{s}{19.11}} \cdot 45.93,$$

$$C_B(s) = \frac{18.64s + 877.9}{s^2 + 19.11s}.$$

Figure 4.7 shows the two resulting closed-loop step responses of the system. As can be seen, the conservative design approach A (Figure 4.7a) yields a much slower rise time compared to design approach B which satisfies the rules of thumb. As specified, the design approach B approximately meets the specification of 10% overshooting and a 0.05s rise time. However, both designs lead to a similar settling time. Nevertheless, as already stated in Section 3.1.3, controller design via loop-shaping is trial and error, with the obtained controllers not necessarily working exactly as expected like in this case.

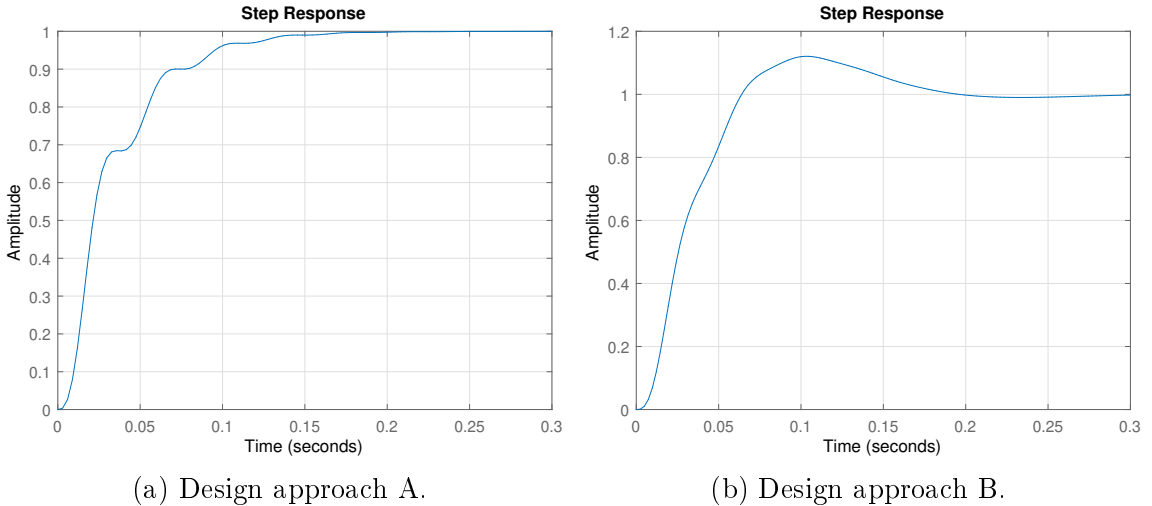


Figure 4.7: Step responses of the closed-loop system with the two designed LS controllers using (a) the conservative design approach A and (b) the design approach B following the rules of thumb as defined in [10].

### 4.1.1.3 State Controller

As third controller for the series resonance circuit, a state controller is designed as shown in Section 3.1.4. Actually, there are two controllers designed, one using eigenvalue assignment via *Ackermann's formula*, the other one utilising a quadratic cost function (*LQR*).

#### Eigenvalue Assignment

At first, the desired poles of the system are specified. Since the order of the given series resonance circuit  $n = 2$ , two poles are required. To obtain a stable system the poles need to be located in the left open complex plane, hence chosen at  $s_1 = s_2 = -100$ . This leads to a desired characteristic equation

$$w(s) = (s + 100)^2 = s^2 + 200s + 10000.$$

The controllability matrix of the series resonance circuit as given in 4.1.1 and its inverse read

$$\mathbf{C}_u = \begin{bmatrix} 0 & 31645.57 \\ 2.5 & -229.38 \end{bmatrix}, \quad \mathbf{C}_u^{-1} = \begin{bmatrix} 0.0029 & 0.4 \\ 3.16 \cdot 10^{-5} & 0 \end{bmatrix},$$

leading to

$$\mathbf{t}_1^T = [3.16 \cdot 10^{-5} \quad 0].$$

The system matrix and squared system matrix are given as

$$\mathbf{A} = \begin{bmatrix} 0 & 12658.2 \\ -2.5 & -91.75 \end{bmatrix}, \quad \mathbf{A}^2 = \begin{bmatrix} -31645.57 & -1161392 \\ 229.375 & -23227.51 \end{bmatrix}.$$

Using *Ackermann's formula*, the final controller parameters are given as

$$\begin{aligned} \mathbf{k}^T &= \mathbf{t}_1^T w(\mathbf{A}), \\ \mathbf{k}^T &= \mathbf{t}_1^T [10000\mathbf{I} + 200\mathbf{A} + \mathbf{A}^2], \\ \mathbf{k}^T &= [3.16 \cdot 10^{-5} \quad 0] \left( 10000 \begin{bmatrix} 1 & 0 \\ 0 & 1 \end{bmatrix} + 200 \begin{bmatrix} 0 & 12658.2 \\ -2.5 & -91.75 \end{bmatrix} \right. \\ &\quad \left. + \begin{bmatrix} -31645.57 & -1161392 \\ 229.375 & -23227.51 \end{bmatrix} \right), \\ \mathbf{k}^T &= [-0.684 \quad 43.3]. \end{aligned}$$

The last step of the controller design is to obtain the scaling factor for reference variable as in equation 3.5. For the given series resonance circuit this leads to

$$V = -\frac{1}{\mathbf{c}^T(\mathbf{A} - \mathbf{b}\mathbf{k}^T)^{-1}\mathbf{b}},$$

$$V = -\frac{1}{[1 \ 0] \left( \begin{bmatrix} 0 & 12658.2 \\ -2.5 & -91.75 \end{bmatrix} - \begin{bmatrix} 0 \\ 2.5 \end{bmatrix} [-0.684 \ 43.3] \right)^{-1} \begin{bmatrix} 0 \\ 2.5 \end{bmatrix}},$$

$$V = 0.316.$$

Hence, the final control law for the designed state controller using eigenvalue assignment reads

$$u = -[-0.684 \ 43.3]\mathbf{x} + 0.316r.$$

### LQR

The second design of the state controller, the *linear-quadratic-regulator* is the optimal solution regarding the cost function

$$J = \frac{1}{2} \int_0^{\infty} [\mathbf{x}^T \mathbf{Q} \mathbf{x} + \mathbf{u}^T \mathbf{R} \mathbf{u}] dt.$$

from Section 3.1.4.2.

Since the given series resonance circuit has only one input, the matrix  $\mathbf{R}$  becomes a scalar and  $\mathbf{Q}$  is a  $2 \times 2$  matrix corresponding with the two state variables of the system. For the design of the controller, the cost matrix  $\mathbf{Q}$  and scalar  $R$  are specified as

$$\mathbf{Q} = \begin{bmatrix} 5 & 0 \\ 0 & 1 \end{bmatrix}, \quad R = 10.$$

With one input, matrices  $\mathbf{B}$  and  $\mathbf{K}$  become column respectively row vectors and the ARE from equation (3.8) reads

$$\mathbf{P}\mathbf{A} + \mathbf{A}^T\mathbf{P} - \mathbf{P}\mathbf{b}R^{-1}\mathbf{b}^T\mathbf{P} + \mathbf{Q} = \mathbf{0},$$

The ARE can be solved in MATLAB using the `care` command. For the given setting this results

$$\mathbf{P} = \begin{bmatrix} 0.0292 & 0.8990 \\ 0.8990 & 93.9617 \end{bmatrix}.$$

The optimal feedback gains for this problem using equation (3.7) are hence

$$\begin{aligned}\mathbf{k}^T &= \frac{1}{R} \mathbf{b}^T \mathbf{P}, \\ \mathbf{k}^T &= \frac{1}{10} [0 \quad 2.5] \begin{bmatrix} 0.0292 & 0.8990 \\ 0.8990 & 93.9617 \end{bmatrix}, \\ \mathbf{k}^T &= [0.2247 \quad 23.49].\end{aligned}$$

Again the scaling factor for the reference variable is calculated as in equation (3.5)

$$\begin{aligned}V &= -\frac{1}{\mathbf{c}^T (\mathbf{A} - \mathbf{b} \mathbf{k}^T)^{-1} \mathbf{b}}, \\ V &= -\frac{1}{[1 \quad 0] \left( \begin{bmatrix} 0 & 12658.2 \\ -2.5 & -91.75 \end{bmatrix} - \begin{bmatrix} 0 \\ 2.5 \end{bmatrix} [0.2247 \quad 23.49] \right)^{-1} \begin{bmatrix} 0 \\ 2.5 \end{bmatrix}}, \\ V &= 1.2247.\end{aligned}$$

The final control law read as

$$u = -[0.2247 \quad 23.49] \mathbf{x} + 1.2247r.$$

#### 4.1.1.4 PI-State Controller

The PI-state controller is designed next according to Section 3.1.5. There it is shown that the PI-state controller extends the system order by one state (the integrator value of the controller) and the controller parameters can be obtained using the same methods as for the state controller. Furthermore, it is required that the plant has no zeros at  $s = 0$ .

From the transfer function previously given in equation (4.2) as

$$P(s) = \frac{31645.57}{s^2 + 91.65s + 31645.57},$$

it can be seen that the system fulfils this requirement.

The poles of the closed-loop system are specified at  $s_1 = s_2 = s_3 = -200$ , with the calculation using *Ackerman's formula* yielding

$$\tilde{\mathbf{k}}^T = [2.792 \quad 203.3 \quad -252.8].$$

The integral gain can be obtained by the last element of the vector  $\tilde{\mathbf{k}}^T$ , i.e.

$$k_i = \tilde{k}_{n+1} = -252.8.$$



The proportional error gain is chosen according equation (3.11) as

$$k_p = \frac{1}{\mathbf{c}^T \mathbf{A}^{-1} \mathbf{b}},$$

$$k_p = \frac{1}{\begin{bmatrix} 1 & 0 \end{bmatrix} \begin{bmatrix} 0 & 12658.2 \\ -2.5 & -91.75 \end{bmatrix}^{-1} \begin{bmatrix} 0 \\ 2.5 \end{bmatrix}},$$

$$k_p = -1.$$

Hence, resulting the state feedback parameters are

$$\mathbf{k}^T = [\tilde{k}_1 \quad \dots \quad \tilde{k}_n] + k_p \mathbf{c}^T$$

$$\mathbf{k}^T = [2.792 \quad 203.3] + (-1) [1 \quad 0],$$

$$\mathbf{k}^T = [1.792 \quad 203.3].$$

#### 4.1.1.5 1-Sliding Controller

The 1-sliding controller is designed as shown in Section 3.1.6. For the given series resonance circuit, the control error  $e = r - y = r - x_1$  should decay with a rate of  $\lambda$

$$e = r - x_1,$$

$$\frac{d}{dt}e = \frac{d}{dt}r - \frac{d}{dt}x_1,$$

$$\frac{d}{dt}e = \frac{d}{dt}r - \frac{1}{C}x_2 \stackrel{!}{=} -\lambda(r - x_1) = -\lambda e$$

and therefore

$$x_2 = -d(x_1),$$

$$x_2 = \lambda C(r - x_1) + C \frac{d}{dt}r.$$

The sliding manifold is subsequently chosen as

$$\sigma = x_2 + d(x_1) = 0,$$

$$\sigma = x_2 - \lambda C(r - x_1) - C \frac{d}{dt}r.$$

Next the calculation of the control law leads to

$$\frac{d}{dt}\sigma \stackrel{!}{=} -k \operatorname{sgn}(\sigma),$$

$$\frac{d}{dt}x_2 - \lambda C \left( \frac{d}{dt}r - \frac{d}{dt}x_1 \right) - C \frac{d^2}{dt^2}r = -k \operatorname{sgn}(\sigma),$$

$$-\frac{1}{L}x_1 - \frac{R}{L}x_2 + \frac{1}{L}u - \lambda C \left( \frac{d}{dt}r - \frac{1}{C}x_2 \right) - C \frac{d^2}{dt^2}r = -k \operatorname{sgn}(\sigma),$$

$$x_1 + (R - \lambda L)x_2 + \lambda LC \frac{d}{dt}r + LC \frac{d^2}{dt^2}r + L[-k \operatorname{sgn}(\sigma)] = u. \tag{4.3}$$

A state transformation yields

$$\begin{bmatrix} x_1 \\ x_2 \end{bmatrix} \rightarrow \begin{bmatrix} e \\ \sigma \end{bmatrix}, \quad \frac{d}{dt} \begin{bmatrix} e \\ \sigma \end{bmatrix} = \begin{bmatrix} -\lambda e - \frac{1}{C}\sigma \\ -k \operatorname{sgn}(\sigma) \end{bmatrix}. \quad (4.4)$$

As can be seen from equation (4.4), the sliding variable is driven to the sliding manifold  $\sigma = 0$ . At the sliding manifold the order of the system is reduced and the system is solely governed by the design parameter  $\lambda$ . However, as seen from equation (4.3) the control law requires the first and second time-derivative of the reference variable which may cause problems. Furthermore, also the sliding variable contains the time-derivative of the reference variable.

One possibility to avoid this problem is to neglect these two terms in the control law and assume them as uncertainty or perturbation as well as neglecting the derivative in the sliding variable. Nonetheless this approach requires to increase the gain  $k$  and hence chattering may be amplified. Additionally the sliding variable is actually not really zero, thus the system is not only driven by the specified dynamics. Therefore, neglecting the derivatives is only feasible if the reference signal consists mainly of steps. Another way to tackle this problem is to use *robust exact differentiators* as proposed in [22], which easily allow to obtain these derivatives.

The control law of the 1-sliding controller is already given in equation (4.3). The only parameters for the controller are the decay parameter  $\lambda$  and the controller gain  $k$ , where  $k$  must be chosen that it always compensates any given uncertainty.

Hence,  $\lambda = 250$  is chosen to give the control error more weight in the sliding function. Furthermore, as no big deviations were shown at the model verification (Figure 2.33),  $k = 0.4$  is chosen to cope with any uncertainties.

#### 4.1.1.6 Super-Twisting Controller

The design steps of the super-twisting controller are carried out as previously for the 1-sliding controller. However, this time the function of the super-twisting algorithm from Section 3.1.7 is utilised. The control law can therefore directly be written as

$$u = x_1 + (R - \lambda L)x_2 + \lambda LC \frac{d}{dt}r + LC \frac{d^2}{dt^2}r + L \left( -k_1 \sqrt{|\sigma|} \operatorname{sgn}(\sigma) + w \right),$$

$$\frac{d}{dt}w = -k_2 \operatorname{sgn}(\sigma).$$

As for the 1-sliding controller, the problem with derivatives of the reference variable is still present and can be handled as discussed previously. With the super-twisting algorithm the discontinuity occurs in the second time-derivative of the sliding variable and hence the first derivative of the control law. Therefore, the generated control function is continuous.

The choice of controller parameters as proposed in [16] is

$$\begin{aligned} k_1 &= 1.5\sqrt{M}, \\ k_2 &= 1.1M, \end{aligned}$$

where  $M$  is the Lipschitz constant of the maxim perturbation respectively uncertainty.

Since there are no "big" uncertainties, even when neglecting the second derivative of the control variable,  $M = 10$  and  $\lambda = 250$  are specified for the controller design.

#### 4.1.1.7 Feedforward Control

The feedforward control is designed according to Section 3.1.8. The transfer functions of the feedforward control can directly be read from the plant transfer function. Hence,

$$F(s) = s^2 + 91,65s + 31645.57, \quad \text{and} \quad E(s) = 31645.57.$$

The only remaining task is to obtain the trajectory to perform a switch of operation points. For the series resonance circuit it is specified that the operation point should be shifted from  $y = 0$  to  $y = 1$  with a transition time  $T_t = 0.05s$ . Thus, the start and end conditions are

$$z_s^*(t) = 0, \quad z_e^*(t) = \frac{1}{\mu_0} = 3.16 \cdot 10^{-5}.$$

The trajectory function can be obtained using equation (3.17) and Table 3.3. Finally this yields

$$\begin{aligned} z^*(t) &= z_s^* + (z_e^* - z_s^*) \sum_{i=3}^5 \tilde{\gamma}_i \frac{t^i}{T_t^i}, \\ z^*(t) &= 0 + (3.16 \cdot 10^{-5} - 0) \left( \tilde{\gamma}_3 \frac{t^3}{0.05^3} + \tilde{\gamma}_4 \frac{t^4}{0.05^4} + \tilde{\gamma}_5 \frac{t^5}{0.05^5} \right), \\ z^*(t) &= 3.16 \cdot 10^{-5} \left( 10 \frac{t^3}{0.05^3} - 15 \frac{t^4}{0.05^4} + 6 \frac{t^5}{0.05^5} \right), \\ z^*(t) &= 2.5280t^3 - 75.84t^4 + 606.72t^5. \end{aligned}$$

Figure 4.8 shows the behaviour of the planned trajectory  $z^*$  for the change of the operation point.

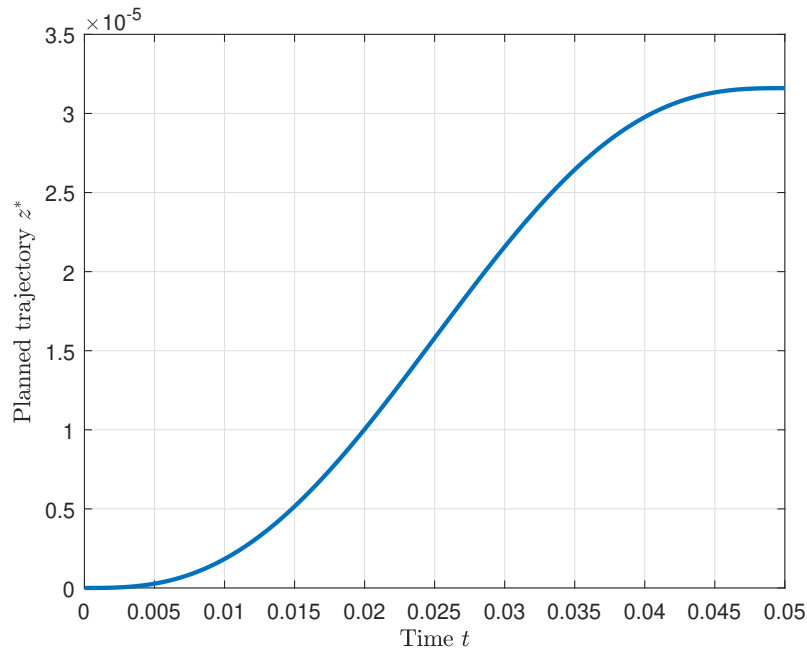


Figure 4.8: Simulation of the planned trajectory during the change of operation points.

## 4.1.2 Controller Designs for Current Controlled Circuit

In this section the controlled output of the series resonance circuit is changed from the capacitor voltage to the inductor current. Therefore, the only change for the system (2.17) is the output vector which changes to

$$\mathbf{c}^T = [0 \ 1].$$

### 4.1.2.1 State Controller

The state controller design can be executed as in Section 4.1.1.3. Therefore, the poles are specified as  $s_1 = s_2 = -100$ .

Using *Ackermann's formula* for the eigenvalue assignment, this again leads to the same feedback gain as in Section 4.1.1.3

$$\mathbf{k}^T = [-0.684 \ 43.3],$$

since  $\mathbf{c}^T$  has no influence on the internal dynamics.

However, the current controlled circuit has differentiating behaviour i.e.  $P(s=0) = T(s=0) = 0$ . Hence, the input scaling requires an infinite gain and therefore making state control not possible for steady state control. However, it is possible to control the circuit for given frequencies and match the output amplitude.

Therefore, a frequency  $\omega_s = 2\pi \cdot 2Hz = 12.57rad/s$  is specified. The transfer function from the reference input to the output is given as

$$T(s) = \frac{2.5s}{s^2 + 200 + 10000},$$

and evaluated for the given frequency  $T(j\omega_s)$ . This leads to an amplitude and phase of

$$|T(j\omega_s)| = 0.0031, \quad \angle T(j\omega_s) = 75.67^\circ.$$

By setting the scaling of the reference input to

$$V = \frac{1}{|T(s)|} \Big|_{s=j\omega_s} = \frac{1}{0.0031} = 323.34,$$

the output amplitude matches the input amplitude at the specified frequency ( $\omega_s = 12.57rad/s$ ). However, there is a phase shift of  $75.67^\circ$ .

Another possibility which is not shown is to choose the poles such that the phase of the numerator and denominator of  $T(s)$  match at the given frequency. Furthermore, by scaling the reference variable correctly the input and output can be matched exactly for the specified frequency.

#### 4.1.2.2 Super-Twisting Controller

For the super-twisting controller, the approach for this problem differs from sections 4.1.1.6 since the control signal directly occurs in the dynamics of the output

$$\frac{d}{dt}y = \frac{d}{dt}x_2 = -\frac{1}{L}x_1 - \frac{R}{L}x_2 + \frac{1}{L}u.$$

Hence, the sliding variable can be directly chosen as

$$\sigma = r - y = r - x_2.$$

The super-twisting controller then ensures that the output follows the input.

Therefore, the control law can be calculated as

$$\begin{aligned} \frac{d}{dt}\sigma &= -k_1\sqrt{|\sigma|}\operatorname{sgn}(\sigma) + w, \\ \dot{r} + \frac{1}{L}x_1 + \frac{R}{L}x_2 - \frac{1}{L}u &= -k_1\sqrt{|\sigma|}\operatorname{sgn}(\sigma) + w \\ L\dot{r} + x_1 + Rx_2 + L\left(k_1\sqrt{|\sigma|}\operatorname{sgn}(\sigma) - w\right) &= u, \end{aligned}$$

with

$$\frac{d}{dt}w = -k_2\operatorname{sgn}(\sigma).$$

The factor  $M$  is chosen as 2, aligned with the amplitude of the reference input of the performed test measurements. The final controller parameters are given as

$$\begin{aligned}k_1 &= 1.5\sqrt{M} = 1.5 \cdot \sqrt{2} = 2.12, \\k_2 &= 1.1M = 1.1 \cdot 2 = 2.2.\end{aligned}$$

### 4.1.3 Observer Designs

All of the presented observer designs in Section 3.2 are designed and applied to the series resonance circuit. However, at first the observability of the system must be validated. For the given circuit the observability matrix reads

$$\begin{aligned}\mathbf{O}_y &= \begin{bmatrix} \mathbf{c}^T \\ \mathbf{c}^T \mathbf{A} \end{bmatrix}, \\ \mathbf{O}_y &= \begin{bmatrix} [1 \ 0] \\ [1 \ 0] \begin{bmatrix} 0 & 12658.2 \\ -2.5 & -91.75 \end{bmatrix} \end{bmatrix}, \\ \mathbf{O}_y &= \begin{bmatrix} 1 & 0 \\ 0 & 12658.2 \end{bmatrix}.\end{aligned}$$

As can be seen, the matrix  $\mathbf{O}_y$  has full rank and according *Kalman's observability criteria* from Section 3.2.1 the pair  $(\mathbf{A}, \mathbf{c}^T)$  is fully observable.

#### 4.1.3.1 Luenberger Observer

The Luenberger estimator is designed as shown in 3.2.2, with observer error and the dynamics of the observer formulated accordingly as

$$\tilde{\mathbf{x}} = \mathbf{x} - \hat{\mathbf{x}},$$

respectively

$$\frac{d}{dt}\hat{\mathbf{x}} = \mathbf{A}\hat{\mathbf{x}} + \mathbf{b}u + \mathbf{l}(y - \hat{y}).$$

The resulting error dynamics given as

$$\frac{d}{dt}\tilde{\mathbf{x}} = (\mathbf{A} - \mathbf{l}\mathbf{c}^T)\tilde{\mathbf{x}}.$$

The calculation of the observer gains is done using LQR as cost function, hence needing to solve the *ARE*. Without much thought, the parameters are specified as  $\mathbf{Q} = \mathbf{E}$  and  $R = 1$ . Using the `care` command yields

$$\mathbf{P} = \begin{bmatrix} 23.553 & 0.022 \\ 0.022 & 0.005 \end{bmatrix}.$$

The optimal observer for the given specification is hence given as

$$\begin{aligned}\mathbf{L} &= (R^{-1}\mathbf{cP})^T = \mathbf{Pc}^T R^{-1}, \\ \mathbf{L} &= \begin{bmatrix} 23.553 & 0.022 \\ 0.022 & 0.005 \end{bmatrix} \begin{bmatrix} 1 & 0 \\ 0 & 1 \end{bmatrix} \frac{1}{1}, \\ \mathbf{L} &= \begin{bmatrix} 23.553 \\ 0.022 \end{bmatrix}.\end{aligned}$$

#### 4.1.3.2 Reduced Observer

For the series resonance circuit the output  $y = x_1$ , hence  $x_1$  is measurable and a reduced observer for  $x_2$  is designed according Section 3.2.3. The pole for the observer is specified as  $s_1 = -200$ .

The model of the series resonance circuit is already in the shape of (3.18). Since the system order  $n = 2$ , the reduced observer has order  $n - q = 1$  and the matrix  $\mathbf{L}$  and sub-matrices  $\mathbf{A}_{ij}$  are scalars. Therefore, the observer gain calculates as

$$\begin{aligned}(a_{22} - la_{12}) &\stackrel{!}{=} s_1, \\ l &= \frac{a_{22} - s_1}{a_{12}} = \frac{-91.75 - (-200)}{12658.2}, \\ l &= 0.0086,\end{aligned}\tag{4.5}$$

and the observer design is done. To retrieve the final observer, the individual components then simply need to be arranged as in (3.19).

#### 4.1.3.3 Super-Twisting Observer

The last designed observer is the super-twisting observer as described Section 3.2.4. The dynamics of the estimator for the series resonance circuit are given as

$$\begin{aligned}\frac{d}{dt} \begin{bmatrix} \hat{x}_1 \\ \hat{x}_2 \end{bmatrix} &= \mathbf{A}\hat{\mathbf{x}} + \mathbf{b}u - \begin{bmatrix} 1 \\ l \end{bmatrix} \left[ -k_1 \sqrt{|\tilde{x}_1|} \operatorname{sgn}(\tilde{x}_1) + w \right], \\ \frac{d}{dt} w &= -k_2 \operatorname{sgn}(\tilde{x}_1).\end{aligned}$$

In contrast to the general description, the state variable which is seen as system output is here in the upper row.

Hence, according to equation (3.22) and considering the change of rows,  $l$  must be chosen that  $(a_{22} - la_{12})$  is Hurwitz.

The pole of the reduced system is specified as  $s = -200$ , thus resulting

$$a_{22} - la_{12} \stackrel{!}{=} -200,$$

which equals the problem of the reduced observer in equation (4.5) and  $l = 0.0086$ .

The factor  $M$  is chosen as 5 to govern the observer error dynamics and therefore the remaining observer gains are given as

$$k_1 = 1.5\sqrt{M} = 1.5\sqrt{5} = 3.35,$$

$$k_2 = 1.1M = 1.1 \cdot 5 = 5.5.$$



## 4.2 Integrator Test Circuit

In this section different controllers are designed for the integrator test circuit from Section 2.4.2. The state-space model for the integrator, equation (2.27) reads as

$$\begin{aligned}x &= V_O, \quad u = u, \\ \frac{d}{dt}x &= \frac{1}{RC}u + \frac{1}{RC}\Delta(t), \\ y &= x.\end{aligned}$$

Since there is only one system state, which is also measurable at the output, no observer is designed for this circuit. Furthermore,  $\Delta(t)$  is considered as unknown input disturbance, hence, it is neglected for the normal controller design. Nevertheless it is considered to obtain a disturbance estimation using the 1-slide and super-twisting controller as well as assumptions about the disturbance are needed for the design of the controller with observer-based disturbance attenuation.

With the selected component values of  $R = 150k\Omega$  and  $C = 1\mu F$  from Section 2.4.2.2, the numerical dynamics of the integrator test circuit reads as

$$\frac{d}{dt}x = \frac{1}{0.15}u = 6.67u.$$

Obviously, as there is only one state which can be altered by the control signal, the circuit is controllable.

### 4.2.1 State Controller

The design of a state controller for the integrator is a rather simple problem. Since the integrator dynamics is solely driven by external inputs, the design task changes for the scalar case from  $(a-bk) = s_1$  to  $-bk = s_1$ . The pole is specified at  $s_1 = -100$ , thus, leading to a feedback gain

$$\begin{aligned}k &= -\frac{s_1}{b} = -\frac{-100}{6.67}, \\ k &= 15.\end{aligned}$$

The resulting scaling factor of the reference variable is therefore

$$\begin{aligned}V &= -\frac{1}{c(0-bk)^{-1}b} = \frac{cbk}{b} = ck, \\ V &= 15.\end{aligned}$$

Hence, the control law is given as

$$u = -kx + Vr = -15x + 15r.$$

### 4.2.2 1-sliding Controller

The design of the 1-sliding controller is straight forward as the control signal directly enters the state dynamics. Therefore, the sliding variable is chosen as

$$\sigma = e = (r - x),$$

and the control law follows as

$$\begin{aligned} \frac{d}{dt}\sigma &\stackrel{!}{=} -k \operatorname{sgn}(\sigma), \\ \frac{d}{dt}r - bu &= -k \operatorname{sgn}(\sigma), \\ u &= \frac{1}{b} \left( \frac{d}{dt}r + k \operatorname{sgn}(\sigma) \right). \end{aligned} \quad (4.6)$$

Considering the disturbance and using the derived control law the dynamics of  $\sigma$  is

$$\begin{aligned} \frac{d}{dt}\sigma &= \frac{d}{dt}r - b \left[ \frac{1}{b} \left( \frac{d}{dt}r + k \operatorname{sgn}(\sigma) \right) + \Delta(t) \right], \\ \frac{d}{dt}\sigma &= -k \operatorname{sgn}(\sigma) - b\Delta(t). \end{aligned}$$

To drive the sliding variable and hence the control error to zero ( $\sigma = e = 0$ ), the gain must be chosen as

$$k > b\Delta_{max}, \quad \Delta_{max} = \max_t (|\Delta(t)|).$$

By assuming  $\Delta_{max} < 1$  a choice of  $k = 6.67$  ensures this. Therefore, when reaching the sliding mode ( $\sigma = \frac{d}{dt}\sigma = 0$ ) the dynamics change to

$$\begin{aligned} 0 &= -k \operatorname{sgn}(0) - b\Delta(t), \\ \Delta(t) &= -\frac{k}{6.67} \operatorname{sgn}(0). \end{aligned}$$

In theory this requires infinite fast switching of the control signal to maintain the sliding mode. However, in real systems the sliding mode is maintained by fast switching actions that keep the sliding variable in a vicinity around zero  $|\sigma| < \epsilon$ . Moreover, the disturbance can be estimated in the sliding mode by using a low-pass filter

$$\hat{\Delta}(t) = LPF \left[ -\frac{k}{6.67} \operatorname{sgn}(\sigma) \right].$$

However, the estimate is influenced by the LPF characteristics, i.e. the time constant of the implemented LPF.

### 4.2.3 Super-Twisting Controller

The sliding variable for the super-twisting controller is chosen as for the previous 1-sliding controller

$$\sigma = e = (r - x).$$

Using the super-twisting algorithm from (3.12) and the previously obtained control law from the 1-sliding controller (4.6), the control law of the super-twisting controller can directly be formulated as

$$u = \frac{1}{b} \left( \frac{d}{dt}r + k_1 \sqrt{|\sigma|} \operatorname{sgn}(\sigma) - w \right),$$

$$\frac{d}{dt}w = -k_2 \operatorname{sgn}(\sigma).$$

By choosing

$$k_1 = 1.5\sqrt{Mb},$$

$$k_2 = 1.1Mb,$$

where  $M$  is the Lipschitz constant of the perturbation

$$M = \max_t \left( \left| \frac{d}{dt}\Delta(t) \right| \right),$$

the sliding mode is obtained in finite time. For the test measurements  $M = 2.5$  is chosen to govern the dynamics. With the disturbance considered, the error dynamics change to

$$\frac{d}{dt}\sigma = \frac{d}{dt}r - b \left[ \frac{1}{b} \left( \frac{d}{dt}r + k_1 \sqrt{|\sigma|} \operatorname{sgn}(\sigma) - w \right) + \Delta(t) \right],$$

$$\frac{d}{dt}\sigma = -k_1 \sqrt{|\sigma|} \operatorname{sgn}(\sigma) + w - b\Delta(t).$$

When the system is in the sliding mode ( $\sigma = \frac{d}{dt}\sigma = 0$ ), the disturbance can be estimated as

$$0 = -k_1 \sqrt{|0|} \operatorname{sgn}(0) + w - b\Delta(t),$$

$$\hat{\Delta}(t) = \frac{w}{b} = \frac{w}{6.67}.$$

In contrast to the previously obtained disturbance estimate of the 1-sliding controller, there is no impairment of the estimate due to the LPF. Therefore, the super-twisting controller yields a better disturbance estimate.

#### 4.2.4 OBDA Controller

The design of this controller with observer-based disturbance attenuation is done as described in Section 3.3.2. At first the state controller and observer are designed independently according to the separation theorem in Section 3.3.1.

Therefore, the controller can be obtained exactly as previously in Section 4.2.1. The pole for the controller is specified as  $s_c = -30$  hence resulting  $k = V = 4.5$ . The resulting control law reads

$$u = -4.5x + 4.5r.$$

Next, the Luenberger observer is designed, with the observer pole specified as  $s_o = -30$ . Since the dynamics are independent of the state the design problem for the scalar case changes from  $(a - lc) = s_o$  to  $-lc = s_o$ . Since  $c = 1$ , the observer gain matches the specified pole with reversed sign  $l = -s_o = 30$ . Hence, the resulting Luenberger observer is given as

$$\hat{x} = 6.67u + 30(x - \hat{x}).$$

The ideal Q-function can be obtained using equation (3.24) as follows

$$\begin{aligned} Q(s) &= -\frac{1 + k(s + lc)^{-1}b}{c(s + lc)^{-1}b} \\ Q(s) &= -\frac{1 + 4.5 \cdot (s + 30 \cdot 1)^{-1} \cdot 6.67}{1 \cdot (s + 30 \cdot 1)^{-1} \cdot 6.67} \\ Q(s) &= -\frac{(s + 30) + 4.5 \cdot 6.67}{6.67} \\ Q(s) &= -9 - 0.15s \end{aligned}$$

As can be seen, the function is not proper. However, the goal is to approximate this function for specified frequencies. Therefore, the disturbance is assumed to consist of a frequency-dependent part and a constant part

$$w = A \sin(\omega_{w,1}t + \phi_w) + B,$$

with specified frequency  $\omega_{w,1} = 2\pi \cdot 0.6 \text{rad/s} = 3.77 \text{rad/s}$ .

Hence, there is only one frequency not equal to  $\omega_{w,0} = 0$ , thus  $\kappa = 1$ . According to equation (3.25)  $Q(s)$  can therefore be approximated by

$$\bar{Q}(s) = \frac{b_2 s^2 + b_1 s + b_0}{(s + \lambda)^2},$$

with  $\lambda = 1$  chosen.

The ideal Q-function  $Q(s)$  is then evaluated at given frequencies  $\omega_{w,0} = 0\text{rad/s}$  and  $\omega_{w,1} = 3.77\text{rad/s}$

$$\begin{aligned} Q(j \cdot 0) &= M_0 = -9, \\ Q(j \cdot 3.77) &= M_{1,R} + jM_{1,I} = -9 + j(-0.5655). \end{aligned}$$

The results are then equated with the approximated Q-function  $\bar{Q}(s)$

$$\begin{aligned} \bar{Q}(j \cdot 0) &\stackrel{!}{=} Q(j \cdot 0) = M_0 \\ \bar{Q}(j \cdot 3.77) &\stackrel{!}{=} Q(j \cdot 3.77) = M_{1,R} + jM_{1,I}. \end{aligned}$$

A comparison of coefficients leads to the following numerator coefficients of the approximation

$$\begin{aligned} b_0 &= \lambda^2 M_0, \\ b_1 &= \frac{M_{1,I}}{\omega_{w,1}} (\lambda^2 - \omega_{w,1}^2) + 2\lambda M_{1,R} \\ b_2 &= \frac{\lambda^2}{\omega_{w,1}^2} M_0 - \frac{M_{1,R}}{\omega_{w,1}^2} (\lambda^2 - \omega_{w,1}^2) + 2\lambda \frac{M_{1,I}}{\omega_{w,1}}. \end{aligned}$$

With the coefficients calculated, the approximated Q-function is given as

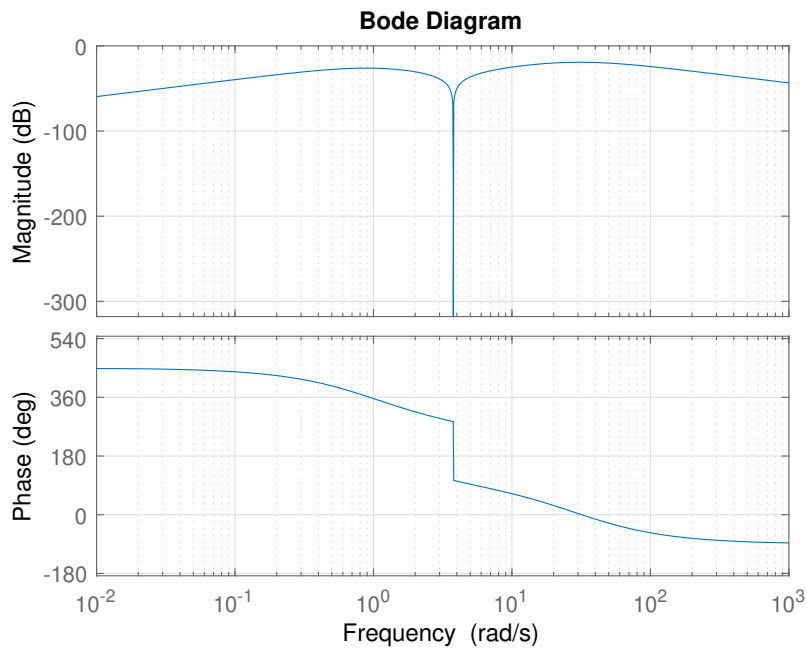
$$\bar{Q}(s) = \frac{-9.3s^2 - 16.02s - 9}{s^2 + 2s + 1}.$$

Figure 4.9 shows a comparison of bode plots for the transfer function  $G_{yw}$  from the disturbance  $w$  to the output  $y$ . On the top, Figure 4.9a shows the transfer function  $G_{yw,Q}$  for the OBDA controller with disturbance attenuation using the control law  $u = -k\hat{x} + Vr + \bar{Q}(s)\tilde{y}(s)$ . Figure 4.9b below shows the transfer function  $G_{yw,noQ}$  for a normal observer-based state controller with the control law  $u = -k\hat{x} + Vr$ . As can be seen, the designed OBDA controller utilising the Q-function strongly attenuates the specified frequencies, especially seen for  $\omega_{w,1} = 3.77\text{rad/s}$ . Furthermore, also the general disturbance rejection is much better.

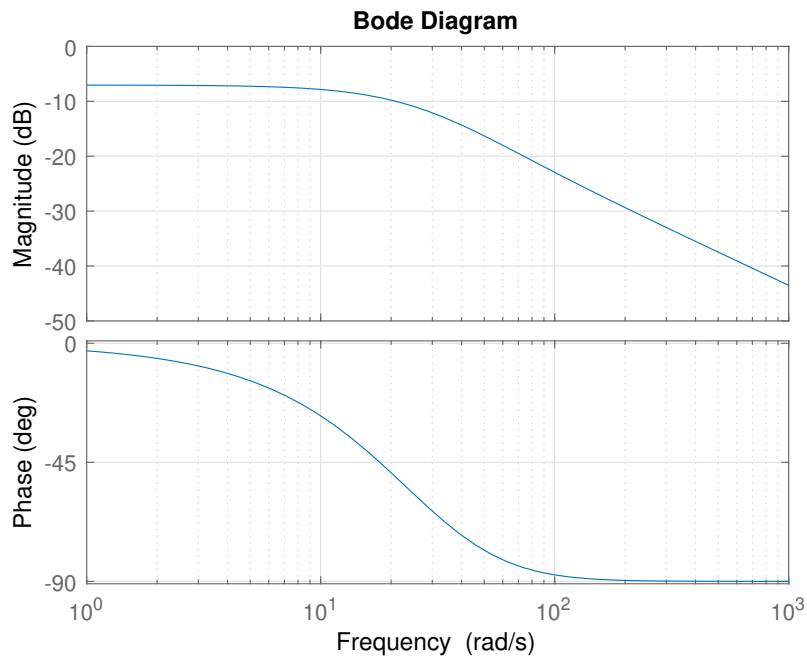
The evaluation of the transfer function of the designed OBDA controller at the specified frequencies yields

$$G_{yw,Q}(j \cdot 0) = 0 \quad \text{and} \quad G_{yw,Q}(j \cdot 3.77) = -6.798\text{e-}17 - j9.826\text{e-}18.$$

The disadvantage of this approach is that the degree of  $\bar{Q}(s)$  increases by 2 for each specified frequency not equal to zero, hence obtaining high order controller when specifying several frequencies.



(a) Control approach with disturbance attenuation  $u = -k\hat{x} + Vr + \bar{Q}(s)\tilde{y}(s)$ .



(b) Conventional controller approach without disturbance attenuation  $u = -k\hat{x} + Vr$ .

Figure 4.9: Bode plot of the transfer functions  $G_{yw}$  from the disturbance  $w$  to the system output  $y$ . Plot (a) shows the just designed OBDA controller that strongly attenuates the disturbances at the specified frequencies utilising  $\bar{Q}(s)$ . Plot (b) shows a conventional observer-based state controller without disturbance attenuation.

# 5 Experimental Results

The designed controllers and observers from the previous chapter are tested with the laboratory set-up where different control scenarios are considered. First, the experiments with the series resonance circuit are presented covering reference tracking, state estimation and observer-based control. Subsequently the experiments with the integrator circuit take care of circuits with input disturbance and show how the designed controllers perform.

Although exact modelling of the circuits was done, there are uncertainties due to the tolerance of the used components and simplifications. Moreover, measurement noise and signal distortions within the measurement process of the hardware set-up further influence the results.

For the differentiation of the reference signals during the experiments, the *robust exact differentiators* toolbox from [22] is used in MATLAB Simulink. The parameter setting for the toolbox was order  $n = 1$ , tuning parameter  $c = 100$  and the discretisation time  $t_d = 0.001s$  inherited from the ADC sampling of the measurements. Furthermore, despite working with discrete measurements the plants are considered continuous in the simulation.

## 5.1 Series Resonance Circuit

With the series resonance test circuit five different test were carried out the laboratory set-up

1. reference tracking with the different controllers
  - a. tracking a rectangular signal with  $1V$  amplitude and  $0.5s$  width and
  - b. tracking a sine input  $r = 2 \sin(2\pi \cdot 5Hz \cdot t)$ ,
2. using the observers for state estimation,
3. control based on the observed state,
4. change of system parameters and finally

5. reference tracking when considering the current as system output.

The experiments were performed with the test circuit set to  $C = C_{max}$ . The controller and observer parameters for the experiments are the same as from Section 4.1. As state controller the LQR design is used and for the LS controller design approach B. Only the parameters for the PID controller were changed from the obtained starting values using Ziegler-Nichols ultimate gain method to the used parameter  $k_p = 0.8$ ,  $k_i = 36.36$  and  $k_d = 0.0021$ . If other parameters were used, they are stated explicitly.

### 5.1.1 Experiment 1

First, Figure 5.1 shows the results for experiment 1a, reference tracking of a rectangular input signal. As can be seen, the uncontrolled system has the highest overshooting whereas the PID controlled system slowly approaches the step change. In contrast to the 1-sliding system where chattering can be seen, the super-twisting controlled system has a smoother output. This can also be seen in the control signal as shown in Figure 5.2a.

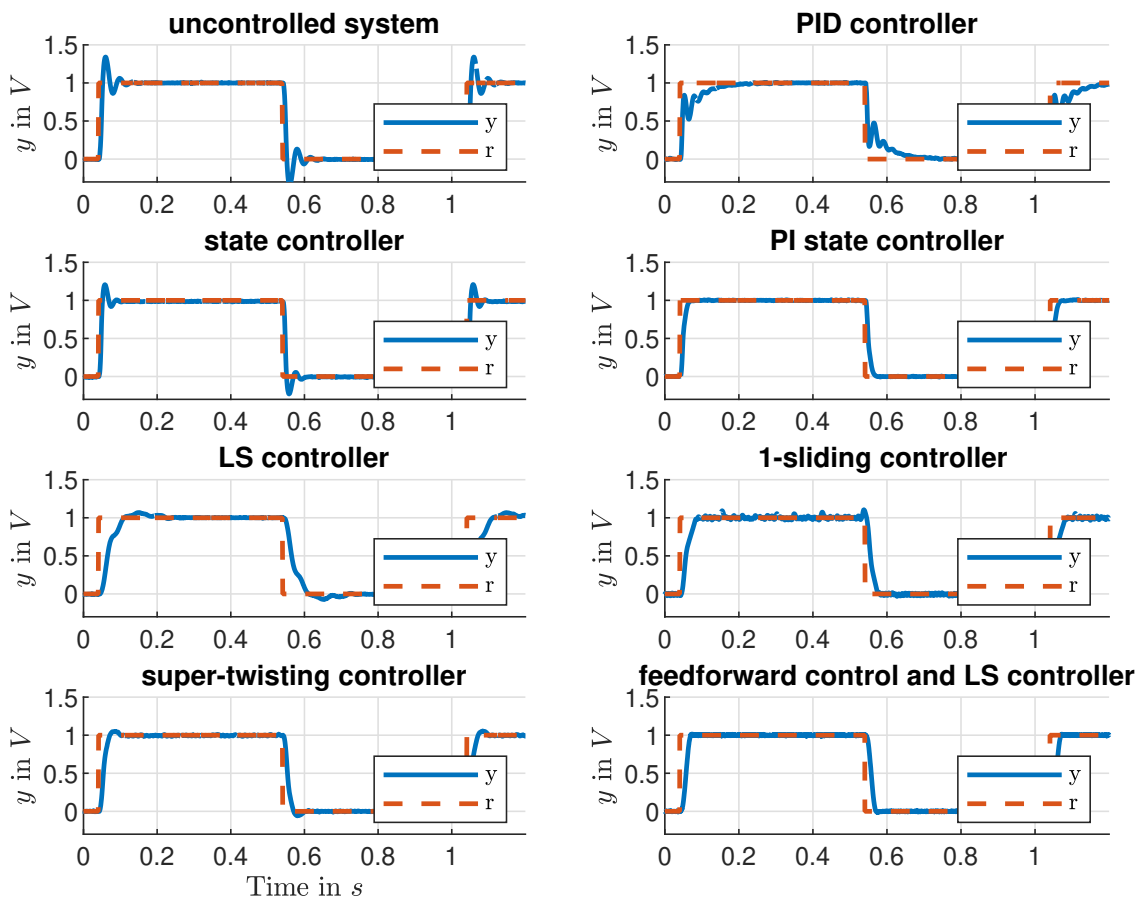
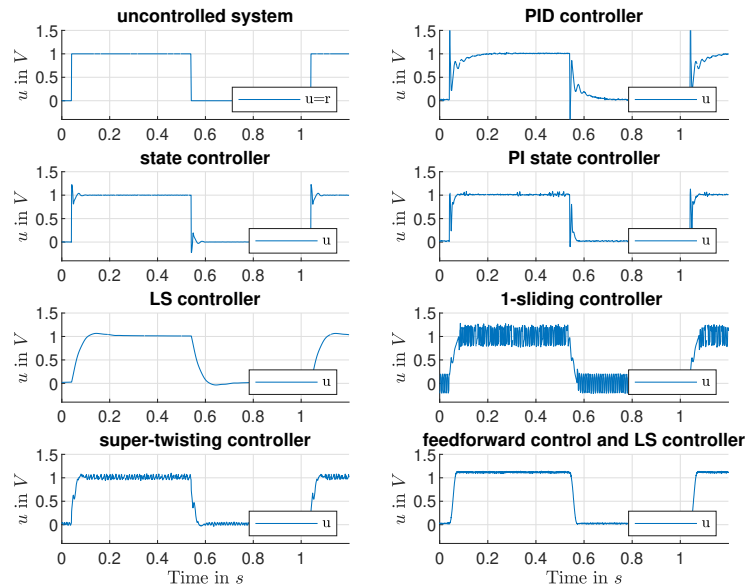
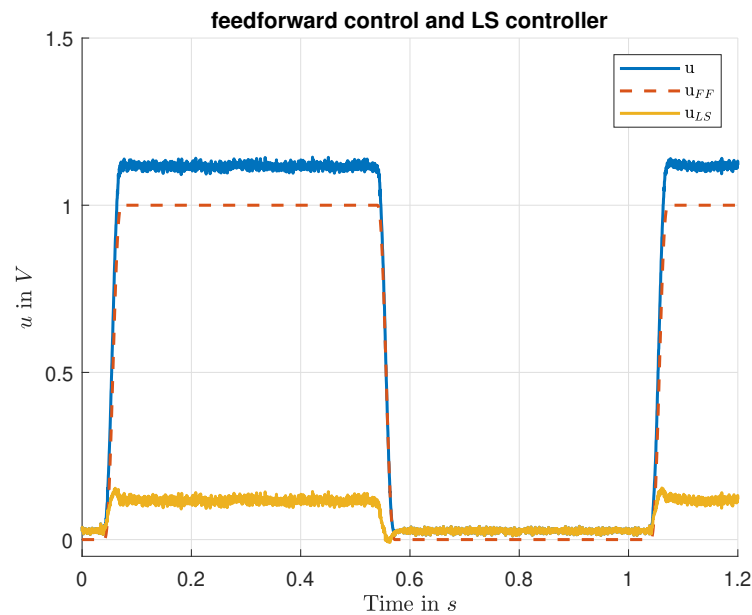


Figure 5.1: Results experiment 1a: Reference tracking of a rectangular signal.





(a) Control signals for reference tracking.



(b) Control signal composition of the feedforward and LS controlled system.

Figure 5.2: Results experiment 1a: Control signals.

From the control signals it can also be seen, that control signals of all controllers except the PID controller stay within the hardware boundary of approximately  $\pm 2.5V$ . However, the PID controller violates this only very short when the derivative term is high.

The system with feedforward and LS control, bottom right, generates a very smooth transit between the two operation points. Figure 5.2b shows how the control signal is composed. As can be seen, the major part is the feedforward control  $u_{FF}$  based on the planned trajectory. Ideally, the control signal  $u_{LS}$  of the LS controller is zero,

however, as there are model uncertainties and measurement noise the controller acts to compensate them.

Figure 5.3 shows the results for experiment 1b with the changed controller parameters for this experiment stated in Table 5.1. As can be seen in Figure 5.3, all controllers with integrating behaviour (PID, PI state, LS) increase the phase lag compared to the uncontrolled system. The state controller yields slightly better performance than the uncontrolled system whereas the 1-sliding and the super-twisting controller are practically able to replicate the reference variable.

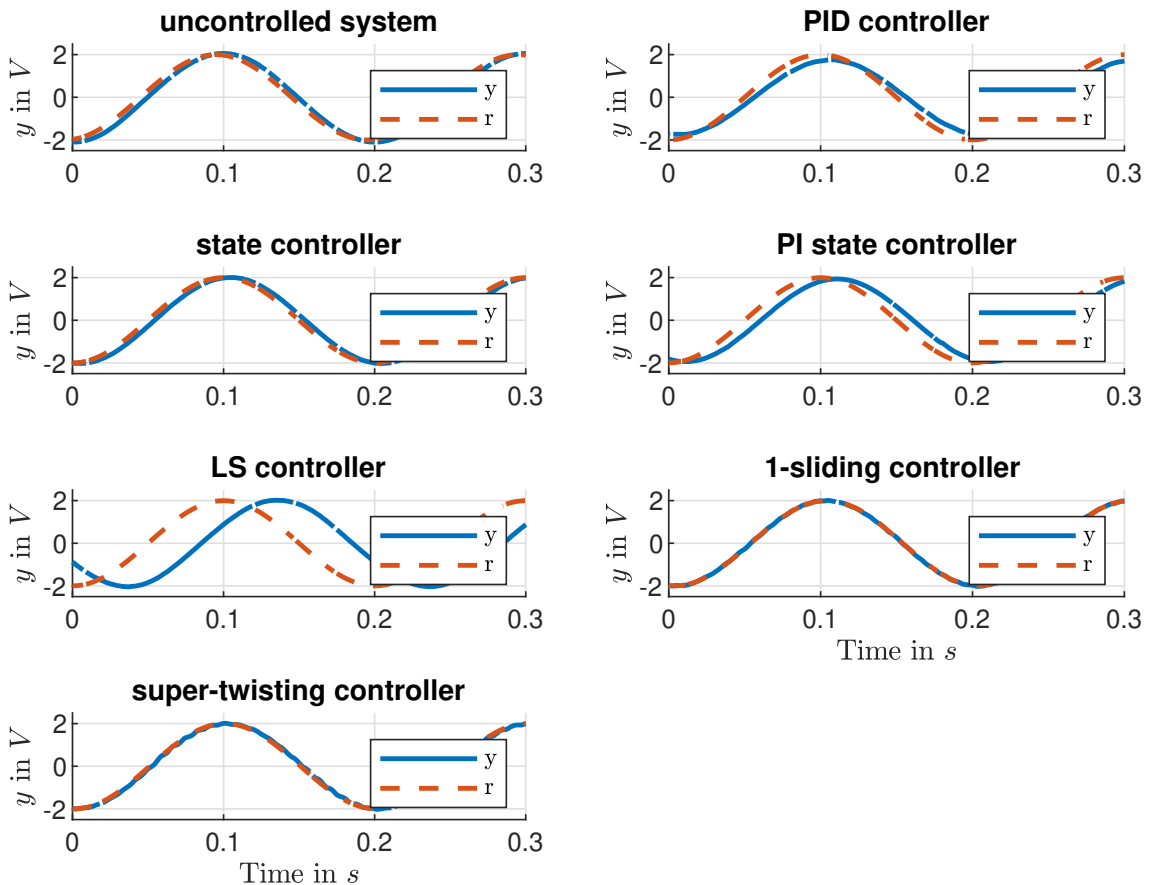


Figure 5.3: Results experiment 1b: Reference tracking of a sine signal.

controller	parameter
state	$R = 1$
PI state	$s_1 = s_2 = s_3 = -200$

Table 5.1: Changed controller parameters series resonance circuit experiment 1b and 3.

### 5.1.2 Experiment 2

Experiment 2 examines the different implemented observers on the uncontrolled system. As Figure 5.4 shows, all three observers are generally able to replicate the system state. A more detailed view is given in Figure 5.5.

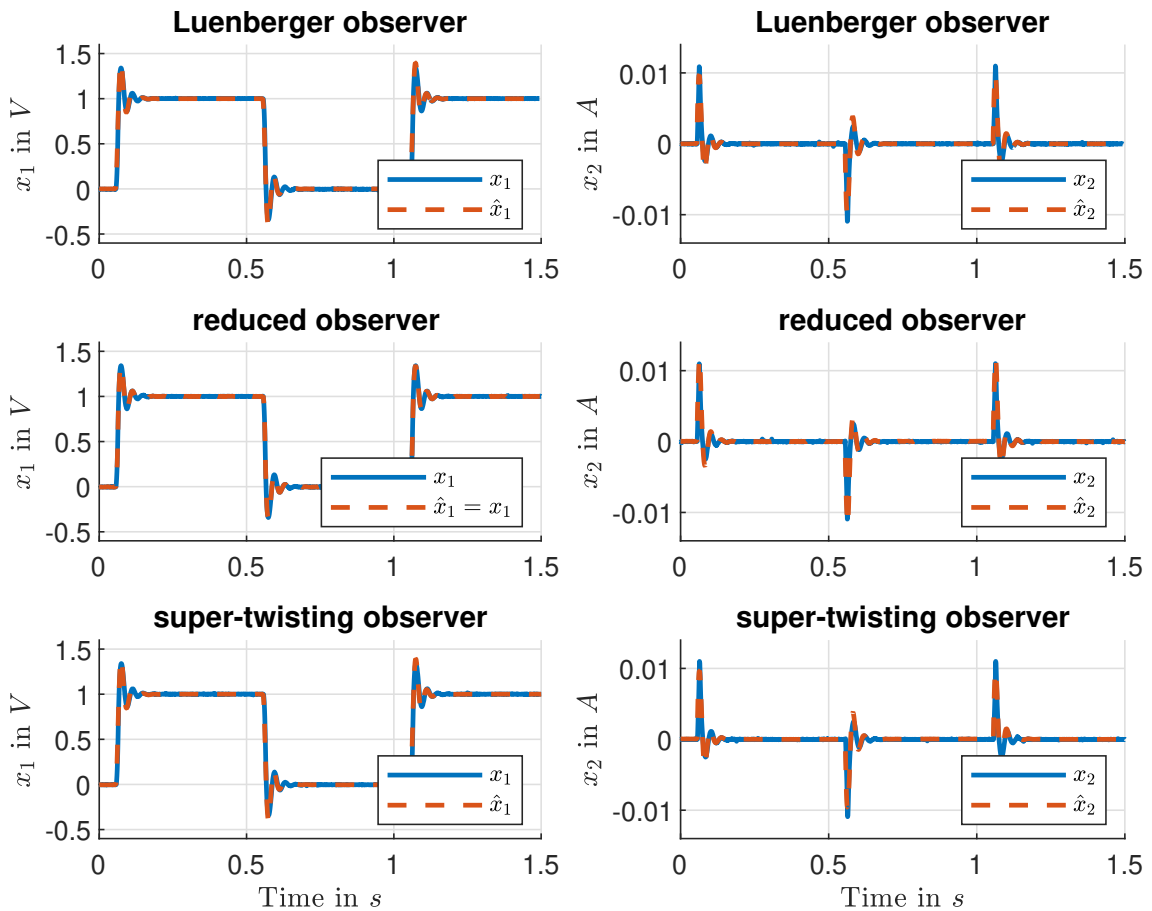


Figure 5.4: Results experiment 2: State estimation with observers.

As can be seen, the Luenberger and the super-twisting observer yield for the given setting similar results. For the reduced observer the system output is not observed, hence  $\hat{x}_1 = x_1 = y$ . Although the state observers contain an exact copy of the system model, the dynamics initiated by the step input differ slightly. However, the estimation error for all observers vanishes asymptotically and the difference in dynamics can be explained by model uncertainties respectively component tolerances of the series resonance circuit.

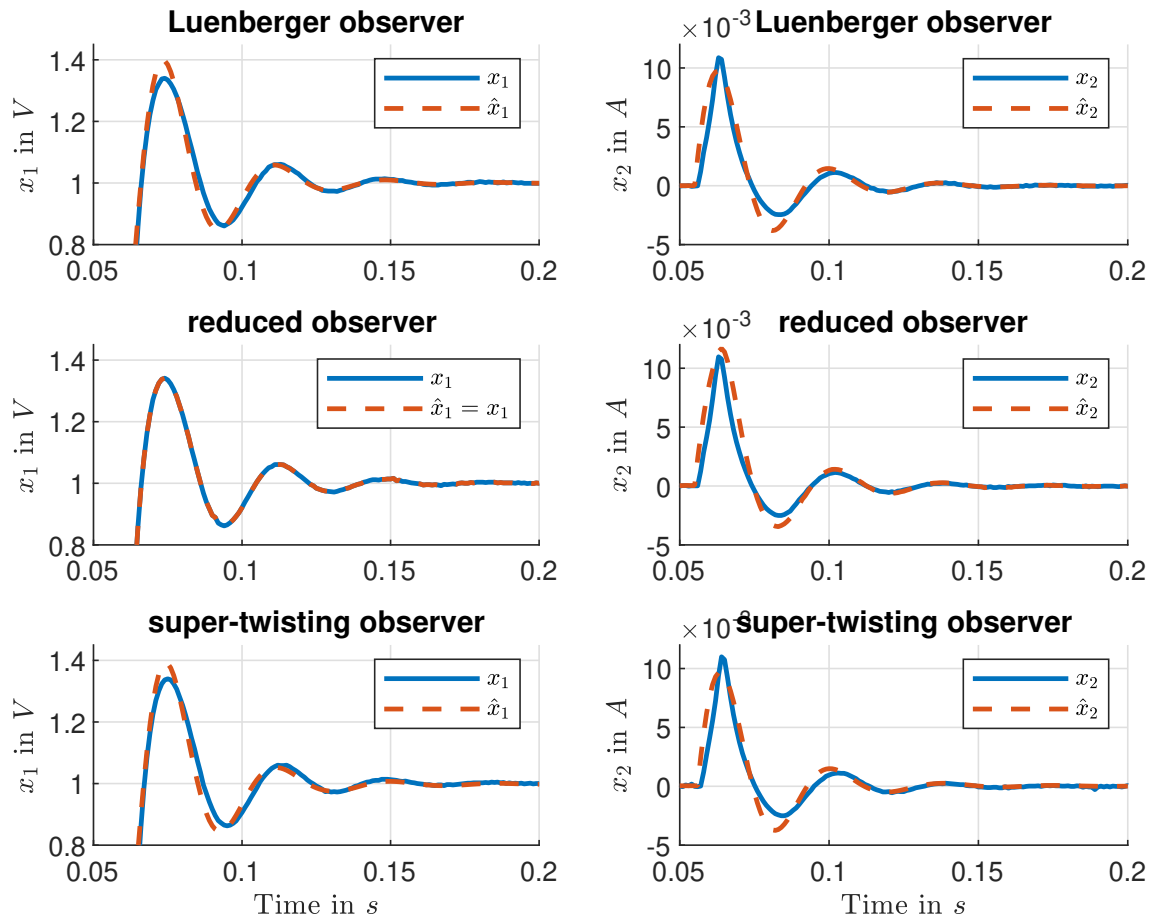


Figure 5.5: Results experiment 2: State estimation with observers in detail.

### 5.1.3 Experiment 3

With a Luenberger observer used to estimate the state, experiment 3 examines reference tracking with observer-based control. As the PID and LS controller do not rely on the system state, they are not considered within this experiment. The state controller and PI state controller are again used with the parameter setting of Table 5.1.

Figure 5.6 shows the results for the remaining four controllers. As can be seen, the reference tracking of the rectangular input signal works. Nevertheless, the output of all systems contains a slight oscillation which might be introduced due to the observation error.

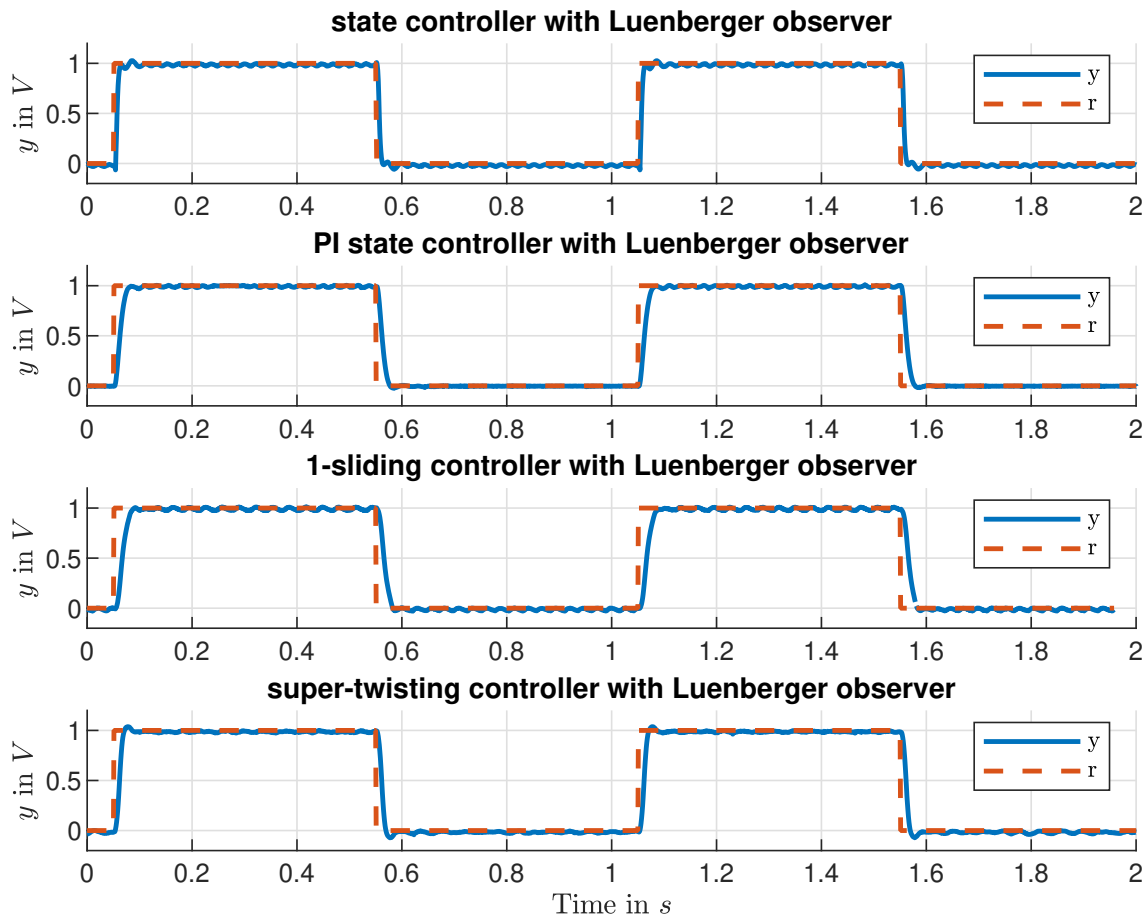


Figure 5.6: Results experiment 3: Reference tracking with observer-based control.

#### 5.1.4 Experiment 4

Experiment 4 highlights the impact of changed system dynamics that are not considered in the model and thus can be seen as uncertainty. Therefore, the capacitance of the system is changed by switching off the biggest capacitor. Hence, the capacitance is changed from  $C = C_{max} = 79\mu F$  to  $C = 32\mu F$ .

For this experiment the state controller is using the measured system state again. Figure 5.7 shows the results when using the state controller, with parameter  $R = 1$  shown top and  $R = 10$  in the middle ( $\mathbf{Q}$  as before). The uncontrolled system shown at the bottom has a higher overshooting due to the changed system dynamics.

The previously controller with  $R = 1$  now acts too strong as the smaller capacitance needs less current to charge. Therefore, the control signal is weighted stronger in the LQR cost function by setting  $R = 10$ . Figure 5.8 shows the corresponding control signals. As can be seen the control signal for the LQR with  $R = 1$  is much higher as for the LQR with  $R = 10$ .

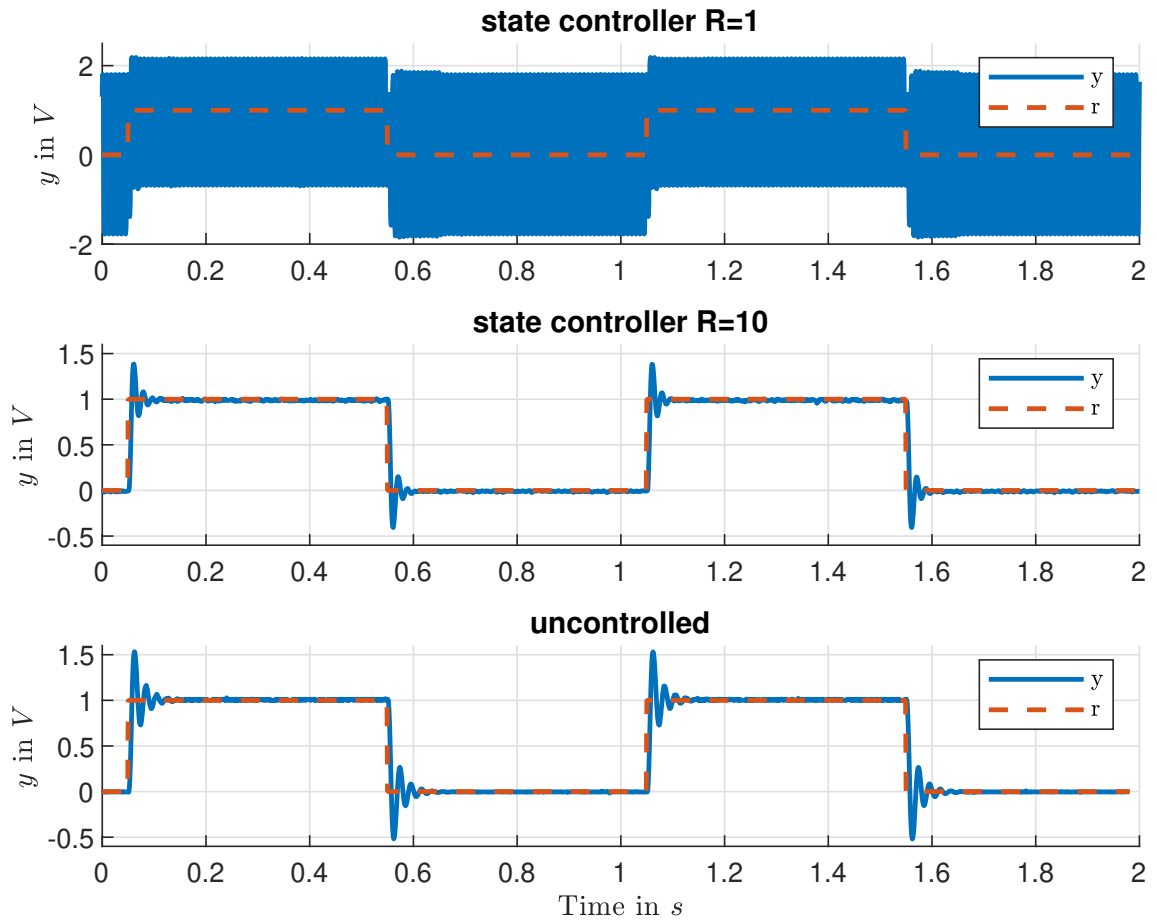


Figure 5.7: Results experiment 4: Reference tracking with changed system dynamics.

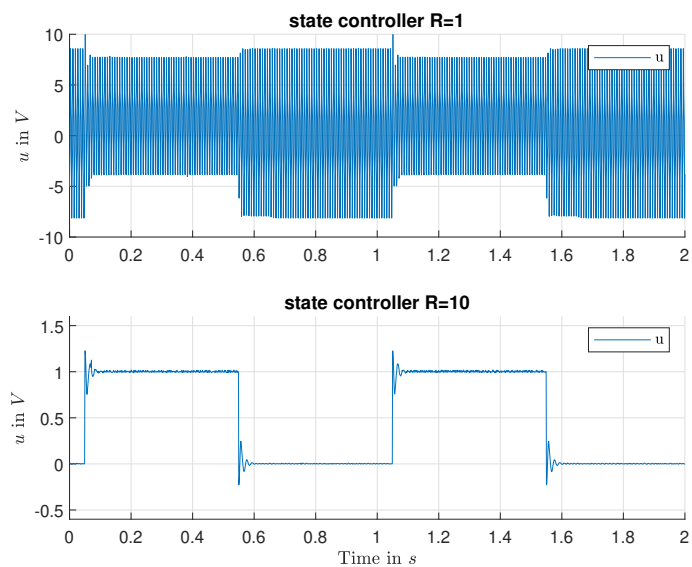


Figure 5.8: Results experiment 4: Control signal for reference tracking with changed system dynamics.

### 5.1.5 Experiment 5

For experiment 5, the current is considered as system output of the series reference circuit. Figure 5.9 shows the results for an input  $r = 0.001 \sin(2\pi \cdot 2Hz)$ . The super-twisting controller is able to replicate the reference input, whereas the state controlled system is only able to match the amplitude but not the phase.

However, during the test it was only possible to drive the super-twisting system correctly for a few seconds. This was due to the fact that the controlled signals are very small ( $0.001A \cdot 5\Omega = 0.005V$ ) and a slight error in the measurement, probably a zero offset, caused the super-twisting controller to saturate. Figure 5.10 show the associated control signals with the super-twisting control signal showing a drift that leads to saturation.

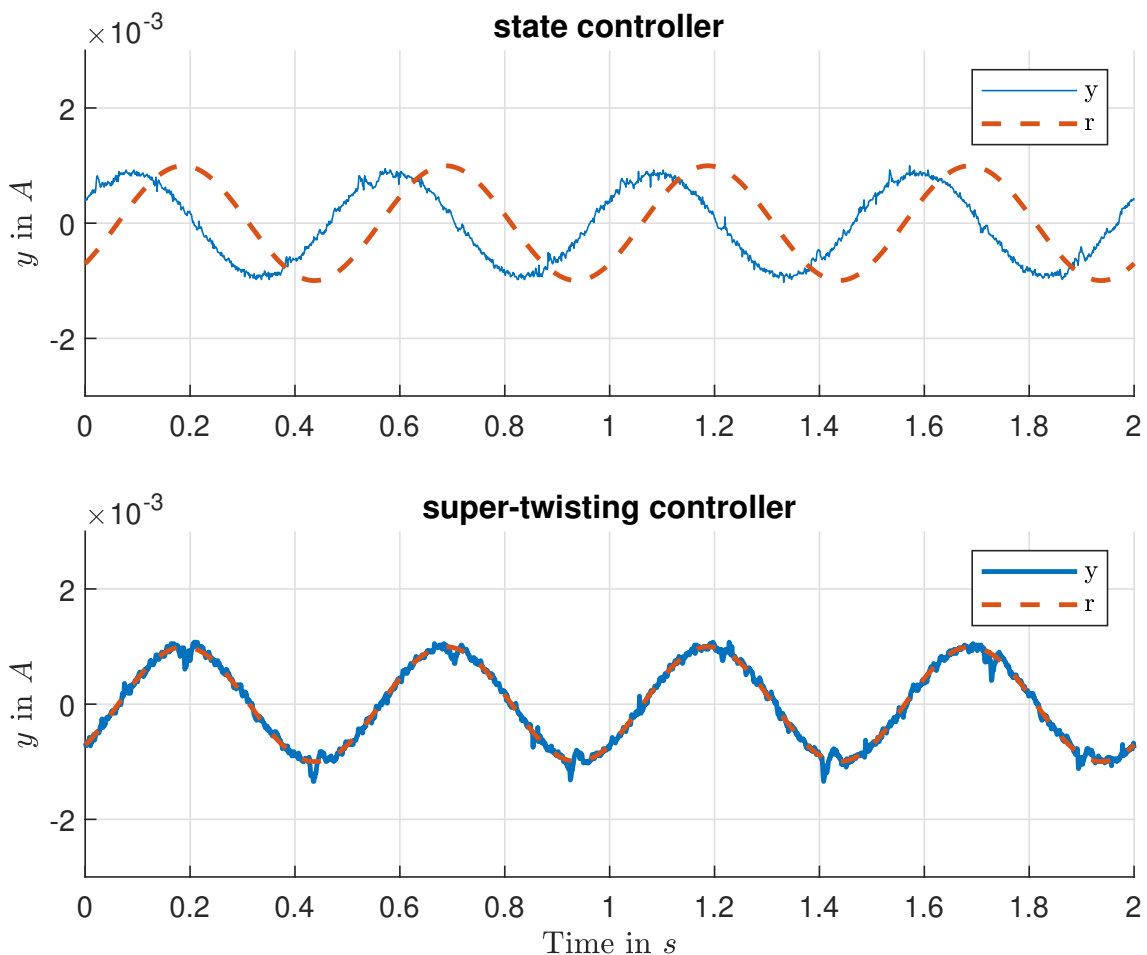


Figure 5.9: Results experiment 5: Reference tracking considering the current as output.

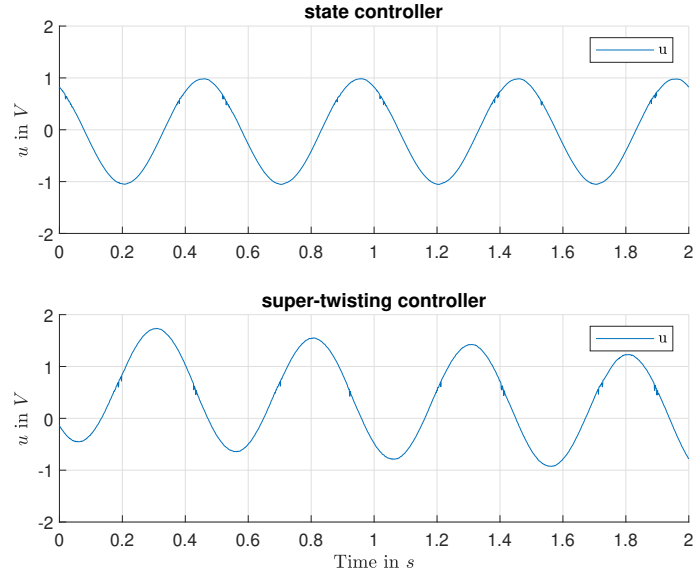


Figure 5.10: Results experiment 5: Control signals for reference tracking considering the current as output.

## 5.2 Integrator

In the previous section the test with the series resonance test circuit showed reference tracking and state estimation. This section now shows how the designed controllers for the integrator test circuit tackle input disturbances. Therefore, three different experiments were performed with the laboratory set-up

6. disturbance attenuation with  $r = 0$  and constant input disturbance  $\Delta = 0.3$ ,
7. disturbance attenuation with  $r = 0$  and sinusoidal input disturbance
  - a.  $\Delta = 0.6 \sin(2\pi \cdot 0.6Hz \cdot t)$  and
  - b.  $\Delta = 0.6 \sin(2\pi \cdot 2Hz \cdot t)$ ,
8. reference tracking  $r = 0.2 \sin(2\pi \cdot 1Hz \cdot t)$  and sinusoidal input disturbance  $\Delta = 0.6 \sin(2\pi \cdot 0.6Hz \cdot t)$ .

For the first two experiments (6 and 7) the same parameters as from the controller design Section 4.2 are used. For the additional reference tracking in experiment 8 the controllers are made "faster", with the altered parameters shown in Table 5.2.

controller	parameter
state	$s = -300$
OBDA	$s_c = s_o = -150$
super-twisting	$M = 6$

Table 5.2: Changed controller parameters for experiment 8.



### 5.2.1 Experiment 6

For this experiment a constant input of  $\Delta = 0.3$  is assumed. Figure 5.11 shows the integrator outputs. The OBDA controller is able to attenuate the disturbance whereas the state controller is not. The 1-sliding and super-twisting controller are also able to suppress the perturbation, however, the chattering for the 1-sliding controller is clearly seen. By reducing the gain of the 1-sliding controller the chattering can be reduced, however the gain must still dominate the disturbance.

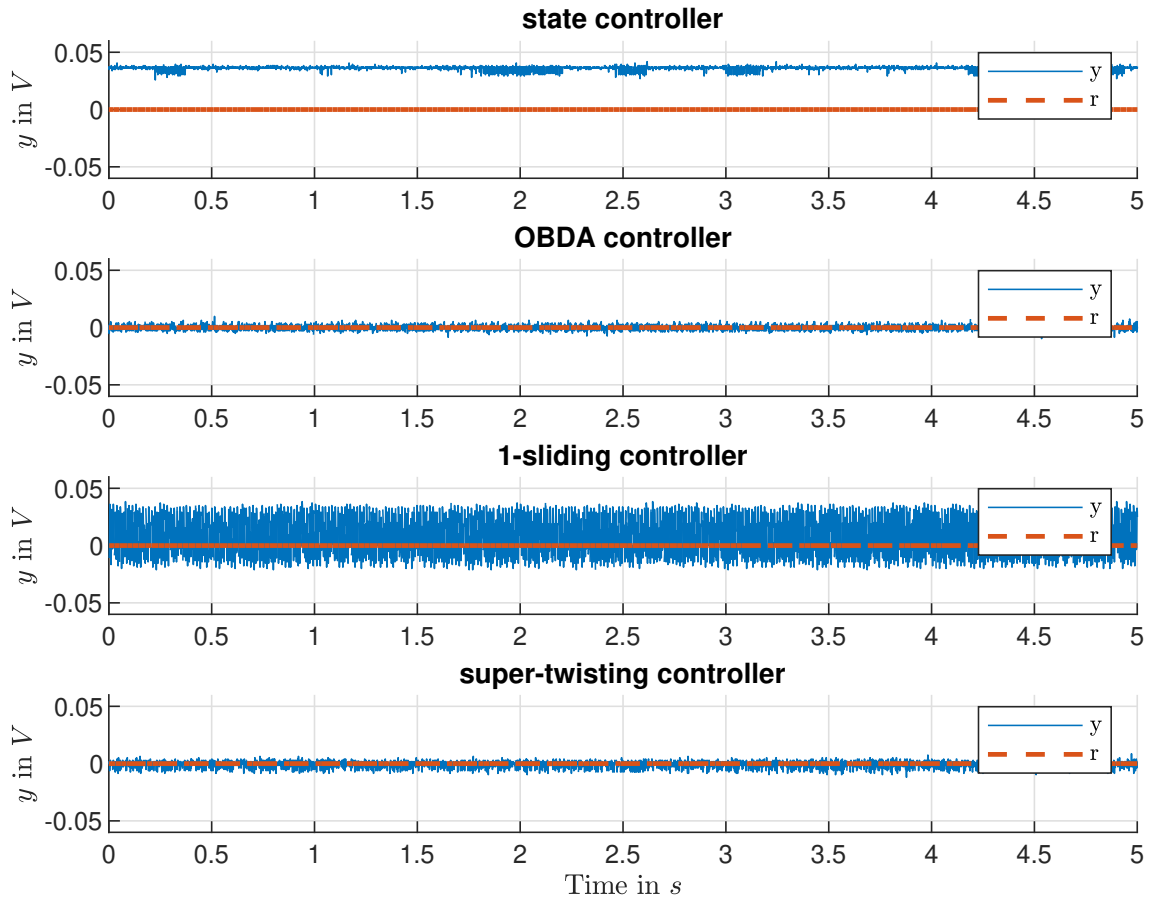
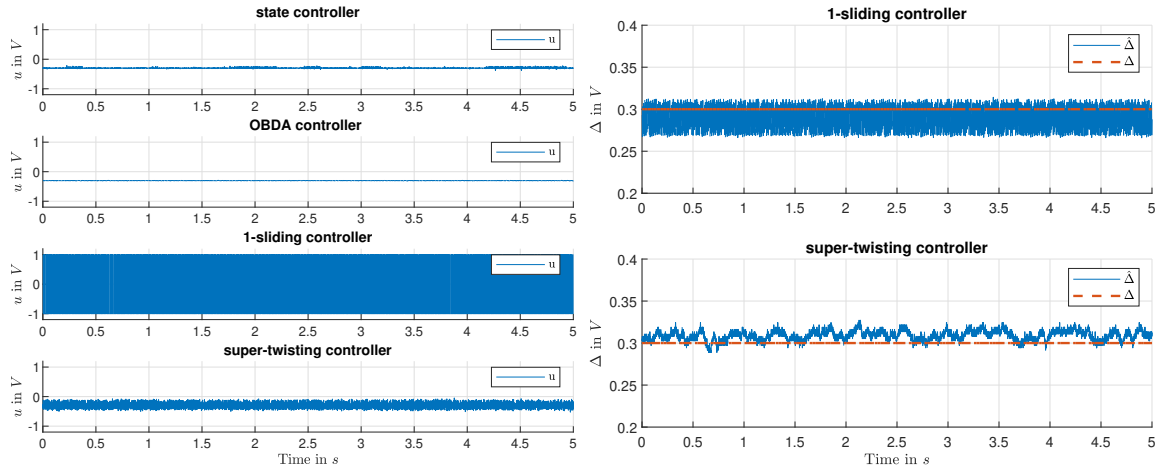


Figure 5.11: Results experiment 6: Attenuation of a constant disturbance.

The control signals are shown in Figure 5.12a, with the 1-sliding controller constantly changing between  $-1$  and  $1$ . The two sliding mode controllers furthermore allow to estimate of the disturbance as shown in Figure 5.12b, with both methods yielding a viable estimate. For the 1-sliding controller an extra LPF is needed with the used transfer function given as

$$LPF(s) = \frac{1}{0.1s + 1}.$$



(a) Control signal for attenuation of a constant disturbance. (b) Estimation of a constant disturbance.

Figure 5.12: Results experiment 6, control signal and disturbance estimation.

## 5.2.2 Experiment 7

The second experiment exploits the attenuation of a sinusoidal disturbance. At first in experiment 7a, the frequency is exactly the one used for the design of the OBDA controller  $\Delta = 0.6 \sin(2\pi \cdot 0.6Hz \cdot t)$ . For the second experiment 7b, the frequency is changed to  $\Delta = 0.6 \sin(2\pi \cdot 2Hz \cdot t)$ .

Figure 5.13 shows the results for the attenuation of experiment 7a. Although the pole of the OBDA controller is about 3 times "slower" than the state controller, the OBDA controller yields the better performance.

When looking at the Figure 5.14a it can be seen that the form of the control signals from the OBDA controller and state controller are similar, however, there is a phase shift introduced by the Q-function of the OBDA controller.

Both sliding mode approaches are able to keep the control error within a vicinity around zero and hence again allow to estimate the disturbance as shown in Figure 5.14b. This time however, the super-twisting controller yields a much better estimate as the required LPF affects the estimation of the 1-sliding controller.

Figure 5.15 shows the results of the state controller and OBDA controller for experiment 7b. As the frequency of the disturbance is not the specified frequency for the OBDA design, the performance decreases to the level of the state controller. However, it needs to be mentioned again that the pole of the OBDA controller is much "slower" compared to the state controller ( $-30$  to  $-100$ ).

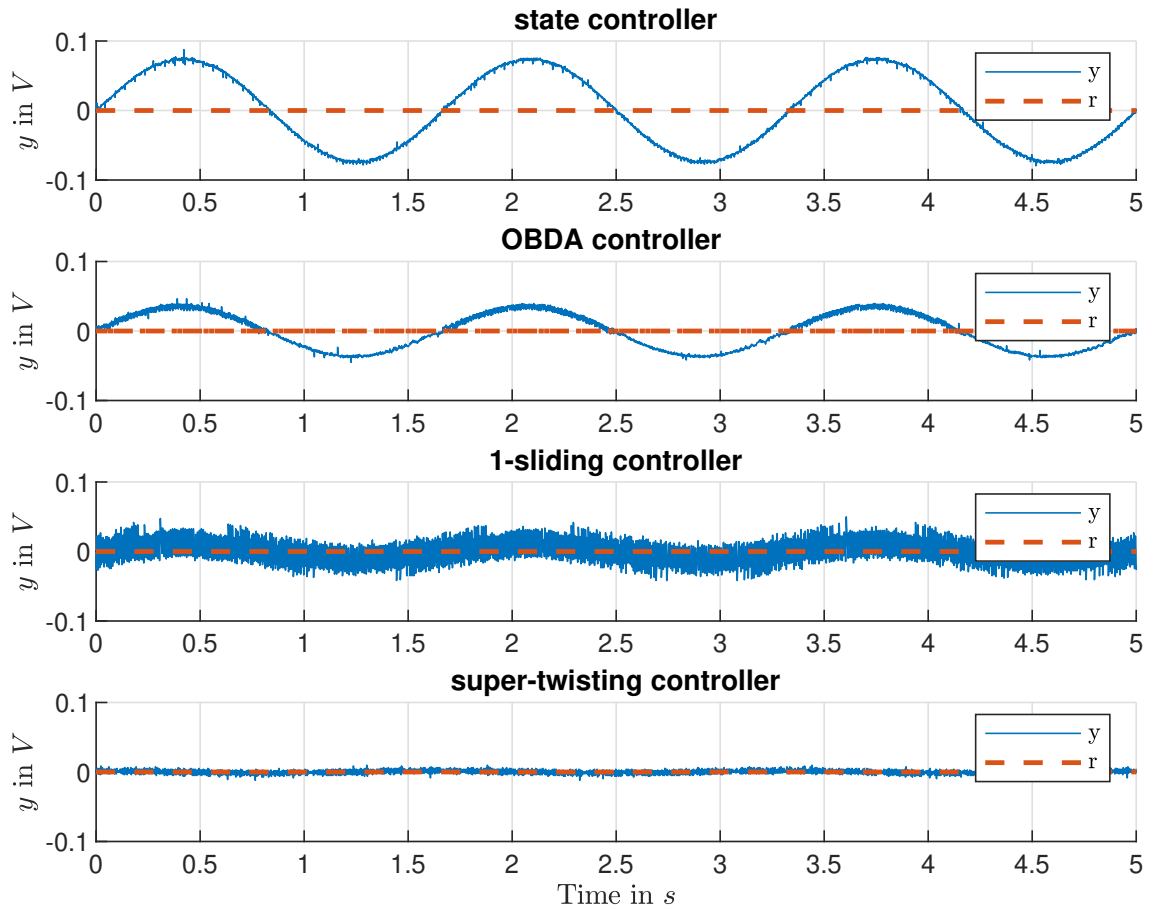
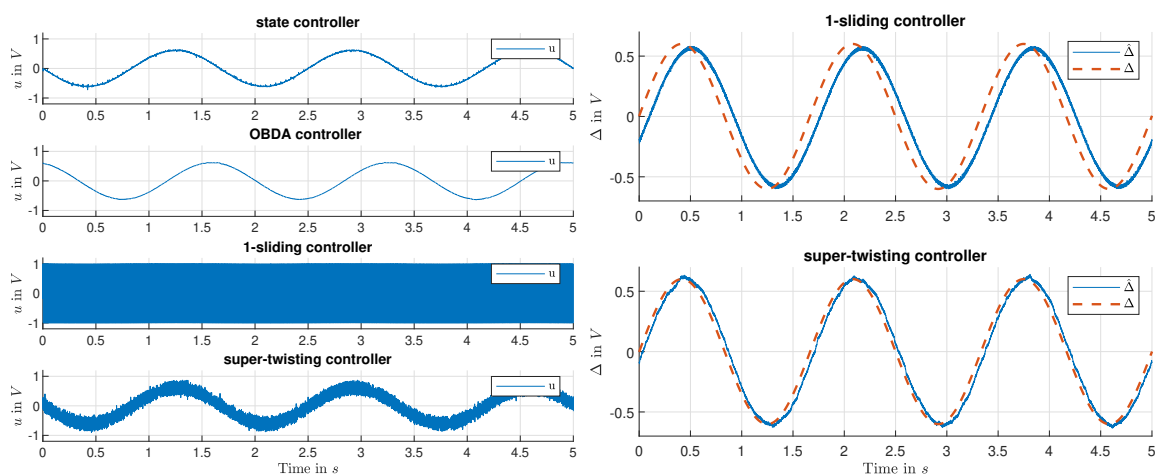


Figure 5.13: Results experiment 7a: Attenuation of a sinusoidal disturbance  $\Delta = 0.6 \sin(2\pi \cdot 0.6Hz \cdot t)$ .



(a) Control signal for attenuation of a sinusoidal disturbance. (b) Estimation of a sinusoidal disturbance.

Figure 5.14: Results experiment 7a, control signal and disturbance estimation.

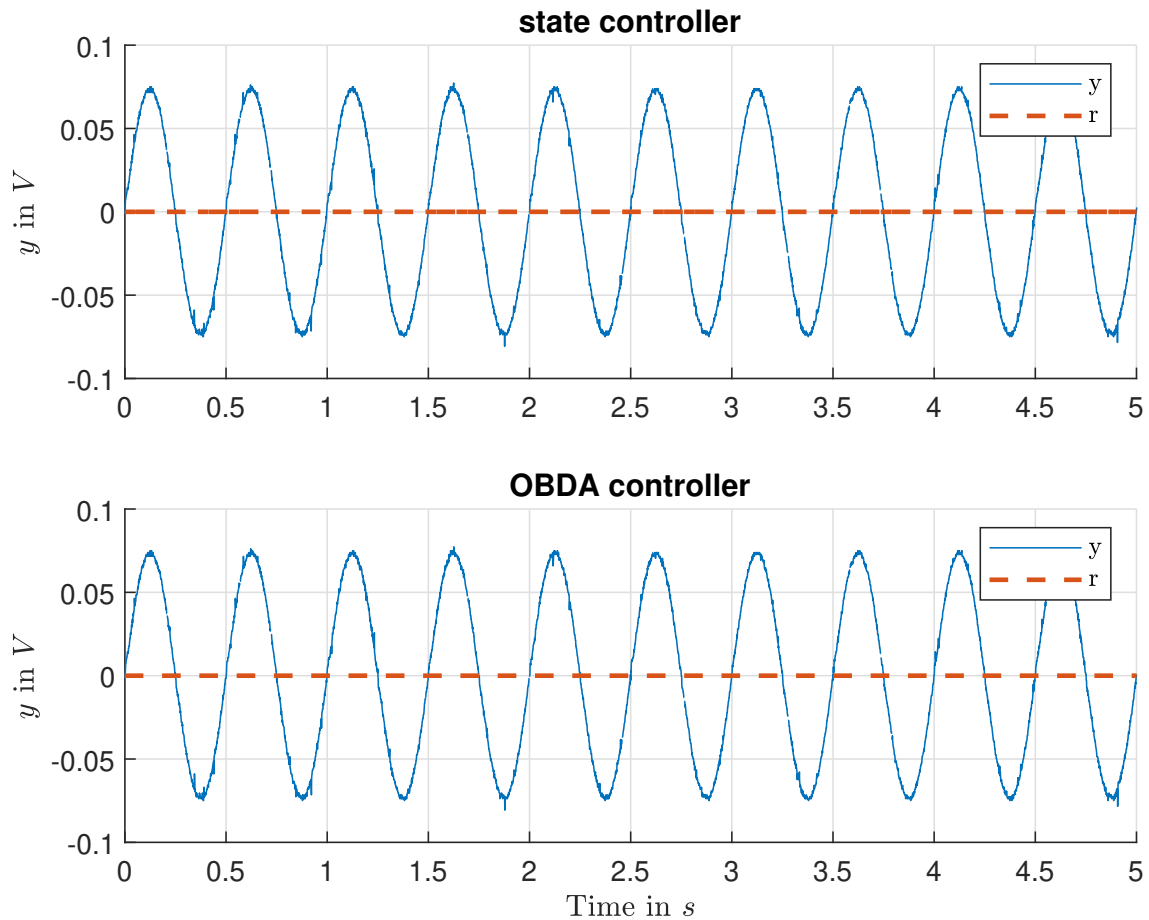


Figure 5.15: Results experiment 7b: Attenuation of a sinusoidal disturbance  $\Delta = 0.6 \sin(2\pi \cdot 2\text{Hz} \cdot t)$ .

### 5.2.3 Experiment 8

For the last experiment the system should also track a given reference input  $r = 0.2 \sin(2\pi \cdot 1\text{Hz} \cdot t)$  while having a sinusoidal disturbance  $\Delta = 0.6 \sin(2\pi \cdot 0.6\text{Hz} \cdot t)$ . Therefore, the controller parameters are altered according to Table 5.2. Figure 5.16 show the results. As can be seen all controllers are more or less able track the reference with the biggest deviations seen for the state controller.

The resulting control signals are shown in Figure 5.17a. With the higher gain, the measurements noise also has a bigger influence on the control signal of the state controller although there is much less chattering compared to the sliding mode approaches. The OBDA controller has by far the smoothest control signal.

Finally, Figure 5.17b shows the estimation of the disturbance. As both controller inherit the reference variable respectively the derivative of it in their control laws, the influence of the reference is cancelled and both yield good estimation results.

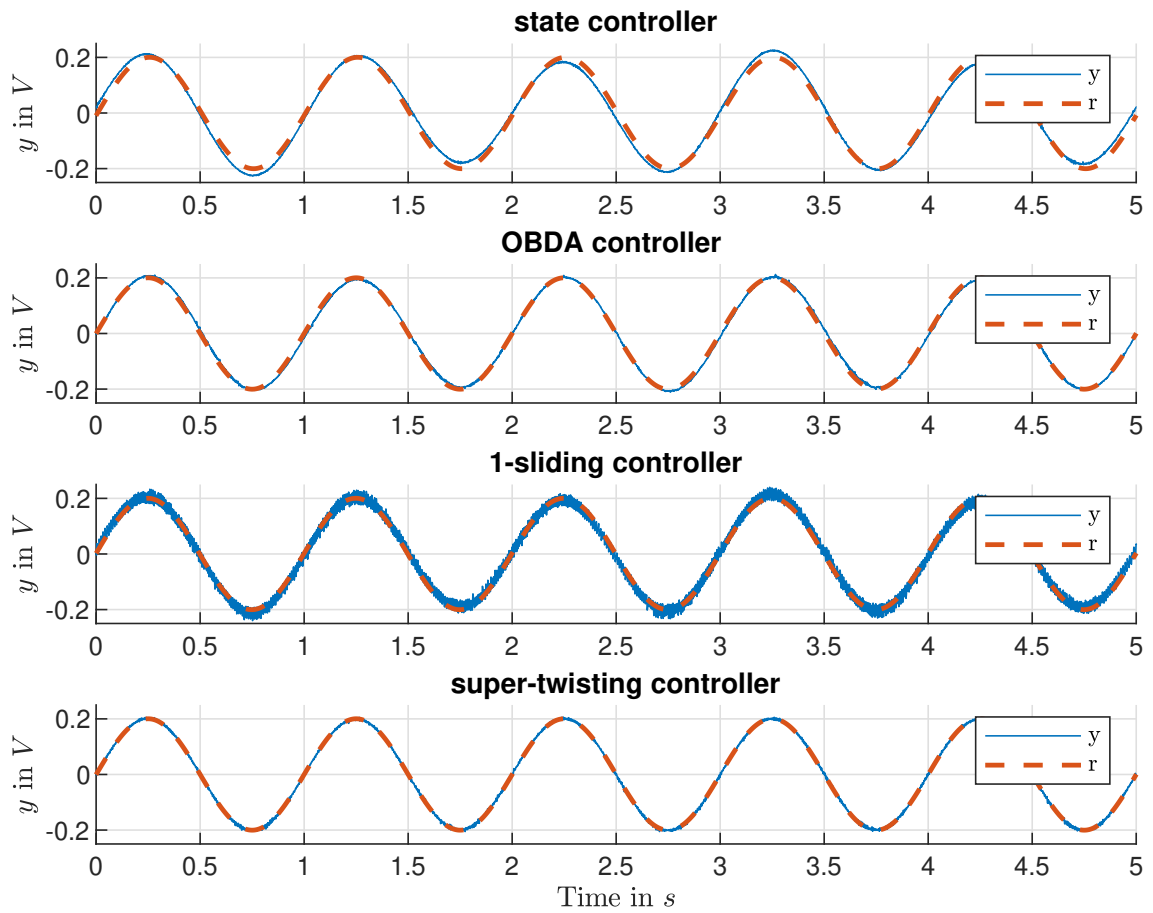
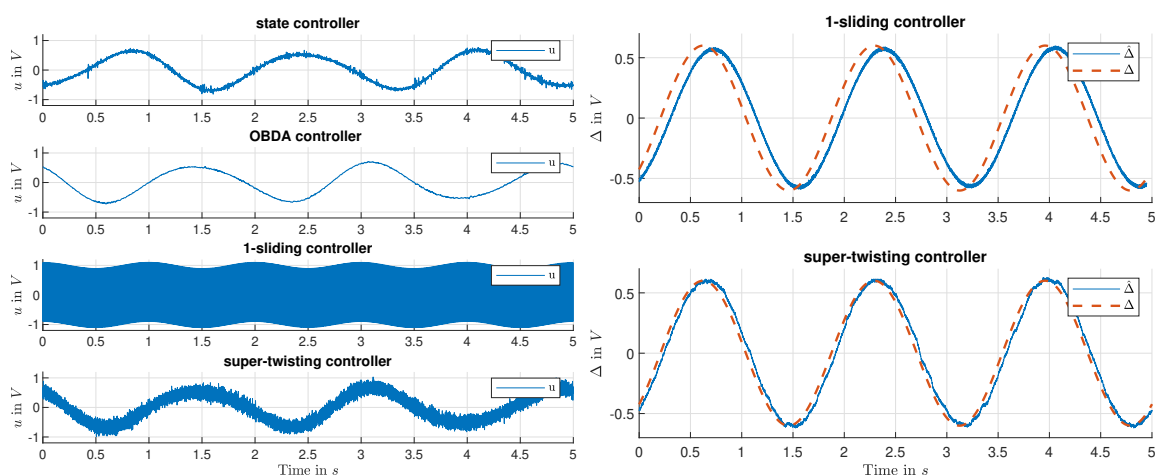


Figure 5.16: Results experiment 8: reference tracking with sinusoidal input disturbance.



(a) Control signal for reference tracking with sinusoidal input disturbance. (b) Estimation of a sinusoidal disturbance.

Figure 5.17: Results experiment 8, control signal and disturbance estimation.

## 6 Conclusion and Further Work

In this thesis, a laboratory set-up is designed, realised and tested to verify different control and observer algorithms using MATLAB Simulink. At first, based on the requirements, a modular hardware was developed for the laboratory set-up. The hardware was split into three parts, a measuring and actuator board, a connector board and test circuits. The three parts are connected using a defined plugging interface.

The measuring and actuator board is a LAUNCHXL-F28069M evaluation board from Texas Instruments. The board is equipped with a microcontroller ( $\mu\text{C}$ ) and ensures interfacing with MATLAB Simulink via a hardware support package. Furthermore, measurements are done using the analogue-to-digital converter of the  $\mu\text{C}$  and the actuation signals are output via the pulse-width-modulation module of the  $\mu\text{C}$ .

The connector board forwards the signals between the evaluation board and the test circuits. The actuator signals from the evaluation board are output digital-analogue converted and scaled to the test circuits. The differential measurements from the test circuits are anti-aliasing filtered, scaled and output ground referenced to the evaluation board.

As control respectively observer tasks a series resonance circuit and an integrator circuit were implemented as test circuits. The validation of the circuits showed that their dynamics approximately match the derived mathematical models.

The process of designing different controllers and observers for the two test circuits is presented step-by-step, with the designs then implemented in MATLAB Simulink. Finally, various experiments were carried out on the laboratory set-up. The experiments on the series resonance circuit handle reference tracking and state estimation whereas the integrator experiments solely deal with input disturbances. The experimental results also proof the applicability of the presented laboratory set-up.

Further work can be carried out in various different ways. At first however the data export from MATLAB Simulink should be improved as the current method is tedious. However, possible improvements are shown in the appendix A.1.3.

---

One possibility to extend the work is to design and implement additional controllers and observers for the given test circuits or to discretise the given models and execute the designs in the discrete time-domain. Another possibility is to design and implement new test circuits or connect the electric set-up with mechanical set-ups as test circuits, hence leading to various possible options. However, when considering new circuits the overall time constant of the designed circuits should be slower, as the current circuits with  $1kHz$  sample rate are already at the speed limit of the laboratory set-up in terms of data transfer between the evaluation board and MATLAB Simulink.

# Bibliography

- [1] R. C. Dorf and R. H. Bishop, *Modern control systems*. Pearson, 2011, vol. 12.
- [2] K. Ogata, *Modern control engineering*. Prentice, 2009, vol. 5.
- [3] N. S. Nise, *Control systems engineering*. Wiley, 2015, vol. 7.
- [4] K. J. Aström and R. M. Murray, *Feedback systems: an introduction for scientists and engineers*. Princeton university press, 2012.
- [5] O. Föllinger and U. Konigorski, *Regelungstechnik: Einführung in die Methoden und ihre Anwendung*. VDE Verlag, 2016, vol. 12.
- [6] J. Lunze, *Regelungstechnik 2: Mehrgrößensysteme, Digitale Regelung*. Springer, 2014, vol. 8.
- [7] R. E. Kalman *et al.*, ‘Contributions to the theory of optimal control’, *Bol. soc. mat. mexicana*, vol. 5, no. 2, pp. 102–119, 1960.
- [8] L. Desborough and R. Miller, ‘Increasing customer value of industrial control performance monitoring-honeywell’s experience’, in *AIChE symposium series*, New York; American Institute of Chemical Engineers; 1998, 2002, pp. 169–189.
- [9] G. F. Franklin, J. D. Powell, and A. Emami-Naeini, *Feedback control of dynamic systems*. Pearson, 2009, vol. 6.
- [10] M. Horn and N. Dourdoumas, *Regelungstechnik-Rechnerunterstützter Entwurf zeitkontinuierlicher und zeitdiskreter Regelkreise*. Pearson, 2004.
- [11] U. Kuhn, ‘Eine praxisnahe einstellregel für pid-regler: Die t-summen-regel’, *Automatisierungstechnische Praxis*, vol. 37, no. 5, pp. 10–16, 1995.
- [12] J. G. Ziegler and N. B. Nichols, ‘Optimum settings for automatic controllers’, *trans. ASME*, vol. 64, no. 11, 1942.
- [13] J. Lunze, *Regelungstechnik 1: - Systemtheoretische Grundlagen, Analyse und Entwurf einschleifiger Regelungen*. Springer, 2014, vol. 10.
- [14] C.-T. Chen, *Analog and digital control system design: transfer-function, state-space, and algebraic methods*. Saunders College Publishing, 1993.
- [15] J. Ackermann, ‘Der entwurf linearer regelungssysteme im zustandsraum’, *at-Automatisierungstechnik*, vol. 20, no. 1-12, pp. 297–300, 1972.



- [16] Y. Shtessel, C. Edwards, L. Fridman, and A. Levant, *Sliding mode control and observation*. Springer, 2014, vol. 10.
- [17] V. Utkin, J. Guldner, and J. Shi, *Sliding mode control in electro-mechanical systems*. CRC press, 2009, vol. 34.
- [18] A. F. Filippov, *Differential equations with discontinuous righthand sides: control systems*. Springer Science & Business Media, 2013, vol. 18.
- [19] V. Hagenmeyer and M. Zeitz, ‘Flachheitsbasierter entwurf von linearen und nichtlinearen vorsteuerungen (flatness-based design of linear and nonlinear feedforward controls)’, *at-Automatisierungstechnik/Methoden und Anwendungen der Steuerungs-, Regelungs-und Informationstechnik*, vol. 52, no. 1/2004, pp. 3–12, 2004.
- [20] M. Green and D. J. Limebeer, *Linear robust control*. Courier Corporation, 2012.
- [21] K. Zhou, J. C. Doyle, K. Glover, *et al.*, *Robust and optimal control*. Prentice hall New Jersey, 1996, vol. 40.
- [22] M. Reichhartinger, S. Spurgeon, M. Forstinger, and M. Wipfler, ‘A robust exact differentiator toolbox for matlab®/simulink®’, *IFAC-PapersOnLine*, vol. 50, no. 1, pp. 1711–1716, 2017.

# A Appendix

## A.1 Notes on MATLAB Simulink

As the laboratory set-up is run in MATLAB Simulink this sections shortly discusses the installation process for the hardware support package, how simulations are set-up and run and finally how the data is currently exported from the simulation and how this can be improved.

A good overview with examples of the integration of the Texas Instruments C2000  $\mu$ C into MATLAB Simulink is given in the MATLAB documentation<sup>1,2</sup>.

### A.1.1 Installations for Hardware Support

The installation of the hardware support package in MATLAB is straight forward. Via the Add-on section the *TI C2000 Piccolo Support from Embedded Coder*<sup>3</sup> can be searched and installed. Then just follows the installation steps, selecting the right processor family. During the installation process also install the third-party software *TI controlSUITE* and the *TI Code Composer Studio* (CCS). The controlSUITE is used from MATLAB as toolchain to build new applications with the CCS allowing to deploy the application on the  $\mu$ C. When setting up the CCS, select processor support for *C2000 real-time MCU's* as well as *TI XDS Debug Probe Support* for debug probes.

The process is also described in the MATLAB documentation<sup>4</sup>.

---

<sup>1</sup><https://www.mathworks.com/help/supportpkg/texasinstrumentsc2000/>

<sup>2</sup><https://www.mathworks.com/help/supportpkg/texasinstrumentsc2000/examples.html>

<sup>3</sup>*TI C2000 Support from Embedded Coder* also can be used as it allows to select the *TI Piccolo F2806x* processor family

<sup>4</sup><https://www.mathworks.com/help/supportpkg/texasinstrumentsc2000/ug/install-support-for-c2000-processors.html>

### A.1.2 Setting up and Running a Simulation

As from Section 2.2.1, simulations in MATLAB Simulink are run in *external mode* to communicate with the  $\mu$ C on the evaluation board.

The set-up of a simulation can be done according the MATLAB documentation section *Configure the Hardware and Model for External mode*<sup>5</sup>. Although following the steps of the documentation it is possible that the connection between the simulation and  $\mu$ C could not be established. Ensure that the setting of the debug probes is correct, with the *Load VCP* option for the *auxiliary* port checked<sup>6</sup>.

Building and deploying the target application on the  $\mu$ C can take up several minutes. When playing around with different parameters e.g. controller gains this would require to stop the simulation and build and deploy again if the parameters are inherited from the workspace. Another way is to change the parameters manually. However, both ways are tedious. By using the command

```
set_param('insertModelNameHere','SimulationCommand','update'),
```

where *insertModelNameHere* needs to be replaced with the actual model name, inherited parameters from the workspace are updated during the simulation without the need to build again.

### A.1.3 Data Export

According to the MATLAB documentation section *Data Logging*<sup>5</sup>, the export of the data from the simulation can be done using the *External Mode Control Panel*. However, after it did not work out after numerous tries an inconvenient and ugly workaround was taken to export the data.

Therefore, the scope data was saved as figure, with the data then extracted from the figure using a custom function. As the figure only saves limited data points, sections need to be zoomed before saving as figure to get detailed data. Nevertheless, this approach is just a workaround and should definitely be improved in future.

## A.2 Pinout Evaluation Board

Figure A.1 shows a visualisation of the pinout from the evaluation board. A numbered pinout can be found in the user guide<sup>7</sup>.

---

<sup>5</sup><https://www.mathworks.com/help/supportpkg/texasinstrumentsc2000/examples/parameter-tuning-and-signal-logging-with-serial-external-mode.html>

<sup>6</sup>[http://processors.wiki.ti.com/index.php/Using\\_the\\_serial\\_adapter\\_of\\_XDS100](http://processors.wiki.ti.com/index.php/Using_the_serial_adapter_of_XDS100)

<sup>7</sup><http://www.ti.com/lit/ug/sprui11b/sprui11b.pdf>

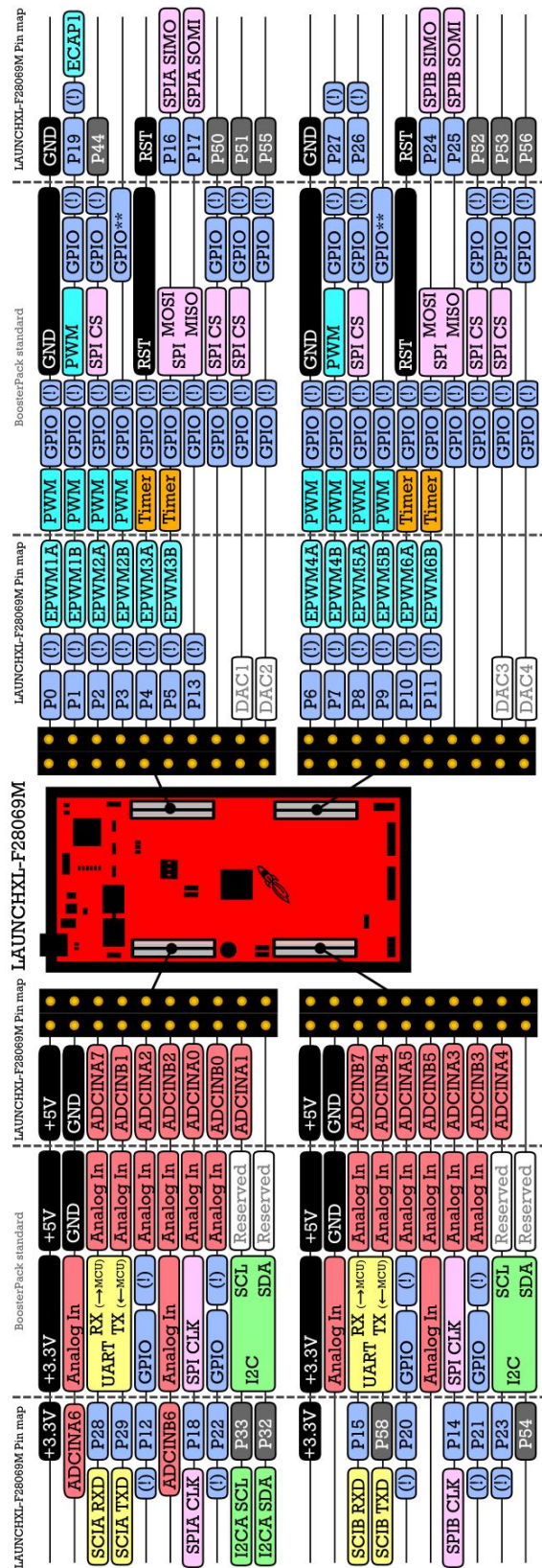


Figure A.1: LAUNCHXL-F28069M pinout. Snipped extracted from the Quick Guide <http://www.ti.com/lit/ml/sprui02/sprui02.pdf>.

## A.3 Connector Board

The circuit diagram of the implemented connector board is given in Figure A.2 with the corresponding component values listed in Table A.1.

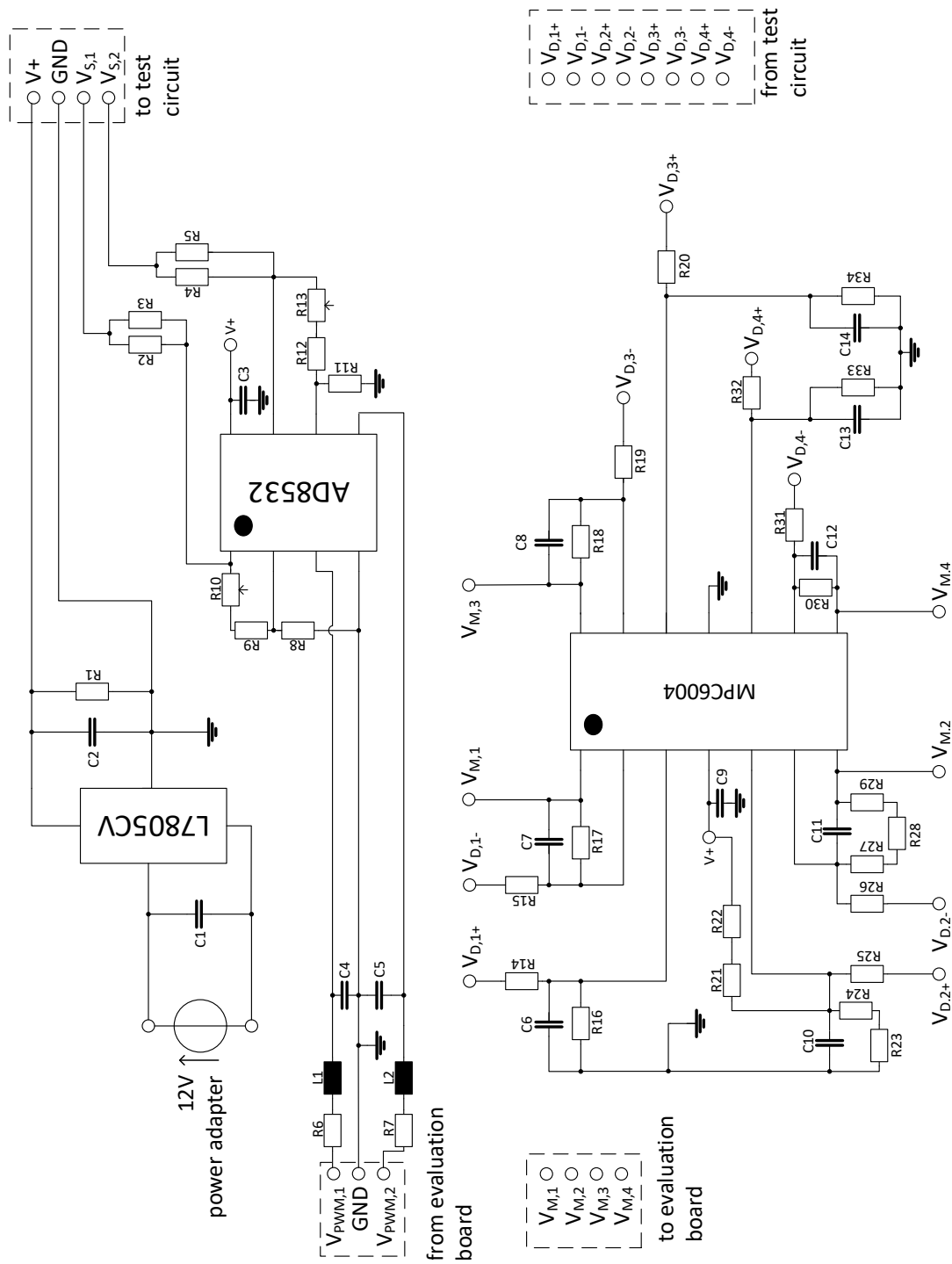


Figure A.2: Implemented circuit diagram of the connector board. The four dashed sections at the top and bottom indicate the plugging interface.

$L_1$	$L_2$	$C_1$	$C_2$	$C_3$	$C_4$	$C_5$	$C_6$	$C_7$	$C_8$
10mH	10mH	0.33 $\mu$ F	0.1 $\mu$ F	0.1 $\mu$ F	33nF	33nF	100pF	100pF	100pF
$C_9$	$C_{10}$	$C_{11}$	$C_{12}$	$C_{13}$	$C_{14}$	$R_1$	$R_2$	$R_3$	$R_4$
0.1 $\mu$ F	150pF	150pF	100pF	100pF	100pF	470 $\Omega$	50 $\Omega$	50 $\Omega$	50 $\Omega$
$R_5$	$R_6$	$R_7$	$R_8$	$R_9$	$R_{10}$	$R_{11}$	$R_{12}$	$R_{13}$	$R_{14}$
50 $\Omega$	1k $\Omega$	1k $\Omega$	100k $\Omega$	33k $\Omega$	25k $\Omega$ poti	100k $\Omega$	33k $\Omega$	25k $\Omega$ poti	1.5M $\Omega$
$R_{15}$	$R_{16}$	$R_{17}$	$R_{18}$	$R_{19}$	$R_{20}$	$R_{21}$	$R_{22}$	$R_{23}$	$R_{24}$
1.5M $\Omega$	1M $\Omega$	1M $\Omega$	1M $\Omega$	1.5M $\Omega$	1.5M $\Omega$	1M $\Omega$	250k $\Omega$	470k $\Omega$	150k $\Omega$
$R_{25}$	$R_{26}$	$R_{27}$	$R_{28}$	$R_{29}$	$R_{30}$	$R_{31}$	$R_{32}$	$R_{33}$	$R_{34}$
100k $\Omega$	100k $\Omega$	10k $\Omega$	200k $\Omega$	200k $\Omega$	1M $\Omega$	1.5M $\Omega$	1.5M $\Omega$	1M $\Omega$	1.5M $\Omega$

Table A.1: Component values connector board.

## A.4 Series Resonance Test Circuit

### A.4.1 Circuit Diagram

Figure A.3 shows the circuit diagram of the implemented series resonance test circuit. The corresponding component values are listed in Table A.2.

$L_1$	$C_1$	$C_2$	$C_3$	$C_4$	$R_1$	$R_2$	$R_3$	$R_4$	$R_5$	$R_6$
0.4H	10 $\mu$ F	22 $\mu$ F	47 $\mu$ F	0.1 $\mu$ F	5 $\Omega$	10k $\Omega$	100k $\Omega$	10k $\Omega$	200k $\Omega$	200k $\Omega$

Table A.2: Component values series resonance test circuit.

### A.4.2 Adjustment Instruction

For adjusting the series resonance test circuit run the circuit in the simulation as open-loop. By setting the reference signal to zero ( $r = 0$ ), both state variables should also yield zero ( $x_1 = x_2 = 0$ ). Any difference can be corrected within the Simulink integration block. Figure A.4 shows inner SRCI-block with the two variables to tune highlighted in green.

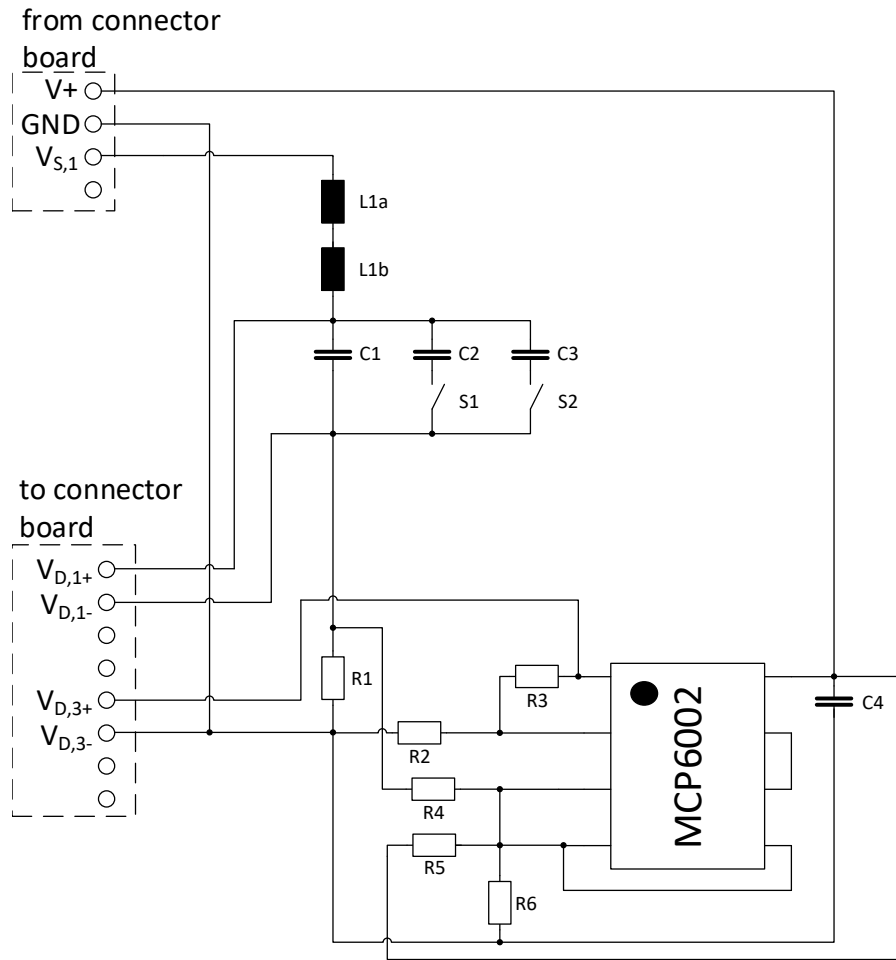


Figure A.3: Implemented circuit diagram of the series resonance test circuit. The two dashed sections at the left indicate the plugging interface. The two inductors at the top highlight the two single elements of the used component that are connected in series.

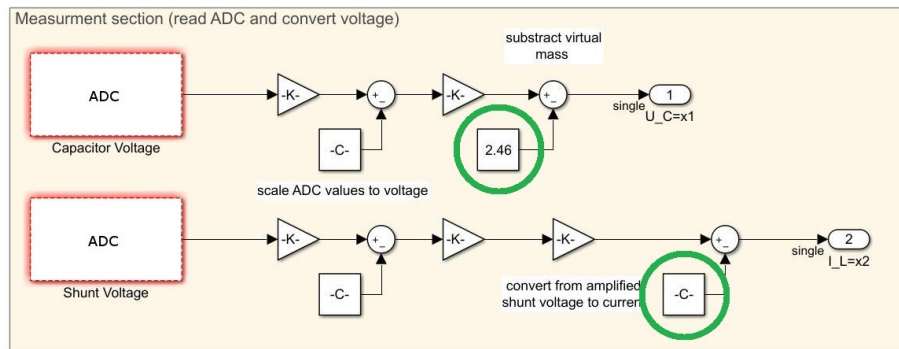


Figure A.4: Serial resonance circuit Simulink integration. The variables highlighted in green can be tuned during the adjustment.

## A.5 Integrator Test Circuit

### A.5.1 Circuit Diagram

The circuit diagram of the implemented integrator circuit is shown in Figure A.5 with the corresponding component values listed in Table A.3.

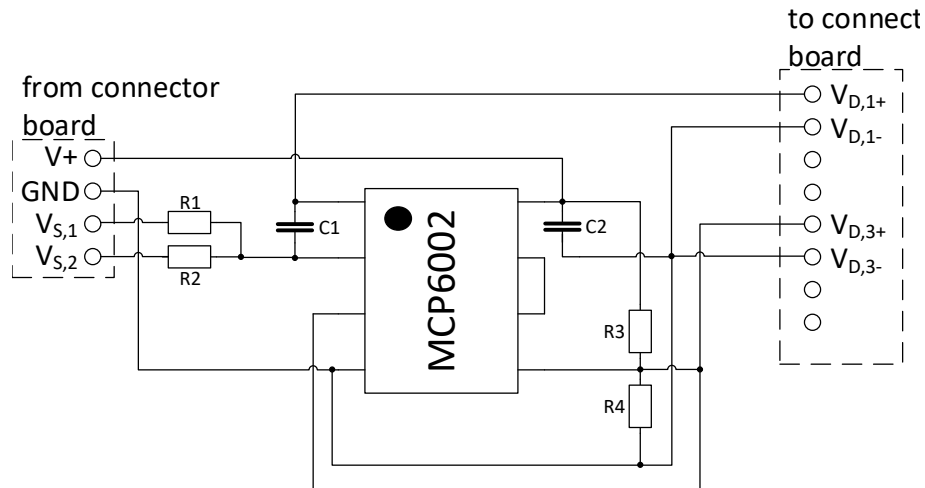


Figure A.5: Implemented circuit diagram of the integrator test circuit. The two dashed sections left and right indicate the plugging interface.

$R_1$	$R_2$	$R_3$	$R_4$	$C_1$	$C_2$
$150k\Omega$	$150k\Omega$	$150k\Omega$	$150k\Omega$	$1\mu F$	$0.1\mu F$

Table A.3: Component values integrator test circuit.

### A.5.2 Adjustment Instruction

For adjusting the integrator circuit run the circuit in the simulation as open-loop. By setting the reference signal and disturbance to zero ( $r = \Delta = 0$ ), the integrator should remain at the initial state. Figure A.6 shows inner ICI-block with the tunable variable highlighted in green. As the circuit integrates every little error it is hard to obtain ideal behaviour with no drift. Hence, it is acceptable if the circuit shows a slow drift after adjustment.



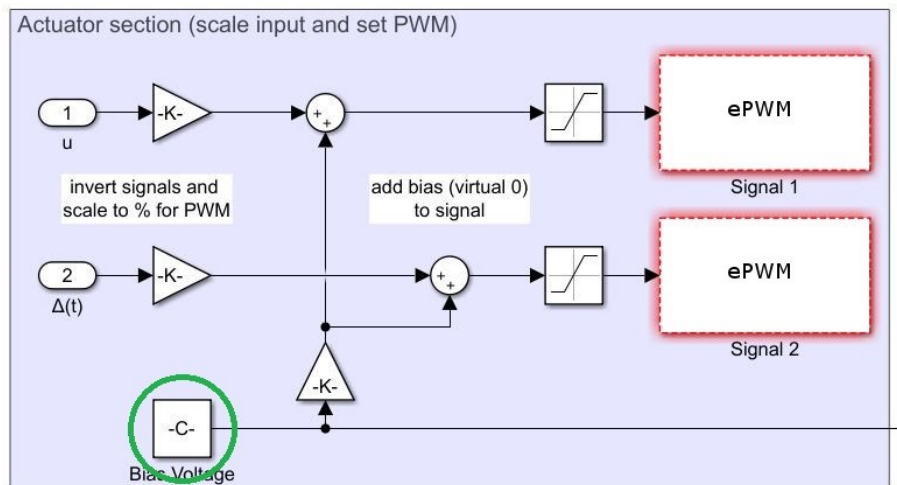


Figure A.6: Integrator circuit Simulink integration. The variable highlighted in green can be tuned during adjustment.